**Oak Ridge
National
Laboratory**

MAPPING FLOW LOCALIZATION PROCESSES IN DEFORMATION OF IRRADIATED REACTOR STRUCTURAL ALLOYS – FINAL REPORT

NUCLEAR ENERGY RESEARCH INITIATIVE PROGRAM No. MSF99-0072
PERIOD: AUGUST 1999 THROUGH SEPTEMBER 2002.

K. Farrell, T. S. Byun, and N. Hashimoto

UT-BATTELLE

Management Contractor for DOE's
Oak Ridge National Laboratory

MAPPING FLOW LOCALIZATION PROCESSES IN DEFORMATION OF IRRADIATED REACTOR STRUCTURAL ALLOYS – FINAL REPORT

K. Farrell, T. S. Byun, and N. Hashimoto

Date Published: September 2003

MAPPING FLOW LOCALIZATION PROCESSES IN DEFORMATION OF IRRADIATED REACTOR STRUCTURAL ALLOYS – FINAL REPORT

Contents

MAPPING FLOW LOCALIZATION PROCESSES IN DEFORMATION OF IRRADIATED REACTOR STRUCTURAL ALLOYS – FINAL REPORT

List of Figures

MAPPING FLOW LOCALIZATION PROCESSES IN DEFORMATION OF IRRADIATED REACTOR STRUCTURAL ALLOYS – FINAL REPORT

List of Tables

MAPPING FLOW LOCALIZATION PROCESSES IN DEFORMATION OF IRRADIATED REACTOR STRUCTURAL ALLOYS – FINAL REPORT

K. Farrell, T. S. Byun, and N. Hashimoto

Executive Summary

Metals that can sustain plastic deformation homogeneously throughout their bulk tend to be tough and malleable. Often, however, if a metal has been hardened it will no longer deform uniformly. Instead, the deformation occurs in narrow bands on a microscopic scale wherein stresses and strains become concentrated in localized zones. This strain localization degrades the mechanical properties of the metal by causing premature plastic instability failure or by inducing the formation of cracks. Irradiation with neutrons hardens a metal and makes it more prone to deformation by strain localization. Although this has been known since the earliest days of radiation damage studies, a full measure of the connection between neutron irradiation hardening and strain localization is wanting, particularly in commercial alloys used in the construction of nuclear reactors. Therefore, the goal of this project is to systematically map the extent of involvement of strain localization processes in plastic deformation of three reactor alloys that have been neutron irradiated. The deformation processes are to be identified and related to changes in the tensile properties of the alloys as functions of neutron fluence (dose) and degree of plastic strain. The intent is to define the role of strain localization in radiation embrittlement phenomena. The three test materials are a tempered bainitic A533B steel, representing reactor pressure vessel steel, an annealed 316 stainless steel and annealed Zircaloy-4 representing reactor internal components. These three alloys cover the range of crystal structures usually encountered in structural alloys, i.e. body-centered cubic (bcc), face-centered cubic (fcc), and close-packed hexagonal (cph), respectively.

The experiments were conducted in three Phases, corresponding to the three years duration of the project. Phases 1 and 2 addressed irradiations and tensile tests made at near-ambient temperatures, and covered a wide range of neutron fluences. Phase 3 was aimed at a higher irradiation and test temperature of about 288$^{\text{o}}$C, pertinent to the operating temperature of commercial reactor pressure vessel steels. Phase 3 explored a narrower fluence range than Phases 1 and 2, and it included an investigation of the strain rate dependence of deformation.

For Phases 1 and 2, tensile specimens of the three alloys were irradiated in the Hydraulic Tube facility of the High Flux Isotope Reactor (HFIR) at Oak Ridge National Laboratory to fast neutron fluences of 6 x 10^{20}, 6 x 10^{21}, 6 x 10^{22}, 6 x 10^{23}, and 5.3 x 10^{24} n.m^{-2}, E>1MeV, corresponding to doses of 0.0001, 0.001, 0.01, 0.1, and 0.8-0.9 displacements per atom (dpa). The irradiation temperature was 65-100$^{\text{o}}$C. Post-irradiation tensile properties were measured at room temperature at a strain rate of 10^{-3} s^{-1}. All three materials underwent progressive irradiation hardening and loss of ductility with increasing dose. Flow stresses were increased, yield point

drops were developed, work hardening rates were reduced, elongations were severely reduced, and early onset of failure occurred by plastic instability. The modes of plastic deformation involved in the various tensile behaviors were determined by curtailing tensile tests at prescribed levels of strain and then sectioning the specimens for examination by transmission electron microscopy. Four modes of deformation were identified, namely three-dimensional dislocation cell formation, planar dislocation activity, dislocation channel deformation (DCD) in which radiation damage structure has been swept away, and fine-scale twinning. These modes varied with material, dose, and strain level.

In the bcc A533B steel, deformation in the unirradiated specimens was homogeneous and occurred by interaction and tangling of dislocations to form dislocation cells. In those specimens of A533B steel irradiated to the two lowest doses, no radiation damage structure (RDS) was detected and there was only minor radiation hardening; the deformation behavior was similar to the unirradiated material. At the middle dose of 0.01 dpa, no RDS was seen but there was considerable radiation strengthening and the work hardening rate was reduced almost to zero. For this dose, the arrangement of strain dislocations was more linear, consistent with the decreased work hardening rate, but there was still some dislocation cell structure. At the highest dose, black spot radiation damage with a mean defect size of 1.3 nm and concentration of about $6.5 \times 10^{22} \text{m}^{-3}$ was evident. In the two highest dose specimens prompt plastic instability failures occurred at the yield stress. DCD with channels were about 40 nm wide was observed in the high dose specimens.

The fluence dependence of the tensile properties of the cph Zircaloy-4 alloy was found to be of similar form as for the A533B steel except that the degree of radiation hardening was higher at the lower doses and lower at the higher doses, compared to that for the A533B steel. No RDS was visible at the lowest dose of 0.0001 dpa. At 0.001, 0.01, 0.1, and 0.8 dpa there was fine black spot damage, reaching a size of 1.4 nm and a concentration of $6.1 \times 10^{22} \text{m}^{-3}$ at 0.8 dpa. For a dose of 0.001 dpa, and in the unirradiated Zircaloy, plastic deformation during tension testing occurred by coarsely dispersed planar slip primarily on the slip system $\{10\bar{1}0\}<11\bar{2}0>$, and to a lesser extent on $\{10\bar{1}1\}<11\bar{2}0>$. At 0.01 dpa, the deformation mode was still planar slip but with stronger participation of $\{10\bar{1}1\}<11\bar{2}0>$. At the two highest doses, where plastic instability failure was initiated at the yield stress, the deformation mode was DCD on the same slip systems. Channel widths were of order 50 nm.

The fcc austenitic 316 stainless steel, which has low stacking fault energy, behaved quite differently from the other two alloys. It displayed a similar degree of radiation hardening as the A533B steel yet it retained substantial work hardening and uniform elongation at all doses. In its unirradiated condition, and at the two lowest fluences, where no RDS was visible, it deformed by planar slip on its $\{111\}<110>$slip systems. As the level of strain was increased, the slip bands became more pronounced and tangled dislocations appeared in the matrix between the bands. Streaks from fine twins appeared in electron diffraction patterns. Dark field microscopy revealed that the twins were located within the deformation bands. At an irradiation dose of 0.01 dpa some black spot RDS was found, but the deformation mode was not altered. For the two highest doses, where black spot-type RDS was observed, dislocation channels were cleared through the RDS, primarily on the easy slip systems. In specimens irradiated to 0.1 dpa, most of the channels

were superimposed on the dislocation bands; there were also some very narrow channels containing neither dislocations nor twins. At the highest dose, where the black spot concentration was 4×10^{23} m^{-3} with a mean size of 1.8 nm, the dislocation bands and microtwins and channels were superimposed in the deformation bands and were very pronounced. Channel widths were about 20 nm. With increasing strain, the blocks of material between the heavy channel bands became subdivided into smaller blocks by development of new channel bands.

These observations are used to construct the first strain-neutron fluence-deformation mode maps for A533B pressure vessel steel, Zircaloy-4, and 316 austenitic steel. Analysis of the data shows that correlations between deformation mode and tensile properties are more complex than expected. Although there is a clear connection between the presence of DCD and the occurrence of yield point drops, reduced work hardening and severe ductility loss at high irradiation doses, the interactions are more subtle at lower doses and the changes in the tensile curve are more difficult to interpret. Most notably, irradiation encourages planar deformation which is seen as a precursor to channeling and which contributes to changes in the tensile curve. The pattern of change in deformation mode with increasing irradiation dose seems to be: Normal unirradiated mode —> planar banding —> DCD.

The deformation behavior of austenitic stainless steel was different from the other two alloys. Even in its unirradiated condition it deformed in a planar manner yet had high work hardening rate. After irradiation, when channels formed they were not devoid of dislocations as in the other two alloys. They contained extended dislocations and microtwins. Significant work hardening was retained. Of the three alloys investigated here, the stainless steel had the narrowest channels at a given dose and it was the most resistant to necking. It is suggested that the presence of microtwins in the channels moderates the behavior of glide dislocations in the channels and helps retain some work hardening in the channels, thereby reducing the concentrations of stress and strain in the channels and delaying necking.

Analysis of the fluence (φt) dependencies of the increases in tensile yield strengths (ΔYS) for all three alloys were made in terms of the relationship $\Delta YS = \alpha(\varphi t)^n$. Values of the radiation hardening exponent, n, were in the range 0.4 to 0.5 for fluences up to about 3×10^{22} n.m^{-2} (~0.05 dpa), and 0.08-0.15 for higher doses. The reductions in n, which could be read as indications of saturation of radiation damage structure due to cascade overlap, were found to be concurrent with acceleration of gross strain localization. It is postulated that intervention by DCD may be a significant factor in the reduced hardening exponent. Attempts to verify damage saturation in terms of the measured densities of defect clusters were inconclusive.

For Phase 3, new irradiations were made in the HFIR hydraulic tube facility using custom-modified capsules designed to attain a goal irradiation temperature of 288°C, which is the operating temperature for the pressure vessels in light water power reactors. The specimens were irradiated in March 2002 during the first fuel cycle following a prolonged shutdown of the reactor for scheduled major maintenance and upgrade. When the specimens were tested only minor radiation damage microstructure and radiation hardening were detected. Tests conducted at high strain rates at 288°C, and further tests made at room temperature to increase the sensitivity of detection of irradiation-induced changes in yield strength, confirmed that the level of retained damage was small. It was concluded that the reduced levels of radiation damage were

due to overheating of the specimens in the uninstrumented capsules during irradiation. Release of this report was delayed to allow investigation of the level and cause(s) of the elevated irradiation temperature. One suspected cause, a reduced coolant flow, was exonerated when new instrumentation for measuring the flow rate was installed in the reactor in January 2003. The other cause was uncertainties and leeway in the thermal-hydraulic calculations used to design the gap-controlled heat transfer in the capsule. From refined thermal generation and transport calculations and analysis of literature data it was deduced that the irradiation temperature was 330-350°C, and that such temperature must represent the threshold for dynamic annealing of radiation damage in all three alloys at displacement doses up to 0.1 dpa. This quantification of dynamic annealing temperatures makes a valuable contribution to our knowledge of radiation effects.

Tests conducted at strain rates in the range 10^{-5} to 1.0 s^{-1} show that the tensile properties of the three alloys are only slightly affected by strain rate and are slightly heightened by irradiation. Of the three alloys, Zircaloy-4 is the most sensitive to strain rate and is more sensitive at 288°C than at room temperature.

Some suggestions are offered for future work in this field.

MAPPING FLOW LOCALIZATION PROCESSES IN DEFORMATION OF IRRADIATED REACTOR STRUCTURAL ALLOYS – FINAL REPORT

K. Farrell, T. S. Byun, and N. Hashimoto

1.0 Background and Objective

Under applied loads, a plastically deformable metal can undergo considerable strain and tolerate much permanent change in shape without breaking. Such deformation takes place by the generation and movement of dislocations on multiple slip planes within the metal. Interaction and tangling of dislocations on intersecting planes causes resistance to further dislocation movement and requires a higher stress to continue the deformation. Such strain hardening, or work hardening as it is commonly known, is necessary to continue and extend the deformation in a uniform manner. Metals that deform in this manner are strained homogeneously throughout their bulk and they tend to be tough and malleable. On the other hand, if the metal does not deform homogeneously but instead the strain is restricted to a localized region, its mechanical properties are impaired and it fails prematurely. These contrasting features of uniform and non-uniform plastic deformation can be seen in the graphical record of a tension test. Fig. 1 is a schematic representation of a tensile test curve illustrating the characteristics of both uniform strain and strain localization by necking and showing the salient features for reading the tensile properties. Hereafter the word 'strain' is used synonymously with 'elongation', in both cases meaning the fractional increase in length of the gauge section.

In the tensile curve, plastic deformation is seen as the retained elongation, either uniform elongation (up to the ultimate tensile stress, or UTS) or as total elongation. Work hardening is registered as the increase in stress needed to continue increasing the elongation and to maintain uniform deformation. This engineering stress reaches a maximum at the UTS, which is the point where in true stress units the work hardening rate falls below the true stress level. As a consequence, uniform strain ceases and deformation continues locally by the formation of a neck, leading to ductile failure there. Since this necking occurs in a narrow region, less applied load is required to maintain or raise the necking stress, hence necking continues under a falling applied bulk stress and the work hardening slope becomes negative. Actually, the slope is negative only in terms of engineering stress-strain units. In true stress-true strain units, where the reduced cross-section in the neck is taken into consideration, the work hardening in the neck has a positive value. Such necking failure is the best-known type of strain localization. It is a gross phenomenon and is the normal fate of a ductile metal that has been strained too much.
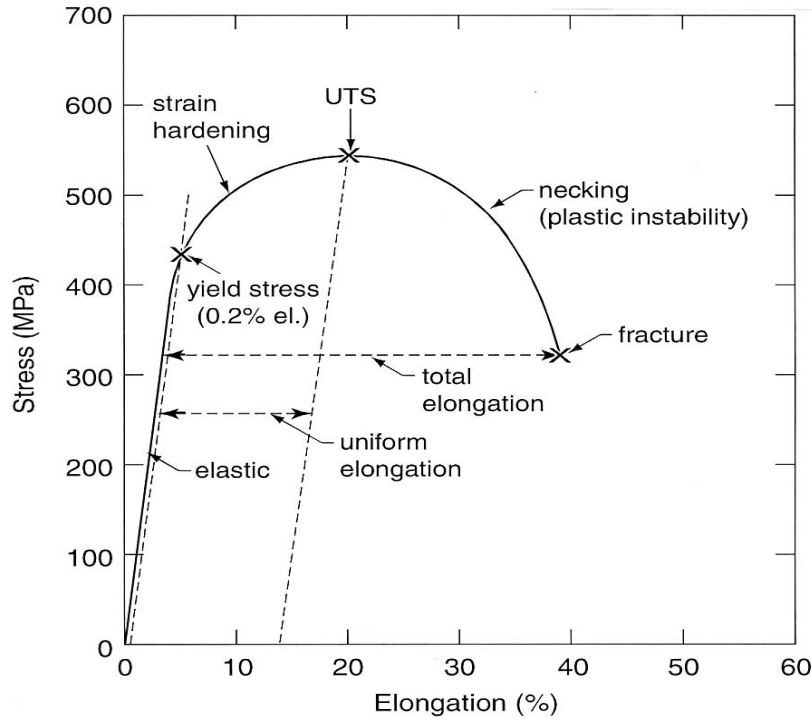
Fig. 1. Schematic tensile curve showing salient features employed in this work.

There are more insidious types of strain localization that occur in prehardened metals on a microscopic scale without the aid of built-in flaws and which can severely degrade the mechanical properties of the metal by causing premature plastic instability failure or by inducing the formation of cracks. One of these microscopic strain localization processes is dislocation channel deformation [1-3], hereafter referred to as DCD. DCD is a process of heterogeneous plastic deformation that entails only a few dislocation sources operating on widely separated slip planes. Dislocations released from the sources glide along the slip planes, cutting through and destroying or assimilating any barriers in their paths. This clearing action creates an easy passageway, or narrow channel a fraction of a micron wide, in which travel of subsequent dislocations from the source is easy, and therefore the strain remains confined to the channels. The large blocks of material between the channels undergo little or no deformation. The levels of strain in the channels can be very high, several hundred percent, whereas the bulk strain may be only a few percent [4, 5]. Consequently, the strains and stresses at the head of a channel can greatly exceed the applied bulk values and they have the potential for creating new channels or perhaps cracks.

Irradiation with neutrons hardens a metal and makes it more prone to DCD [1, 2]. Although this has been known since the earliest days of radiation damage studies [6], a full measure of the connection between neutron irradiation hardening, changes in mechanical properties, and strain localization is wanting, particularly in commercial alloys used in the construction of nuclear reactors. It seems obvious that strain localization must be intimately involved in radiation-

6

induced degradation of mechanical properties, but the correlation is not clear. One way to establish such correlation is with deformation mode maps.

Deformation mode maps originated from the work of M. F. Ashby [7] and his students who, more than twenty years ago, gathered information about the deformation behavior of a metal from diverse sources and condensed it into a single diagram depicting regions of specific deformation modes in terms of stress-temperature coordinates. Likewise, fracture mechanism maps were developed. With such maps one can instantly see for a given temperature and stress whether a material will be ductile or brittle and can determine what is controlling the deformation. The maps provide a guide to selection of the best range of processing conditions for working the material to a commercial product. Transparencies of maps of mechanical properties of the product and of its processing costs can be superimposed on the deformation map to choose the optimum production route. Ashby maps have now been extended to other parameters and other fields [8] and have become a valuable tool for matching materials and properties to applications. A comprehensive map not only correlates materials properties with its deformation behavior, it offers the potential for tracking and predicting the material's service performance. Radiation embrittlement curtails service life and raises safety issues in reactor materials. But there are no published Ashby-type maps for irradiated reactor structural alloys to outline the regions of minimum embrittlement or to indicate avoidance strategies, at least not for the temperature range 0-300°C. In this temperature regime the nearest thing to an Ashby-type deformation map are the two deformation mode-fluence maps [9] for nickel and gold, shown in Fig. 2. These mode maps outline the boundaries between regimes of uniform deformation occurring by cell formation and regions where deformation occurs locally by DCD. The boundaries are dependent on the degrees of fluence and strain. At lower fluences, cell formation is dominant at all strains, and in nickel the size of the dislocation cells decreases from 2 μm to 0.5 μm with increasing strain and increasing fluence. DCD is observed at a fluence of 2 x 10^{21}n.m^{-2}, but only at low strains; at higher strains it switches to cell formation. At the higher fluences, DCD is more persistent and is the dominant mode at all strains at fluences above about 1 x 10^{22}n.m^{-2}.

The goal of the present project is to systematically map the extent of involvement of strain localization processes in plastic deformation of three reactor alloys that have been neutron irradiated. The three materials are a tempered bainitic steel, A533B, representing reactor pressure vessel steels; annealed 316 stainless steel representing other reactor internal components; and annealed Zircaloy-4 alloy, also used as fuel cladding and internals. The deformation processes are to be identified and related to changes in the tensile properties of the alloys as functions of neutron fluence (dose) and degree of plastic strain.
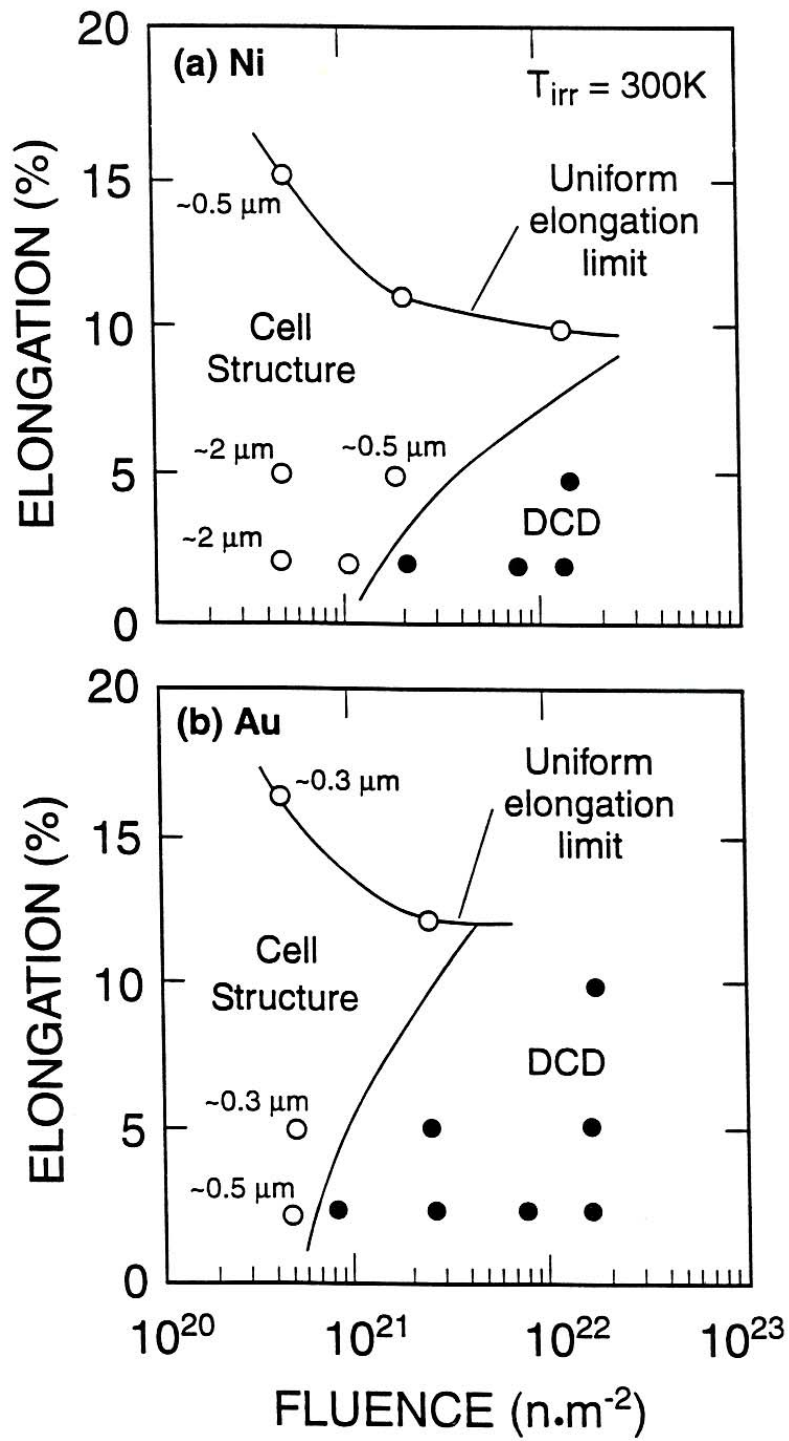
Fig. 2. Deformation mode-fluence maps for nickel and gold irradiated and tensile strained at 300K [9].

2.0 Route and Scope

The occurrence of strain localization can be recognized unambiguously by only one technique – visual examination of the strained test piece to determine whether the specimen is deforming in narrow bands instead of stretching uniformly along its gauge length. The examination can be done to a limited extent with the naked eye, to a better degree with the aid of optical instruments or scanning electron microscopy, and with more detail by transmission electron microscopy (TEM) examination. Indirect signs of strain localization can be found in tensile stress-strain curves. The most common of these changes are the appearance of a yield point drop, a reduction in the work hardening rate, and a reduction in elongation. Since similar tokens can originate from causes other than strain localization, the occurrence of one, or even two, of the signs is no assurance that strain localization is involved. But when all three signs occur together in the test curve there is increased confidence that they are indicating strain localization. One of the goals of this project is to bolster that confidence by correlating changes in the tensile curve with specific deformation modes. Optical examinations and changes in the shapes of tensile curves do not reveal details of the mode(s) of plastic strain localization; they can not tell whether the mechanism is dislocation channeling, mechanical twinning, or some other mode. TEM is the best technique for ascertaining the nature of the deformation mode. Therefore, the experimental route employed in this project was to irradiate tensile specimens of the alloys to a range of fast neutron fluences and obtain their tensile stress-strain curves and tensile properties. Companion specimens were subjected to various predetermined plastic strains in tension and cut into pieces for TEM examination to determine their deformation microstructures. The results were compiled into maps showing how the deformation modes change with neutron fluence and plastic strain. These changes in mode were compared to the corresponding changes measured in the tensile properties to establish and quantify the cause and effect relationship(s) between mechanical properties and deformation mode.

The project was laid out in three consecutive phases each of 12 months duration, as listed in Table 1. Phases 1 and 2 addressed irradiations and tensile tests made at near-ambient temperatures, and covered a wide range of neutron fluences. Originally, Phase 1 was intended to cover the low temperature irradiations and tests, and Phase 2 would be largely TEM work. However, the plan was disrupted by unexpected delays at the reactor that set the program back significantly. Therefore, a modification was made to the work plan that allowed tasks 1.2.3 through 1.3 to be carried into Phase 2. Phase 3 was aimed at a higher irradiation and test temperature of 290°C, pertinent to the operating temperature of commercial reactor pressure vessel steels. Phase 3 explored a narrower fluence range than Phases 1 and 2, and it included an investigation of the strain rate dependence of deformation.

Table 1. Project tasks, Phases 1-3.

Phase 1:

Task Description	Planned Completion Date	Actual Completion Date
1.1 Literature search	Sep-99	Nov-99
1.2 Perform experiments:		
1.2.1 Prepare test specimens	Nov-99	Jan-00
1.2.2 Conduct irradiations	Jan/Feb-00	Aug/Sep-00
1.2.3 Do tensile tests	Feb-00	Merged with Phase 2
1.2.4 Cut TEM pieces from tensiles	Mar-00	Merged with Phase 2
1.2.5 Do TEM survey	Jul-00	Merged with Phase 2
1.3 Compile initial maps	Jul-00	Merged with Phase 2

Phase 2:

1.2.3 Do tensile tests	Feb-00	Apr-01
1.2.4 Cut TEM pieces from tensiles	Mar-00	Apr-01
1.2.5 Do TEM survey	Jul-00	Sep-01
1.3 Compile initial maps	Jul-00	Sep-01
2.1 Conduct detailed TEM	Jul-01	Sep-01
2.2 Tabulate TEM data	Jul-01	Sep-01

Phase 3:

3.1 Do irradiations at ~300°C	Sep/Oct-01	Mar-02
3.2 Perform tensile tests at ~300°C	Oct/Nov-01	Aug-02
3.3 Conduct detailed TEM	Jul-02	Sep-02
3.4 Prepare final report	Aug/Sept-02	Sep-03

3.0 Experiment Conditions

The conditions employed in these experiments are summarized below. More details, and some of the reasons behind the choices of paths, are given in Appendix A. The experiments make use of miniature tensile and TEM specimens, custom-developed for this project and described in more detail in a paper [10] presented at the Fourth ASTM Symposium on Small Specimen Test Techniques, Reno, Nevada, January 23-25, 2001.

The three test materials are a tempered bainitic A533B steel, representing reactor pressure vessel steel, an annealed 316 stainless steel and annealed Zircaloy-4 (Zr-4) representing reactor internal components. Chemical compositions of the three alloys, and the heat treatments given to the tensile specimens, are described in Appendix A1. All machining and sanding operations were completed before the specimens were heat-treated. The dimensions of the tensile specimen are given in Fig. 3.
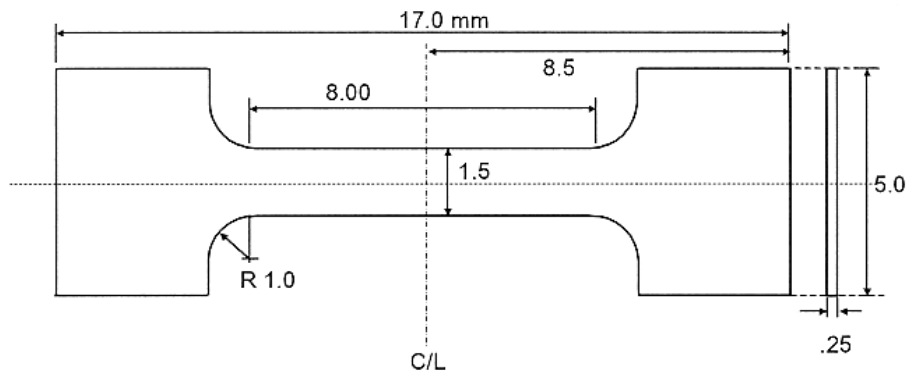
Fig. 3. The tensile specimen.

Irradiations were conducted in the Hydraulic Tube facility of the High Flux Isotope Reactor. This facility permits small aluminum capsules, called rabbits, to be shuttled in and out of the reactor core on demand in a stream of coolant water whilst the reactor is at power. Because of this required freedom of movement, the rabbits can not be wired to monitor or control their temperature. Gamma heat generated in the rabbit is carried away by the hydraulic flow. The goal irradiation temperature for the specimens for Phases 1 and 2 was <100°C and was obtained by irradiating the specimens in direct contact with the flowing coolant water using rabbits with many perforations through their walls. The inlet temperature of the water was 49°C and the outlet temperature was 69°C. The temperature of the specimens was estimated to be in the range 65-100°C. The irradiation exposures ranged from 5.9 x 10^{20} n.m^2 to 5.5 x 10^{24} n.m^{-2}, E>1MeV encompassing five discrete levels, listed in Tables 2 and A3. Correspondingly, nominal atomic displacement levels ranged from 0.0001 dpa to 0.89 dpa for the A533B steel to 0.00009 to 0.8 dpa for the stainless steel and Zircaloy-4. More details are available in Appendix A3.

For Phase 3, the goal irradiation temperature was 288°C, which is the operating temperature of the ferritic steel pressure vessels of commercial power reactors. To attain and maintain an elevated irradiation temperature, a non-perforated rabbit is used and the specimens are isolated from the rabbit wall by a gap filled with helium. Thermal/hydraulic calculations are used to carefully design the width of the gap so that part of the gamma heat developed in the specimens is used to keep them at the desired temperature, and the excess heat is transferred across the gap to the wall and thence to the coolant water flowing over the outer surface of the rabbit. More details of this arrangement are given in Section A3 of Appendix A. As seen in Tables 2 and A3, the irradiations for Phase 3 explored a narrower fluence range than Phases 1 and 2.

All tensile tests for Phases 1 and 2 were performed at room temperature in a screw-driven Instron machine at a crosshead speed of 0.008 mm.s^{-1}, corresponding to a specimen strain rate of 10^{-3} s^{-1}. Engineering strain was calculated from the recorded crosshead separation using a nominal gauge length of 8 mm. Engineering stress was calculated as the load divided by the initial cross section area before irradiation. The load cell was calibrated to NIST-approved

11

standards. Tensile tests for Phase 3 were made in air at 288°C in the same machine using a box furnace around the specimen cradle assembly. Two thermocouples for temperature measurement and control ensured that the temperature variation was no more than ±2°C. These 288°C tests included an investigation of the strain rate dependence of deformation over the range 10^{-3} s^{-1} to 10^{0} s^{-1}.

Table 2. Matrix of tensile tests for each alloy.

Fluence, n.m^{-2} (E>1MeV)	Nom. dpa	Tests to Failure	Truncated tests for TEM			
Phases 1 and 2[a]						
			0.5%,	5%,	At UTS	In neck
-0-	-0-	4	1	1	1	1
6E20	0.0001	2	1	1	1	1
6E21	0.001	2	1	1	1	1
6E22	0.01	2	1	1	1	1
6E23	0.1	2	1	1	1	1
5E24	0.8	2	1	1	1	1
Phase 3[b]						
6E23	0.1	2	-0-	1	1	-0-
5E24	0.8	2	-0-	1	1	-0-

[a] Irradiations at T=<100°C; tests at T=25°C; strain rate=10^{-3}.s^{-1}.
[b] Goal irradiation temperature was 288°C but overtemperature exposure occurred (see Section 5.0); tests were made at 288°C at strain rates of 10^{-3} s^{-1} to 10^{0} s^{-1}.

The matrix of tensile tests is displayed in Table 2. For each alloy, at least two specimens representing each dose level were tested to failure to obtain a full tensile curve and complete tensile properties. These data are tabulated in Appendix A4 and are described in the Results section. Tests on other specimens at the same doses were curtailed at prescribed strains and the gauge sections of the specimens were sectioned for TEM study. The TEM pieces cut from the gauge sections of the tensile specimens were rectangular with dimensions of only 1.5 x 1.5 x 0.25 mm, which is much smaller than a standard 3 mm diameter TEM disk. Preparation of electrothinned TEM foils from these small pieces in a Tenupol electropolishing apparatus required substantial development work and modification of Tenupol specimen holders, details of which are available in Ref. 10 and in Appendix A.

4.0 Results and Discussion, Phases 1 and 2

4.1 Bibliographies
Before describing the experimental results, attention is directed to the fact that the first task of Phase 1 was to compile bibliographies of published information on plastic deformation processes

in irradiated ferritic steels, austenitic stainless steels, and Zircaloy. They are presented herein as Appendices B, C, and D, respectively. Data from these Appendices and from a wider survey of literature on strain localization in other materials were used by the Principal Investigator to present an oral review of strain localization in irradiated metals at an International Workshop on Dislocation-Defect Interactions in Irradiated Materials, Toledo, Spain, April 3-5, 2000. The proceedings of the workshop were never published.

4.2 A533B Steel Results

The optical microstructure of the as-heat-treated A533B steel can be seen in Fig. A1.1 in Appendix A. TEM study of the specimens revealed microstructures consisting of packets of lath-like grains divided into equiaxed subgrains about 300-1000 nm size and containing many tangled dislocations, Fig. 4. Numerous carbide particles of sizes 50-500 nm were distributed randomly through the matrix. The resident tangled dislocations pose a problem for identification of deformation mechanisms after straining because the strain dislocations are indistinguishable from the preexisting dislocation tangles. Fig. 4 was actually taken after 6% strain, and the structure is essentially the same as for an unstrained specimen.

In the as-irradiated specimens, no radiation-induced defect structure (RDS) was discernable for doses of 0.0001, 0.001, 0.01, and 0.1 dpa. This apparent absence of RDS does not necessarily mean that none was present; it means that none was seen, either because the defects were too small for detection, <1 nm diameter, or the TEM foils were not of sufficiently good quality to allow the defects to be seen. For the 0.89 dpa dose, RDS was clearly visible as distinct black spot defects, Fig. 5. Note that in all the materials examined in this work, some of these black spots are small dislocation loops, not all of which are visible in a given beam direction. To account for most of the spots, they are measured in dark field weak beam conditions but no attempt is made to determine the invisible fractions. Measurements of the defects in the A533B steel at 0.89 dpa gave a concentration of 6.5×10^{22} m^{-3} and a mean size of 1.3 nm. Their size distribution is shown in Fig. 6.

The effects of neutron fluence on the tensile properties of the A533B ferritic pressure vessel steel are presented in Figs. 7 and 8. Fig. 7 contains example tensile test curves. The small wriggles on the curves are electronic noise signals and should be ignored. Also, the seeming increase in elastic modulus with dose is not real. It is a reflection of the 'softness' of the loading system couplings under the very small loads required for straining the miniature specimens; the system stiffens as the load is increased. The yield point drop and the associated region of elongation at constant stress, known as the Lüders region, for the unirradiated specimen are real and are characteristic of a pressure vessel steel. In Fig. 8, YS is the yield strength and UTS is the ultimate tensile strength. UE is the uniform plastic strain or elongation, and STN is the strain-to-necking, which is a measure of the uniform strain when the work hardening rate in engineering stress units is close to zero. TE is the total elongation.
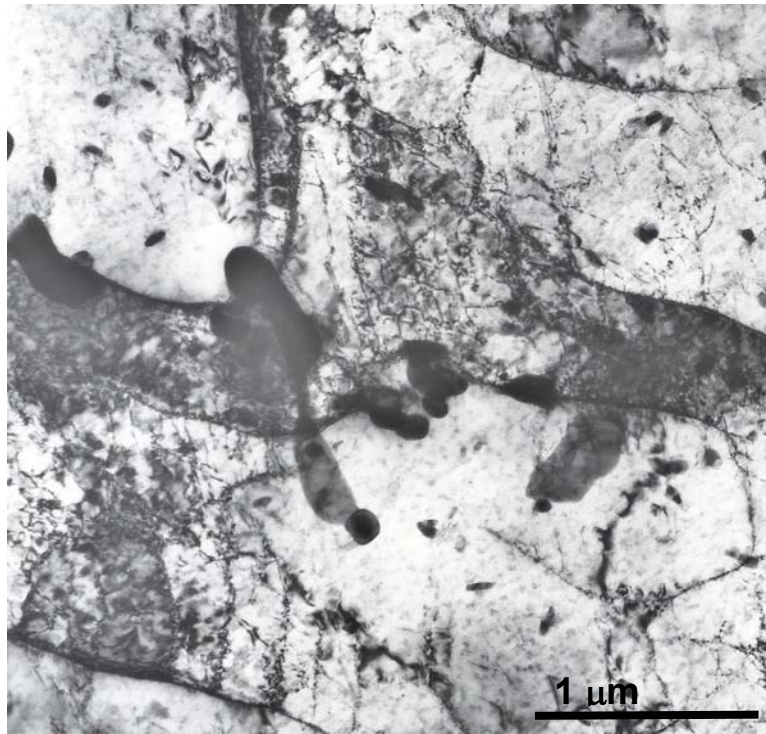
Fig. 4. Microstructure of unirradiated A533B steel at 6% strain.

$[\bar{1}10]$

$[110]$

B=[001], **g**=[110]
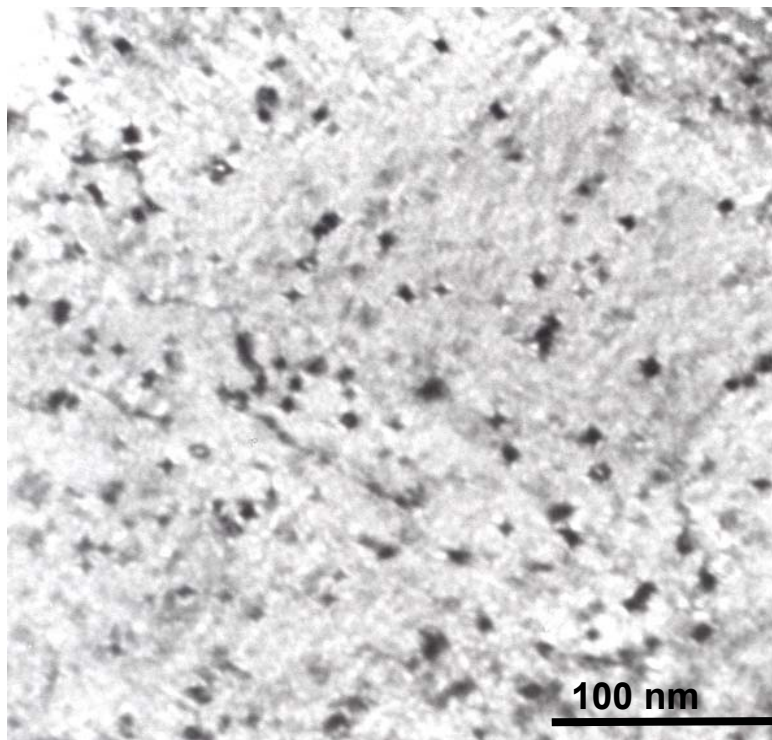
Fig. 5. Black spot irradiation damage structure in A533B steel irradiated to 0.89 dpa.
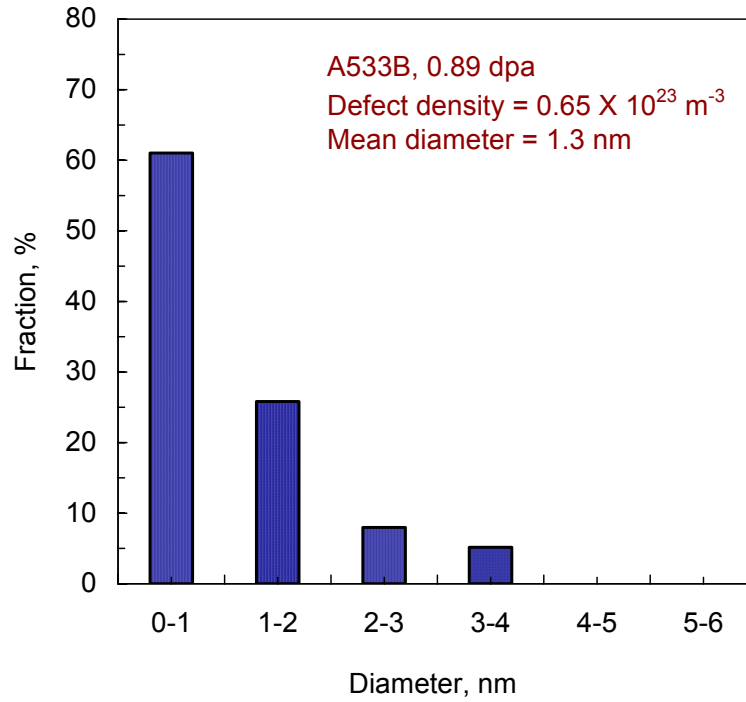
Fig. 6. Size distribution of black spot RDS in A533B steel after irradiation to 0.89 dpa.
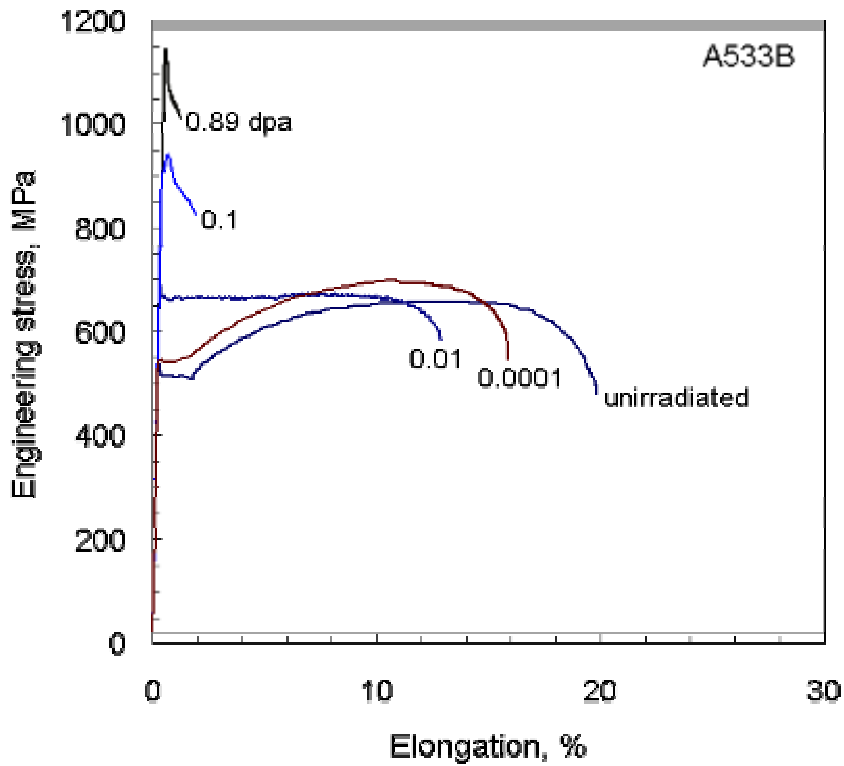
Fig. 7. Representative tensile test curves for A533B steel after different neutron exposures.

15
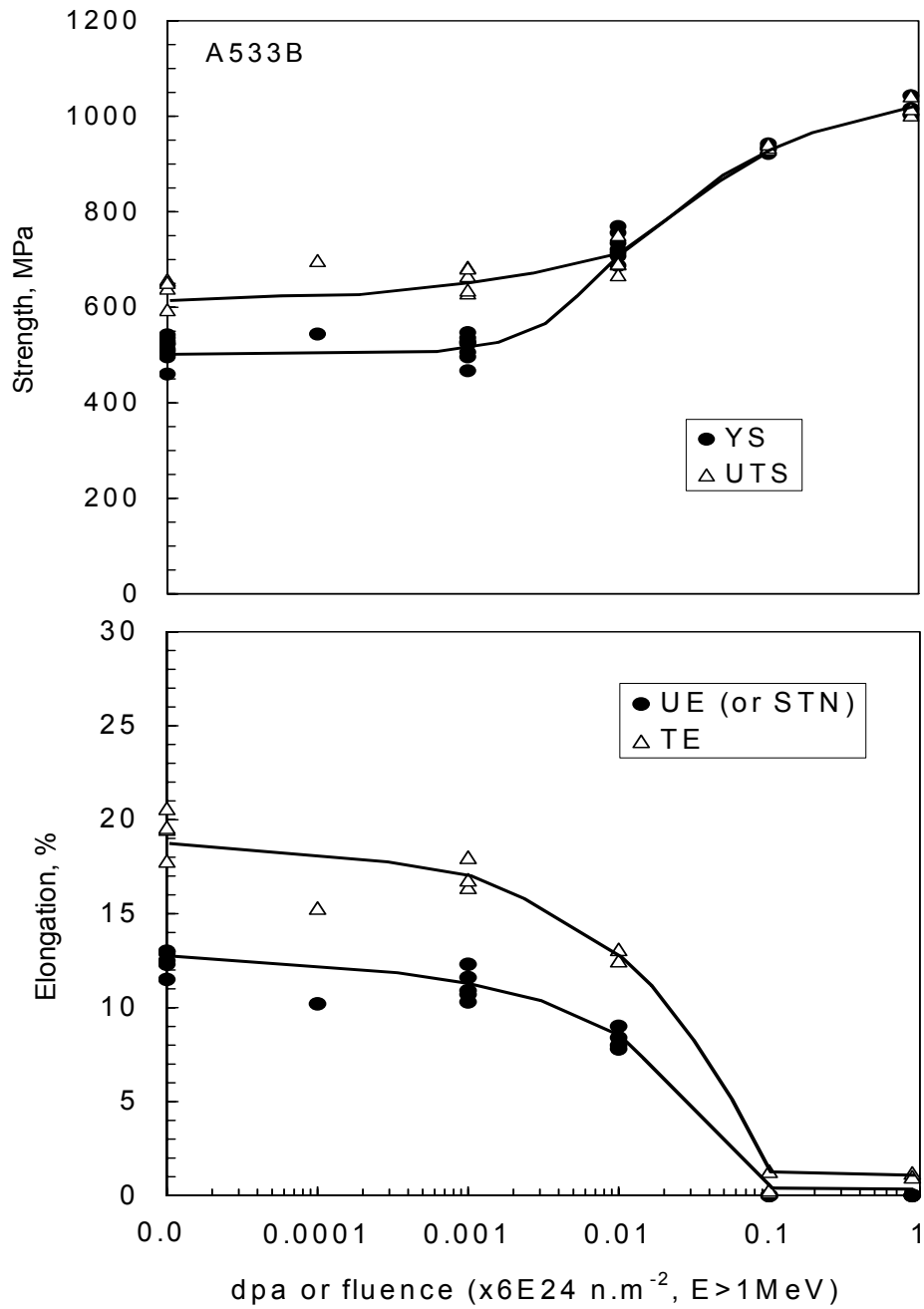
Fig. 8. Dose dependence of tensile properties of A533B steel. (Abbreviations are defined in text).

It can be seen from these figures that for the two lowest doses of 0.0001 and 0.001 dpa there are small increases in YS and UTS, and small reductions in elongation. The increases in YS and UTS are about equal, which means that irradiation to these low doses did not alter the work hardening behavior. At the middle dose of 0.01 dpa, the increase in YS and decrease in elongation are more pronounced and the work hardening region is almost flat, the UTS being barely larger than the YS. Moreover, the UTS is about the same value as the UTS values for the lower doses. For the two higher doses of 0.1 and 0.89 dpa, the UTS and YS are indistinguishable but are considerably higher than for the lower doses; prompt plastic instability occurs at yield, and elongations are severely curtailed. Concomitant with these pronounced increases in YS the work hardening behavior is radically impaired.

Work hardening, or strain hardening as it is alternatively known, is a characteristic of ductile metals in which the stress required to continue the process of plastic deformation is raised asymptotically with increasing strain. It is caused by dislocations interacting with each other and with barriers. Such intermingling of dislocations is essential to maintain bulk plasticity. Without it, plastic deformation becomes localized and shear failure ensues at curtailed elongation. So reduced work hardening is an indicator of strain localization. A rough measure of work hardening rate expressed in engineering stress and strain units can be obtained from the average slope of the tensile curve in the range of the first few percent elongation. More formally, a work hardening exponent, n, can be derived from the tensile flow curve assuming it follows a power law, often, $\sigma = K\varepsilon^n$, where σ and ε are true stress and true strain values. It can then be shown that n is numerically equal to, or is proportional to, the strain at which necking occurs. Table 3 is a list of approximate work hardening rates and n values measured on all three materials for all doses. Both metrics show the same trend with increasing dose. In the A533B steel, the work hardening rate is around 2500 MPa for the unirradiated material and for the two low dose irradiation levels, indicating that these low levels of irradiation have not altered the deformation behavior, and implying that strain localization is not involved. At the middle dose of 0.01 dpa, the work hardening rate is reduced markedly to 70 MPa, and at 0.1 and 0.89 dpa it is strongly negative. A decreased value indicates that the deformation mode has changed and there is less resistance to slip, implying intervention of strain localization. A negative value indicates that strain is occurring under a falling stress; it results from the occurrence of gross necking.

Table 3. Average work hardening rates (MPa, engineering units) in the plastic strain range 0 to 5% elongation. Values of work hardening exponent, n, are shown in square brackets.

Nom.dpa	A533B	Zr-4	316SS
0	2220 [.08]	760 [0.06]	1520 [0.25]
0.0001	2700 [.08]	980 [0.06]	1660 [0.25]
0.001	2380 [.09]	680 [0.05]	1770 [0.20]
0.01	70 [0.015]	-120 [0.011]	1550 [0.14]
0.1	-6470	-440	1160 [0.11]
0.8	-12300	-1120	760 [0.09]

In the present case, necking occurs prematurely in the form of prompt strain localization at the YS, leading to plastic instability failure. If analyzed in terms of true stress-true strain units, a negative engineering work hardening rate corresponds to a small, positive true engineering work hardening rate. The work hardening rate in Zr-4 is low because of its fewer slip systems; it falls markedly at a dose of 0.01 dpa, like in the A533B steel. The 316 steel is different. It shows no abrupt decline at 0.01 dpa, and only relatively small reductions at higher doses.

With regard to deformation microstructures observed in the deformed specimens, the mode of deformation appeared to be multiple slip and dislocation tangling in the unirradiated A533B specimens and in the two lower dose specimens, Figs. 9(a) and 9(b). For 0.01 dpa the deformation mode was still predominantly dislocation tangles. At doses of 0.1 and 0.89 dpa, where large increases in yield stresses accompanied by prompt plastic instability failures were found, it was difficult to characterize the deformation mode because the strain was so strongly localized that most of the TEM sections cut from the gauge length were barely strained whilst those TEM pieces taken from the highly necked fracture region were of unsuitable shape for electrothinning. Hence, although a few dislocation channels were observed they were insufficient for statistical analysis. Several channels are shown in Figs. 9(c) and 9(d). They are about 40nm wide. The channels pass undeflected through the laths but change direction at the bainite packet boundaries.

The deformation mode map derived for A533B steel from these observations is shown in Fig. 10.
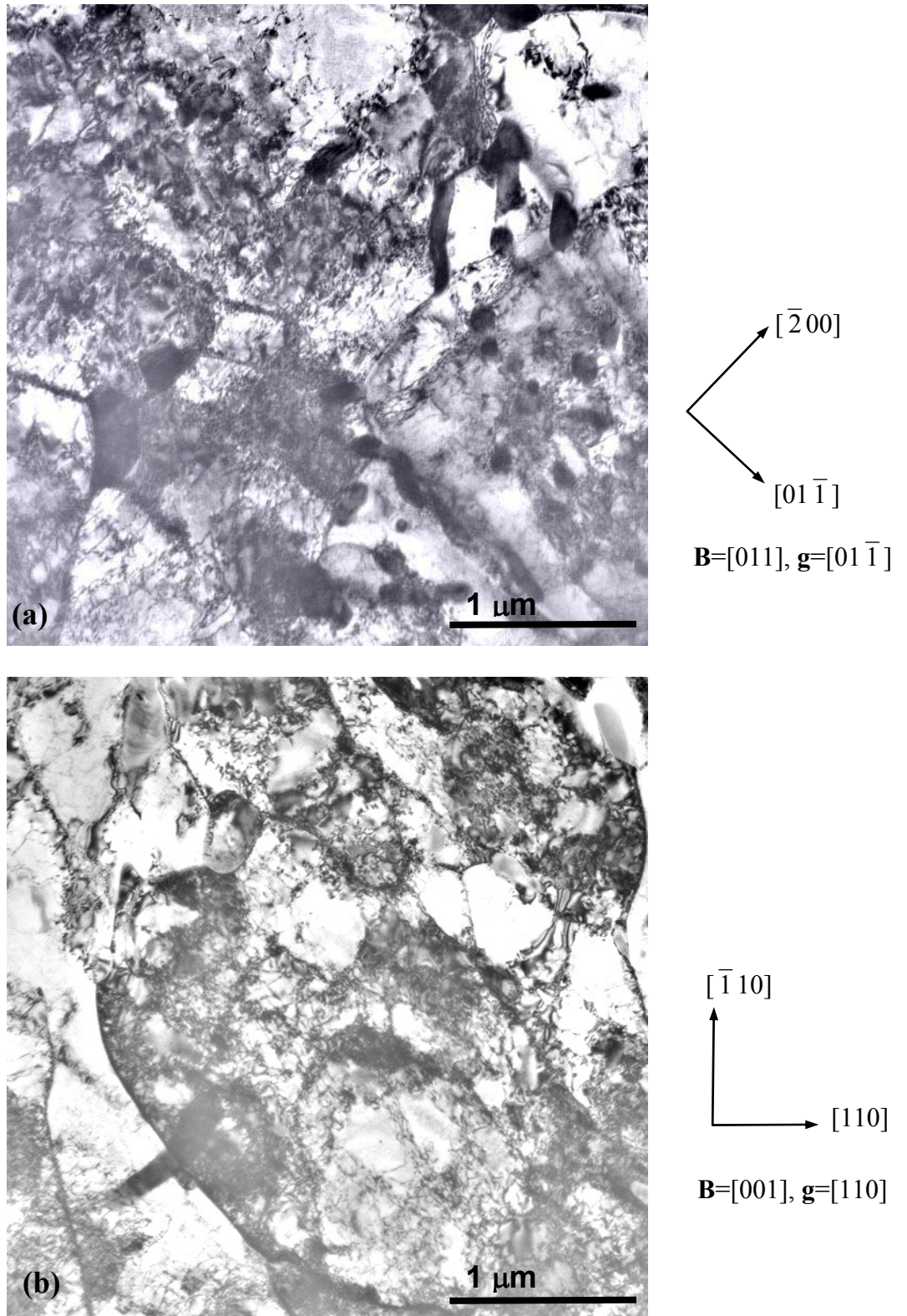
Fig. 9. Deformation structure of unirradiated A533B steel and low dose specimens: (a) at 0.001 dpa after 5% strain, (b) at 0.01 dpa after 10% strain.

Legend for (c):
$[\bar{1}10]$
$[110]$
B=[001], **g**=[110]

Legend for (d):
$[\bar{2}00]$
$[01\bar{1}]$
B=[011], **g**=[01$\bar{1}$]
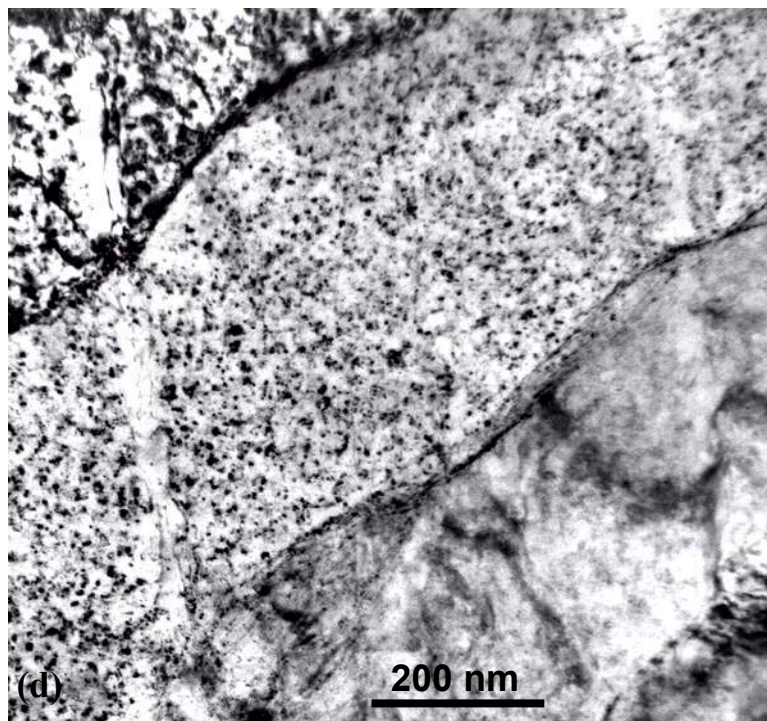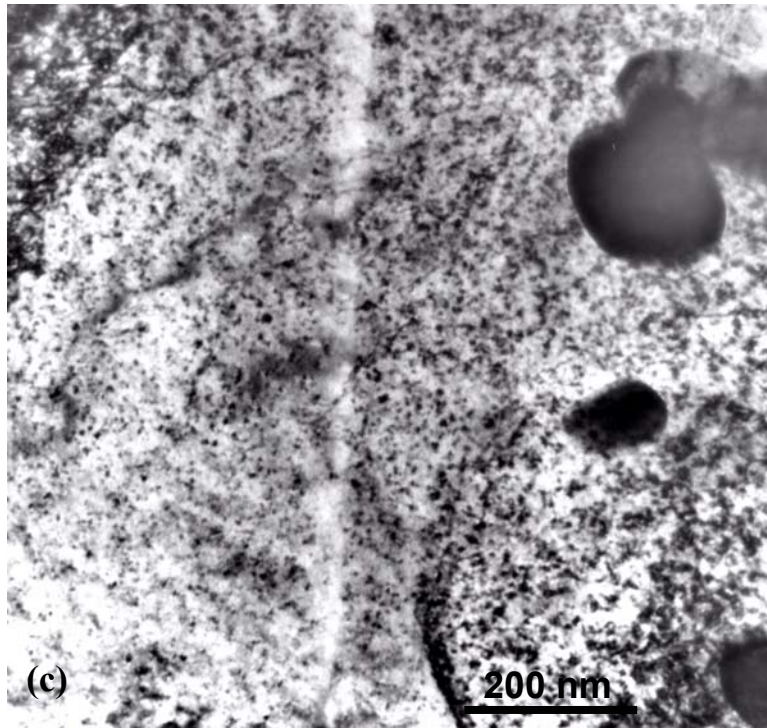
Fig. 9. (continued). Dislocation channels in A533B steel irradiated to 0.89 dpa and strained to 2%: (c) and (d).
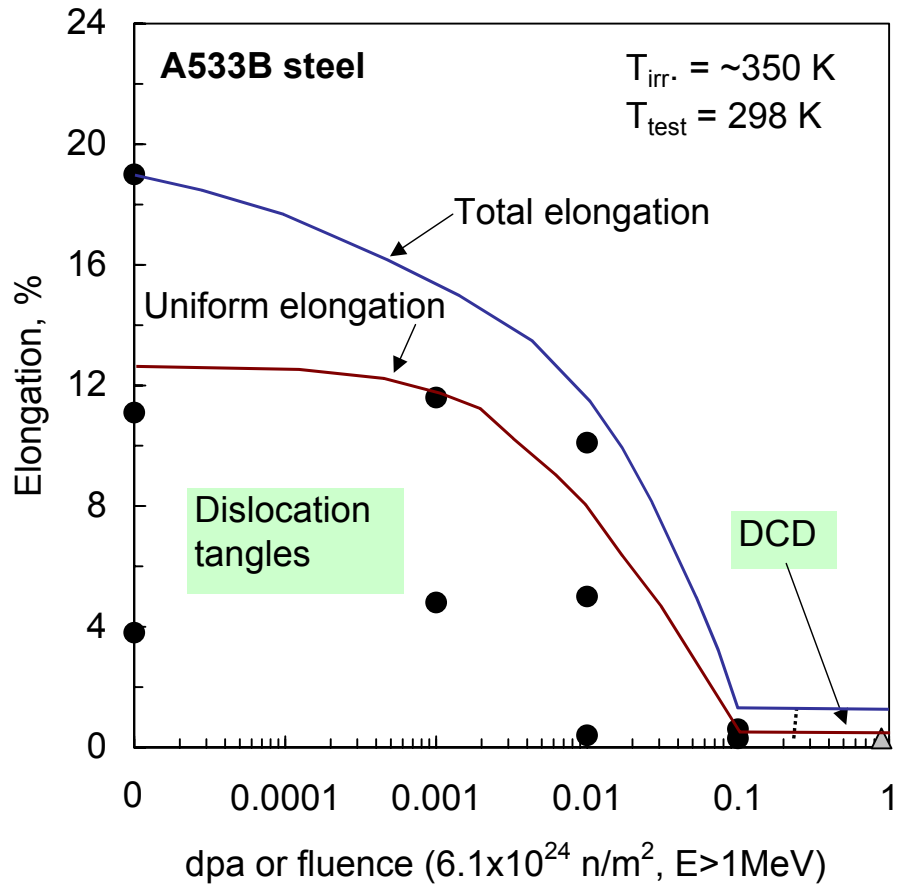
Fig. 10. Deformation mode map for A533B steel neutron-irradiated at 65-100°C and tested at room temperature.

4.3 Zircaloy-4 Results

The microstructure of unirradiated Zr-4 consisted of equiaxed grains containing a few grown-in dislocations. In the as-irradiated specimens no RDS was found at a nominal dose of 0.0001 dpa. At 0.001 dpa, fine black spots were just discernable at a concentration of about 1.1×10^{22} m^{-3} and mean size of 1.2 nm. At the highest dose, 0.8 dpa, black spot damage was quite evident at a concentration of 6.1×10^{22} m^{-3} and mean size 1.4 nm. A bar graph of the size distribution for 0.8 dpa is given in Fig. 11.
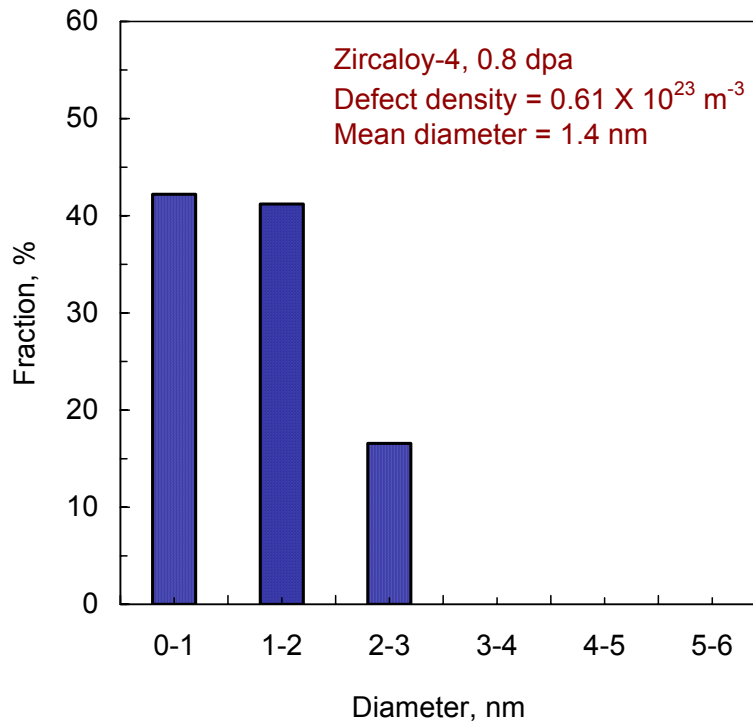
Fig. 11. Size distribution of black spot RDS in Zircaloy-4 irradiated to 0.8 dpa.

Fig. 12 displays typical tensile test curves for Zr-4. Characteristically, annealed unirradiated Zr-4 does not display a yield point drop, and none are found in the unirradiated specimens and in those irradiated to low doses of 0.0001 (not shown) and 0.001 dpa. These low doses raise the YS and UTS but do not significantly alter the work hardening rate. The work hardening rate, Table 3, for unirradiated Zr-4 is 760 MPa and is 680-980 MPa for the low dose irradiations. At a nominal dose of 0.01 dpa, the increase in YS is much larger than at the lower doses and a weak yield point drop is seen; the work hardening rate is negative but necking to failure is not immediate, it is extended over an elongation of almost 20%. Several small bumps in the curve suggest that multiple necks dispersed along the gauge length were involved. The curve for the nominal 0.1 dpa dose is very similar to that for 0.01dpa except for a higher YS and a much stronger yield point drop. Again, necking is drawn out over about 20% elongation and there are several bumps in the necking part of the curve. For the highest dose of 0.8 dpa, a yield point drop is prominent; necking is diffuse but is without bumps.
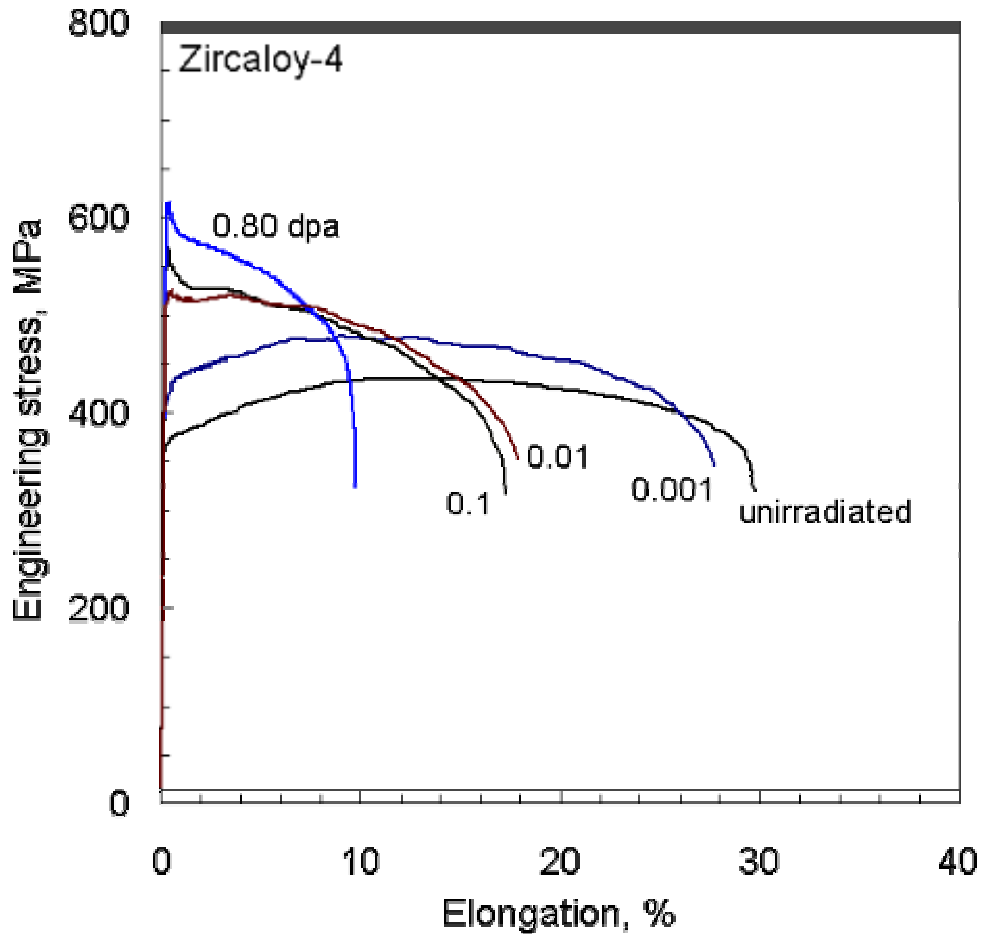
Fig. 12. Tensile test curves for Zircaloy-4.

The changes in tensile properties of Zr-4 with dose are plotted in Fig. 13.

After plastic deformation, the unirradiated specimens and the two lower dose specimens of Zr-4 contain widely-spaced bands of elongated dislocations lying mainly in the prismatic $\{10\bar{1}0\}<11\bar{2}0>$ slip system, with a small amount in the pyramidal $\{10\bar{1}1\}<11\bar{2}0>$ system, Fig. 14. No DCD is found. In the 0.01dpa specimens, the strain dislocations are still in widely separated bands but now the secondary, $\{10\bar{1}1\}<11\bar{2}0>$ system, is more strongly involved. The dislocations in the major slip bands are lying in channels, Fig. 15 (a), seen as white bands by slightly tilting the specimen to put the contained dislocations out of contrast, Fig. 15 (b). The channel edges are not sharp, and the channel contrast is not strong, suggesting that there are remnants of RDS in them. Channel widths varied from barely perceptible lines to about 100 nm. The spacing between the wider channels was roughly 500 nm, and the narrower channels were contained between them. Assuming the larger channels to be created first, their presence obviously did not inhibit the formation of new channels.
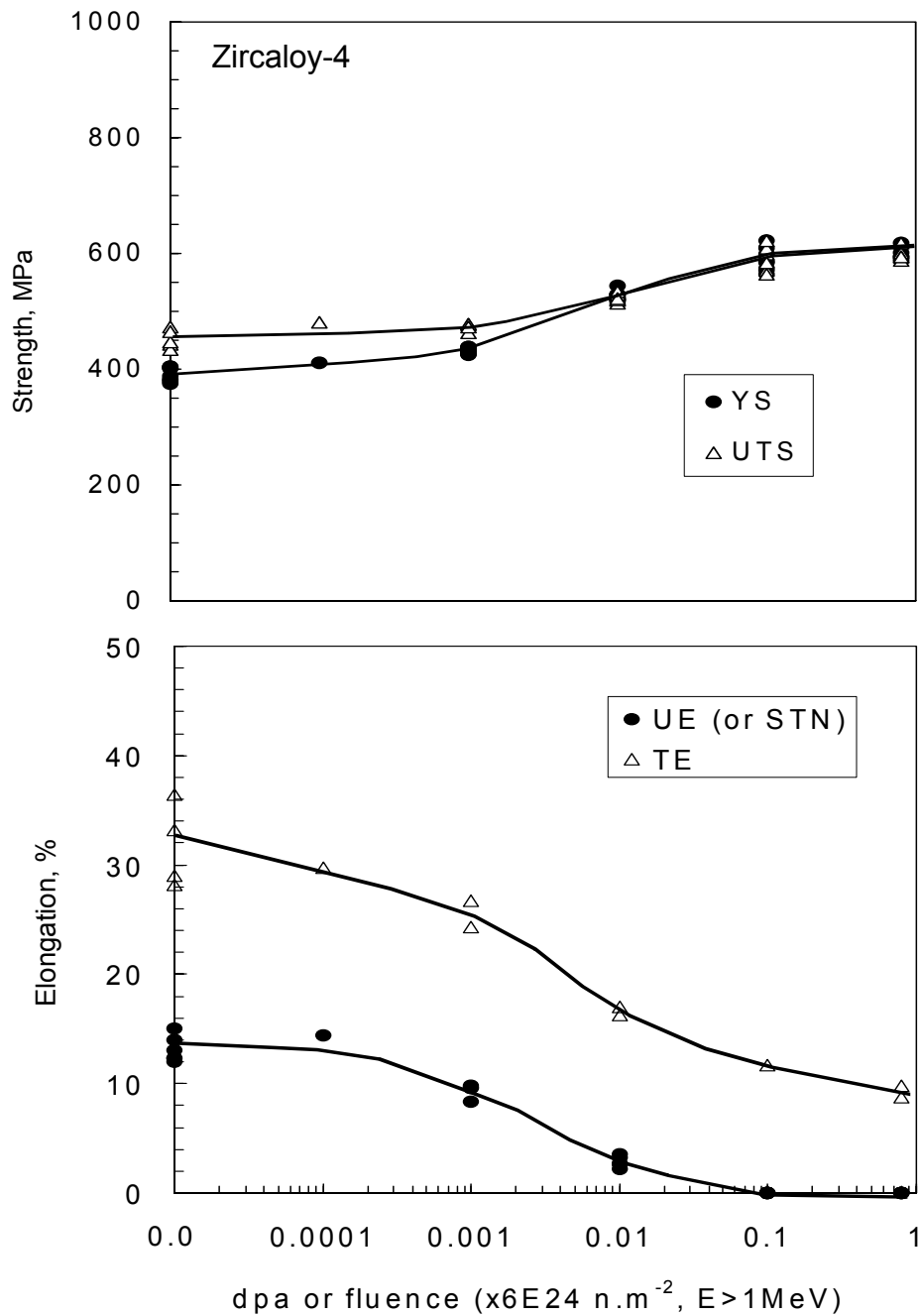
Fig. 13. Dose dependence of tensile properties of neutron irradiated Zircaloy-4.

At 0.1dpa and 0.8 dpa, the dislocation channels were much more obvious, Fig. 16. Within individual grains there tended to be only one slip system, $\{10\bar{1}0\}<11\bar{2}0>$, and cross channels were rare. The major channels were uniformly 40-75 nm wide and were spaced at 400-1100 nm. Between the major channels were relatively few narrow ones, < 30 nm wide. (Note: In an earlier

progress report on these findings [14] the major slip channels were erroneously reported to be on the $\{0001\}<11\bar{2}0>$ system.)

The deformation mode map derived for annealed Zr-4 from these observations is shown in Fig. 17.
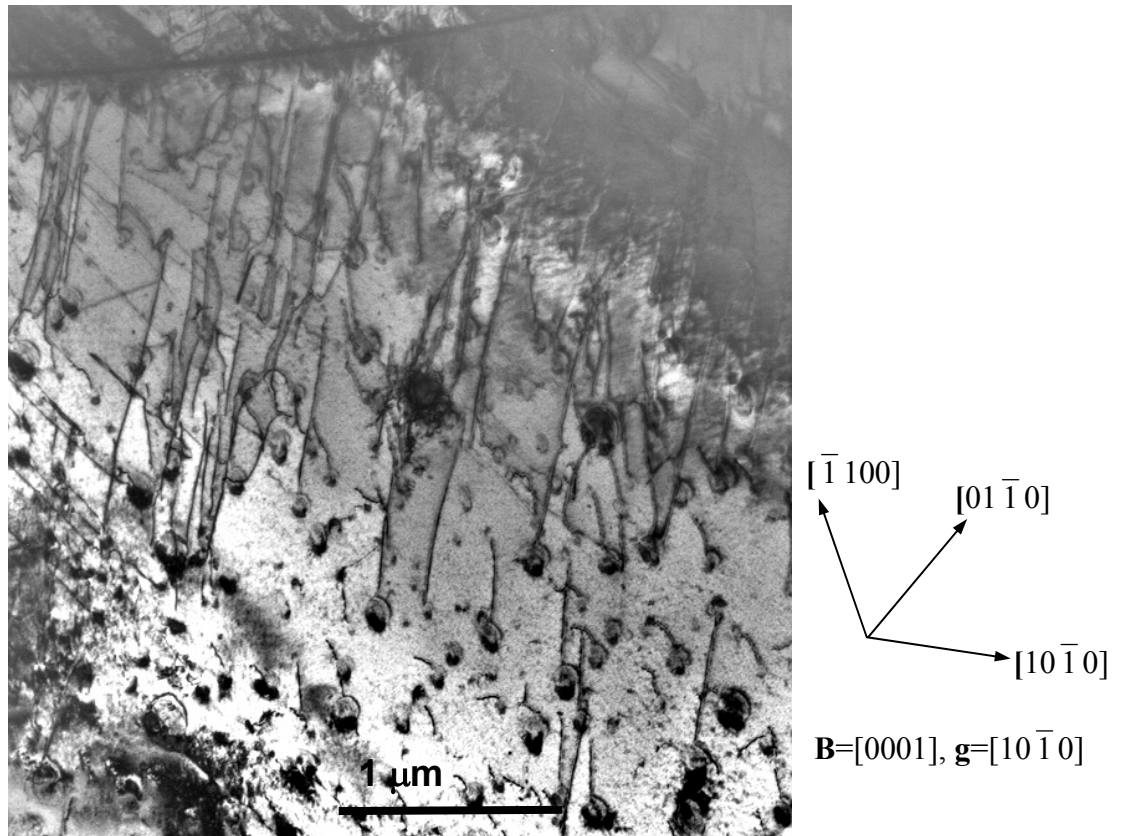
Fig. 14. Typical dislocation structure in unirradiated, deformed Zircaloy-4; at 3% strain.

(a)

200 nm

$[\bar{1}100]$

$[01\bar{1}0]$

$[10\bar{1}0]$

B=[0001], **g**=[10$\bar{1}$0]

(b)

200 nm
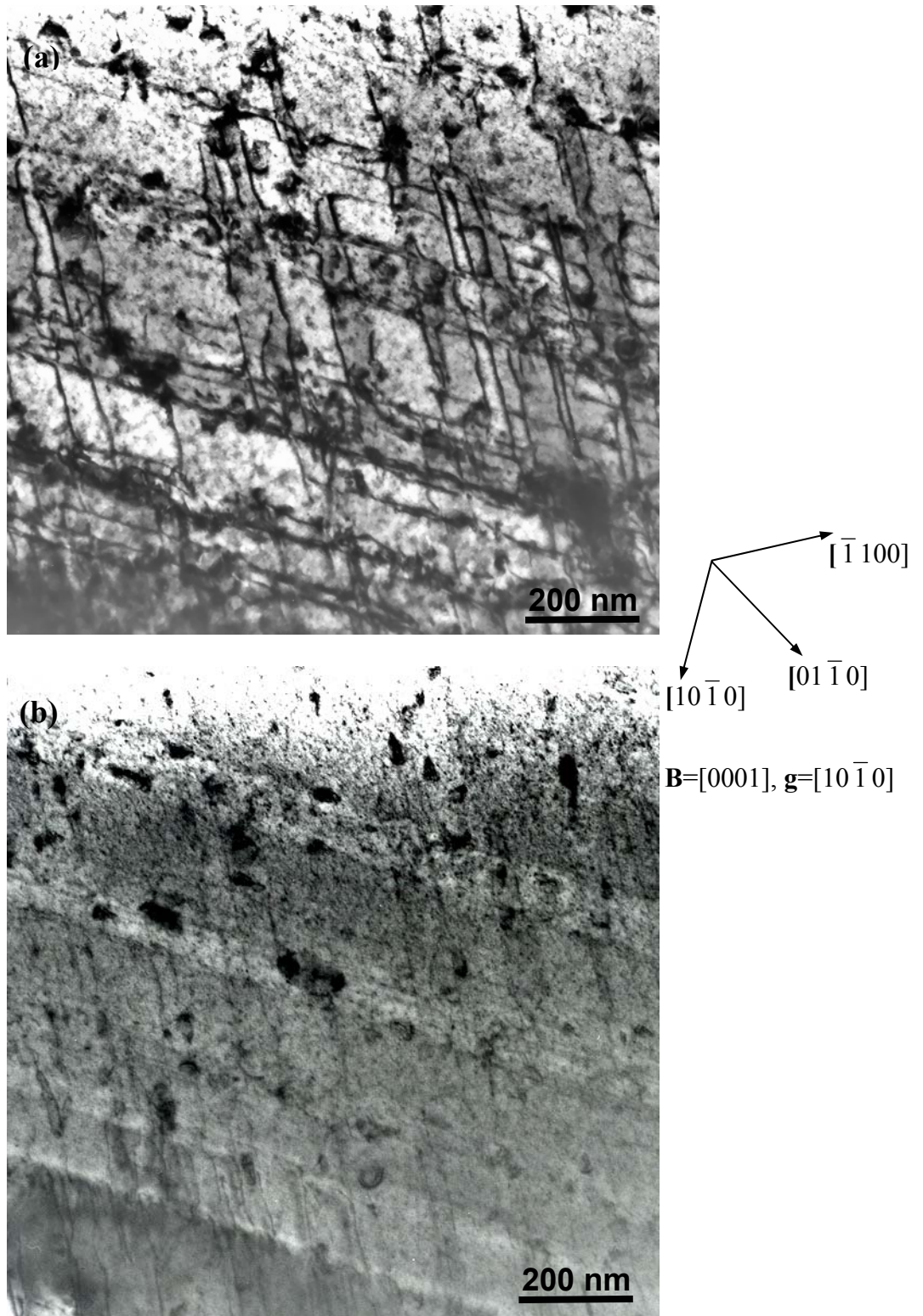
Fig. 15. Dislocation arrays in channels in Zircaloy-4 irradiated to 0.009 dpa and strained 4.8%;
(b) is slightly tilted from (a) to reveal the channels.
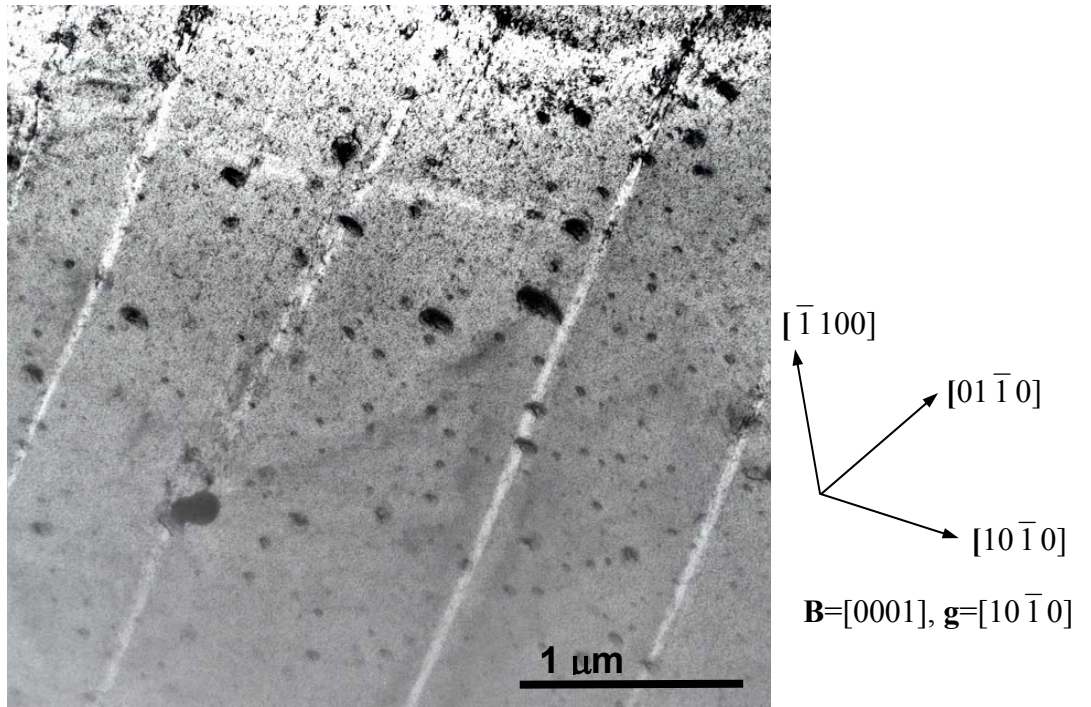
Fig. 16. Dislocation channels in Zircaloy-4 irradiated to 0.8 dpa and strained 6.3%.
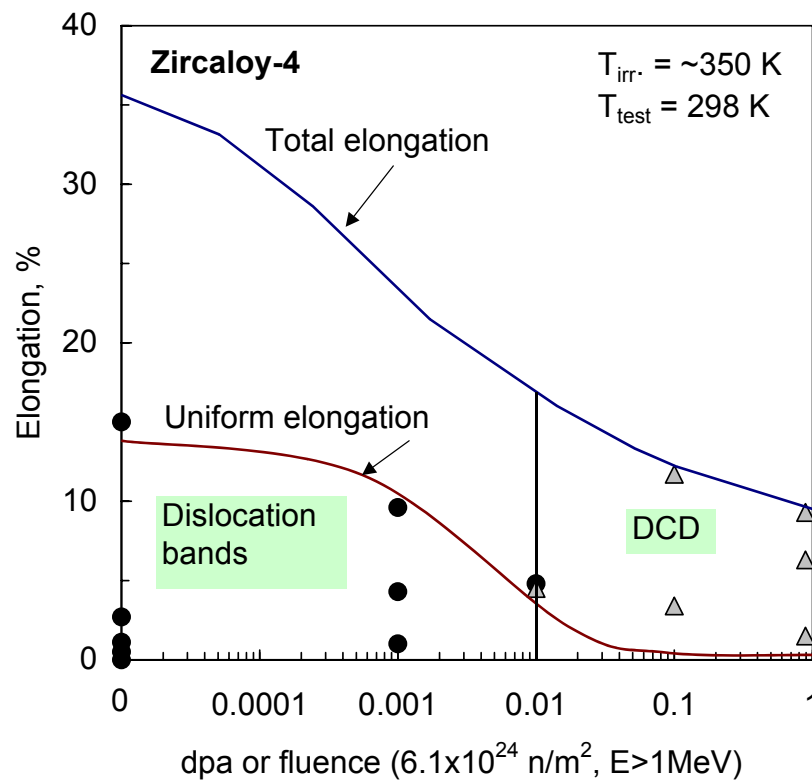
Fig. 17. Deformation mode map for Zircaloy-4 neutron-irradiated at 65-100ᵒC and tested at room temperature.

4.4 316 Austenitic Stainless Steel Results

In its unirradiated condition, the microstructure of as-annealed 316 steel consists of equiaxed grains containing some large annealing twins. The annealing twins are a consequence of the low stacking fault energy of austenitic steel. Irradiation to a dose of 0.0001 dpa did not reveal any RDS. For all other doses, black spot RDS was clearly evident. Figs. 18(a) – 18(d) show the defect size distributions. The mean size of the clusters varies little with dose and is about 1.6 nm. Cluster concentrations are of order 1×10^{23} m^{-3} and they increase by a factor of about 5 over the dose range 0.001 to 0.8 dpa.

316 SS, 0.001 dpa
Defect density = 0.74 X 10^{23} m^{-3}
Mean diameter = 1.5 nm
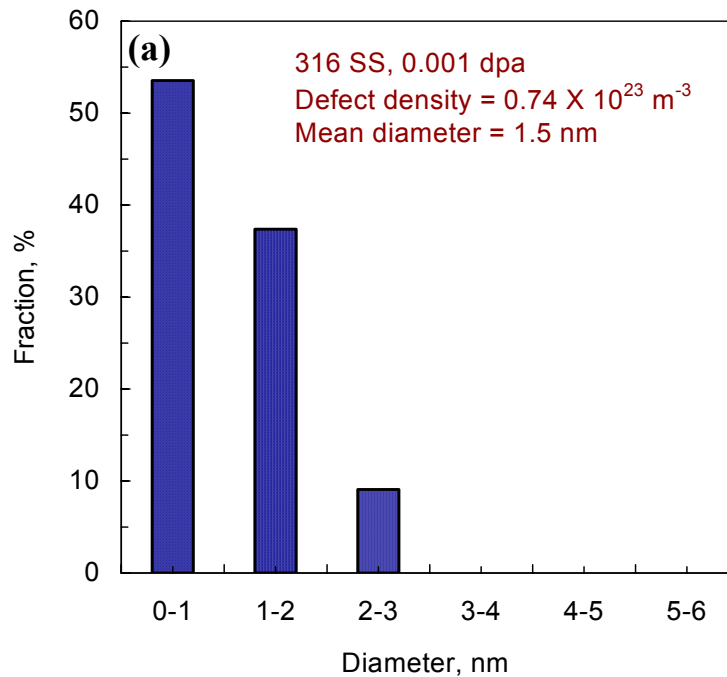
Fig. 18. Size distributions of black spot RDS in 316 stainless steel after irradiation to (a) 0.001, (b) 0.01, (c) 0.17, and (d) 0.78 dpa.

(b)

316 SS, 0.17 dpa
Defect density = 1.0×10^{23} m^{-3}
Mean diameter = 1.6 nm

(c)

316 SS, 0.01dpa
Defect density = 0.81×10^{23} m^{-3}
Mean diameter = 0.8 nm
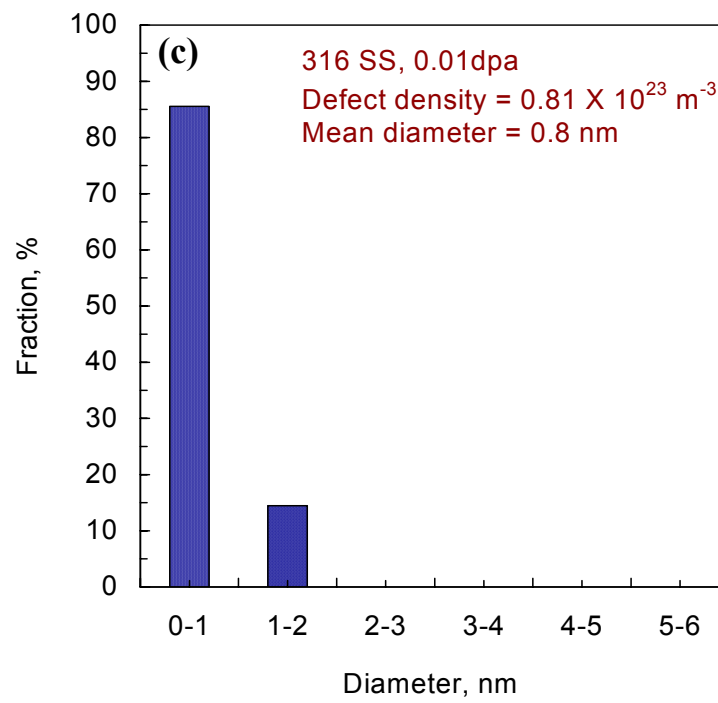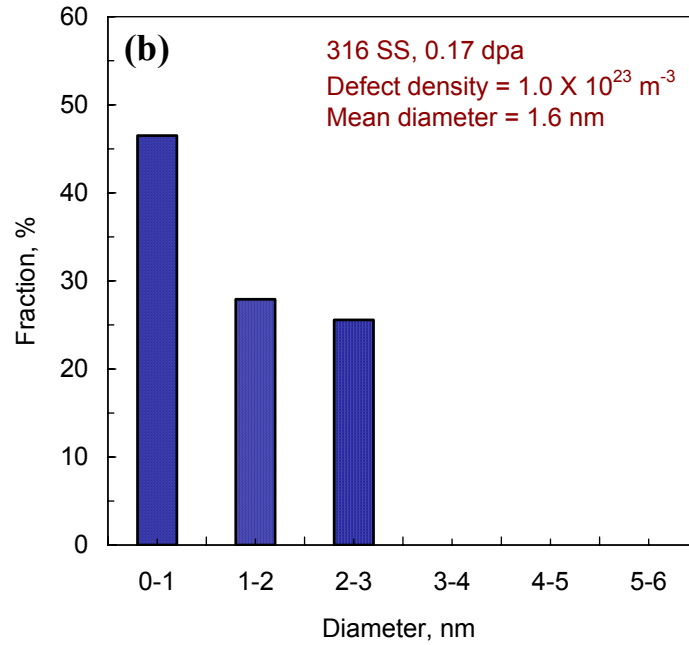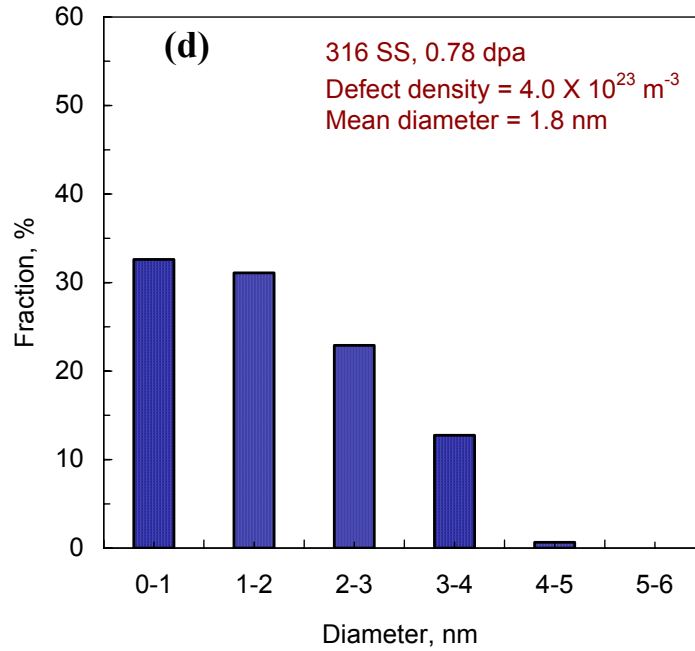
Fig. 18. (continued)

Fig. 18. (continued)
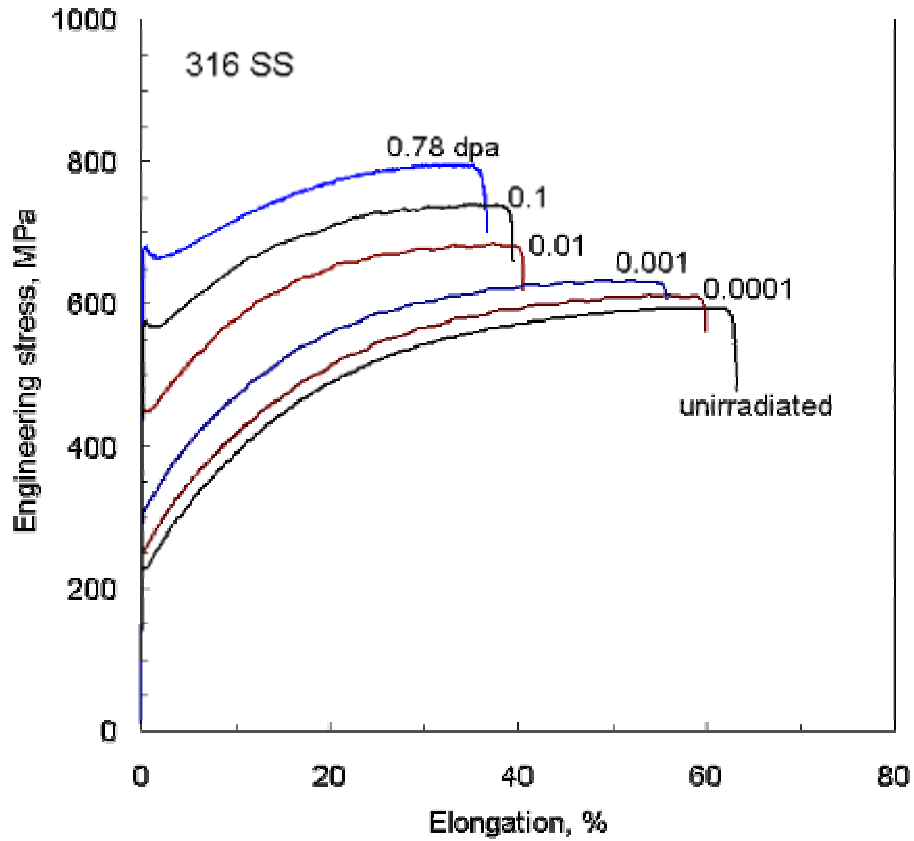
Fig. 19. Representative tensile curves for 316 stainless steel.

Tensile test curves for the annealed 316 austenitic stainless steel specimens are displayed in Fig. 19. The curves are very similar to those reported for 304, 316, and 347 stainless steel irradiated elsewhere at ~50°C to similar doses with larger specimens [15]. In all these stainless steels, there is no yield point drop in the unirradiated materials and in those irradiated to the lower fluences. A yield point drop is introduced at an exposure of about 6 x 10^{22} n.m^{-2} (~0.01 dpa) and it increases in size with increasing dose. The present 316 steel behaves in the same way. There is a small yield inflection but no yield point drop in the unirradiated material and at the two lower fluences. The yield stress is raised a little by the irradiation but there is not much effect on the work hardening rate which remains around 1600 MPa, Table 3. This rate is less than for A533B steel and more than for Zr-4. At the middle dose of 0.01 dpa, there is little change in work hardening rate in the stainless steel, contrary to the large decreases seen in the A533B steel and the Zr-4, Table 3. At the two highest doses the rate is reduced for the 316 steel, but not to the severe extents observed in the other two materials. There is no negative work hardening and no prompt plastic instability failure in the stainless steel, even at the highest dose.

The dose dependence of the tensile properties is given in Fig. 20. For the low dose irradiations, the yield strength is raised a little and there are small decreases in elongation. At the higher doses, there is substantial increase in yield strength. However, the elongation suffers only relatively mild loss, in sharp contrast to the large ductility losses seen in the A533B steel and the Zr-4.

With regard to deformation mode, the unirradiated 316 steel deforms by slip on {111}<110> systems. At low strains of 1% or so, the dislocations are primarily in planar arrays, Fig. 21. Short lengths of stacking fault fringes are frequently visible in the dislocations. As the strain level increases the arrays thicken into bands on {111}<110>, and random, tangled dislocations appear in the matrix between the bands. With increasing strain, the slip bands became more pronounced and at about 5% elongation, the appearance of streaks in electron diffraction patterns indicated the occurrence of fine twins. Dark field illumination using the twin streaks placed the fine twins in the slip bands. Such fine deformation twins are created by overlapping of the stacking faults of extended dislocations on consecutive slip planes in the slip bands, as described in Refs. 16-18. This twinning is not an instantaneous process as in mechanical twinning, and no twinning discontinuities are seen in the stress-strain curves. At high strains of 50% or so, the twins are very evident in the microstructure, Fig. 22.

After irradiation to the two lower doses, no change in deformation mode was observed. At doses up to 0.01 dpa, there was still no appreciable distinction between the deformation modes for unirradiated and irradiated specimens. Even at the higher doses there is no radical change in deformation mode; rather, the nature of the deformation remains the same but the degree of damage is altered subtly. Twins show up in the dislocation bands at lower strains than in the unirradiated specimens. At a dose of about 0.1 dpa, the dislocation bands are replaced by narrow channels in which the RDS has been largely erased, Fig. 23. Most of the channels contain deformation twins and some glide dislocations, but a small portion of the channels seem to be clear of all structure no matter how much the TEM specimen is tilted in attempts to reveal features in the channels. Offsets are seen at channel intersections, and there is substantial dislocation activity at the junctions. Furthermore, some of the clear channels are curved,

departing at an angle of about 7.5° from the major channels. Numerous short cross channels, like ladder rungs, connect the major channels. There are tangled dislocations in the spaces between the channels, and their presence does not seem to have affected the black spot RDS there. Many of the channels are present in the earliest stages of straining, and they proliferate with strain. Large stacking faults and twins are present in the channels even at low strain levels. At the highest dose of 0.79 dpa, the channels carve the deformation microstructure into subdivided tetrahedral blocks, Fig. 24.
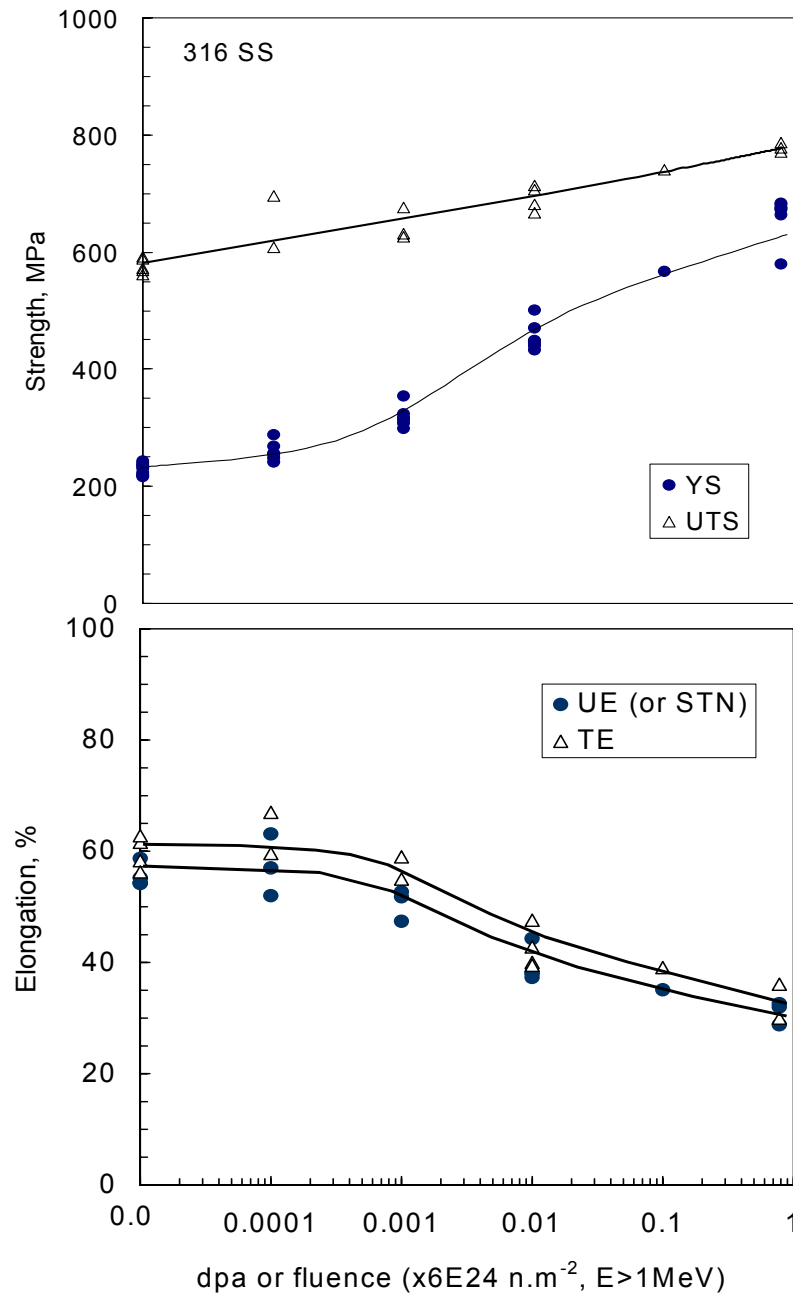
Fig. 20. Fluence dependence of the tensile properties of annealed 316 stainless steel.

32
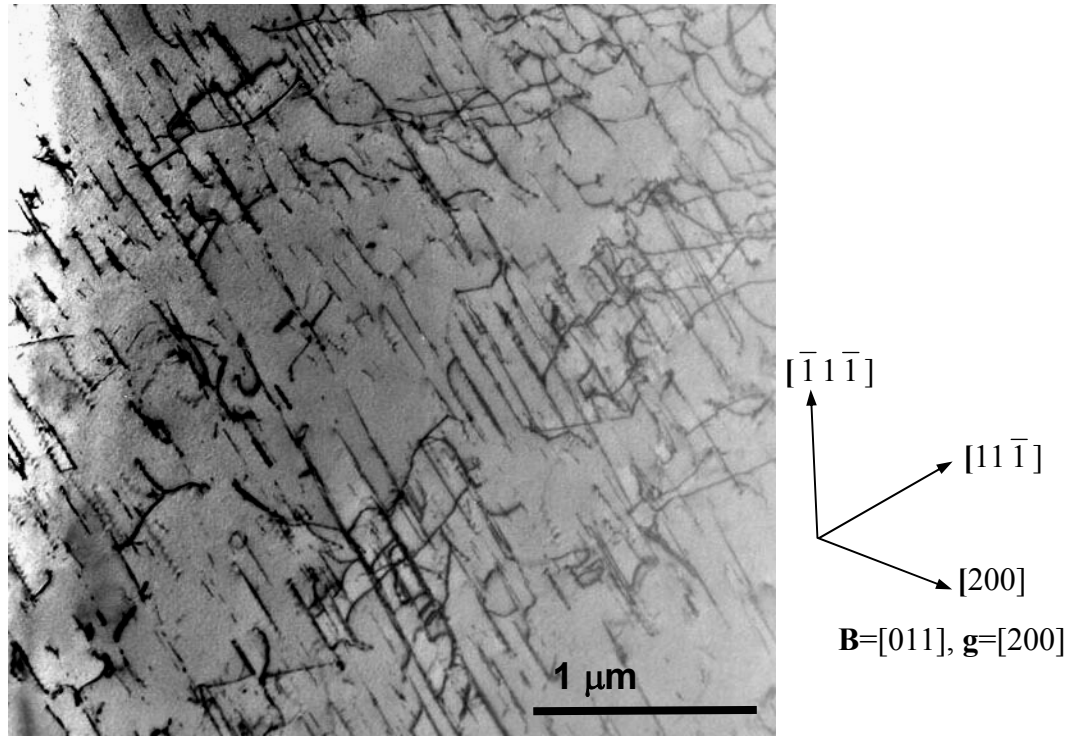
Fig. 21. Planar deformation in unirradiated stainless steel strained 1.5% at room temperature.
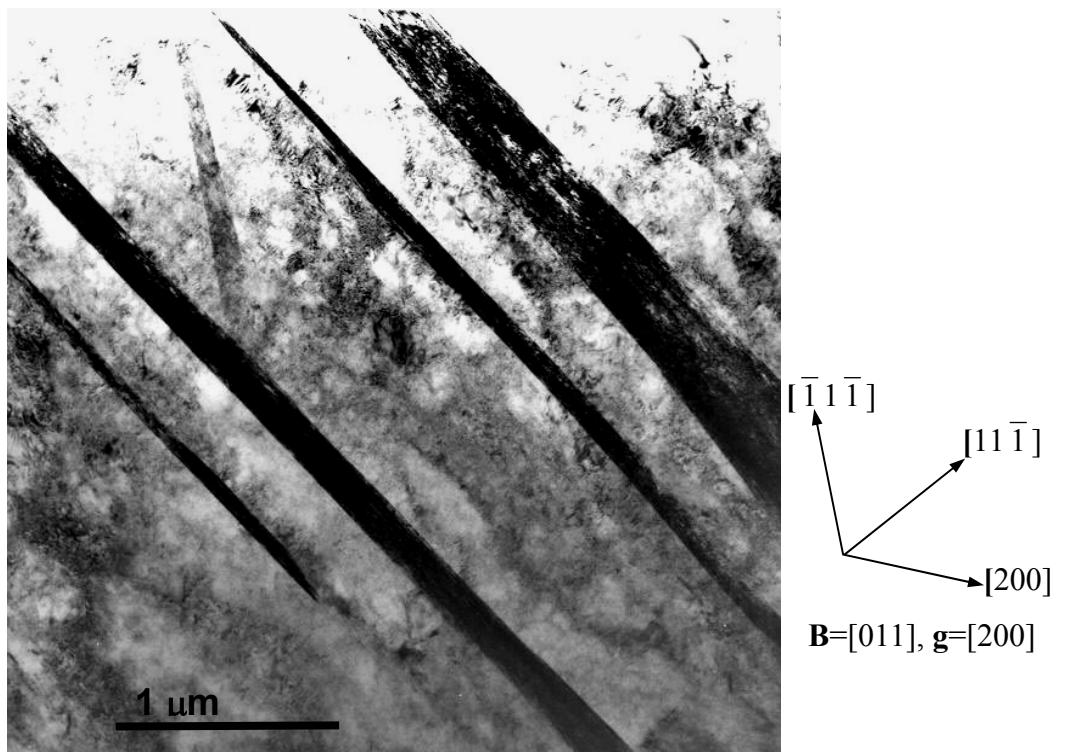
Fig. 22. Deformation twins in unirradiated 316 stainless steel strained 54% at room temperature.
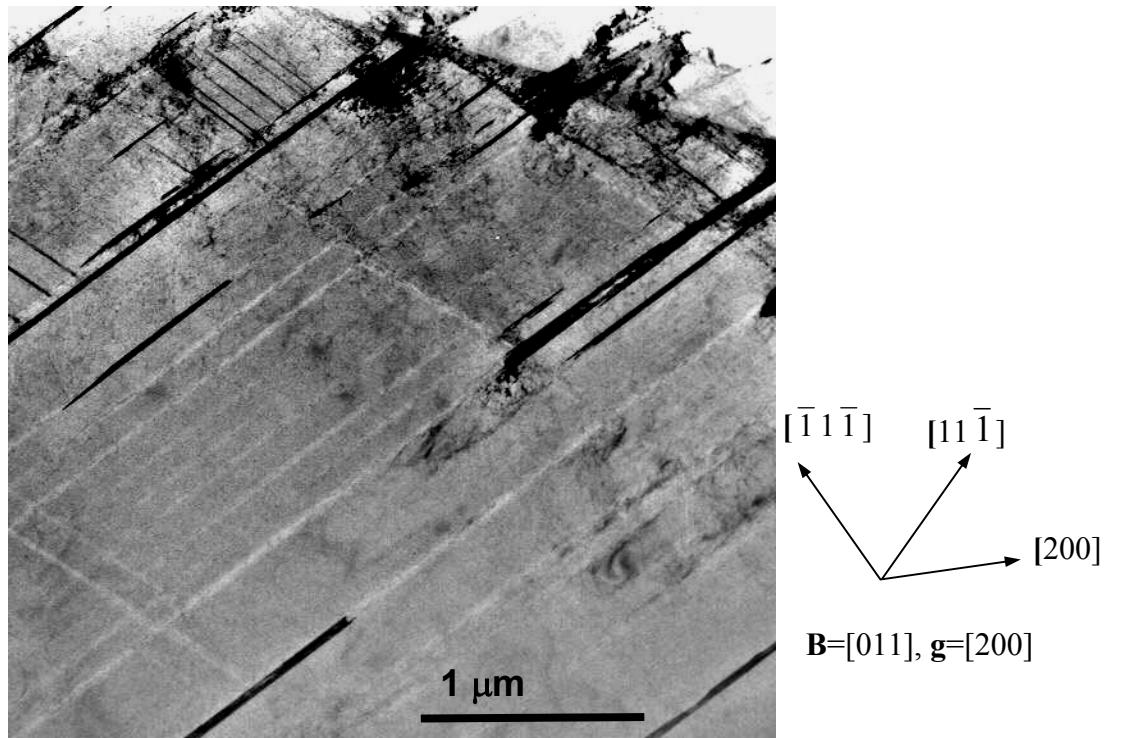
Fig. 23. Dislocation channels in 316 stainless steel irradiated to 0.15 dpa and strained 6%.
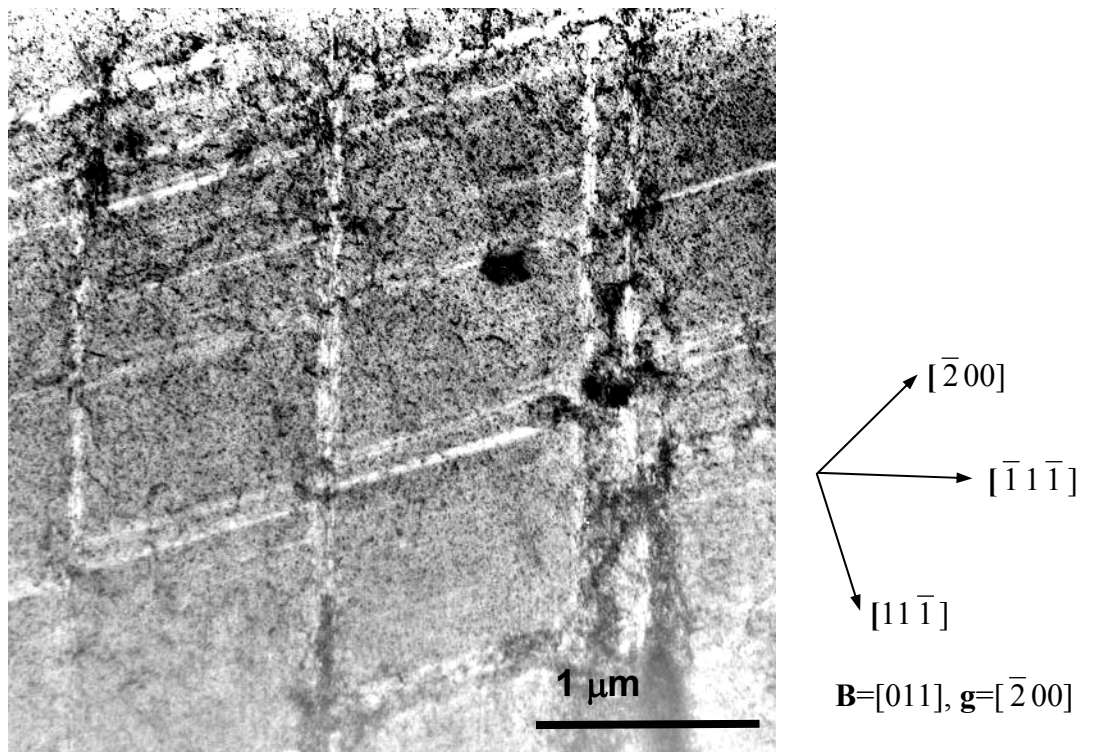
Fig. 24. Blocky arrangement of dislocation channels in 316 stainless steel irradiated to 0.78 dpa and strained 32%.

Measurements of channel widths and spacings at the two highest doses are presented in Table 4. Considerable grain-to-grain variation was found, and although attempts were made to choose typical grains it is acknowledged that there is significant uncertainty. Even within a single grain there was high deviation. Despite these qualifiers it can be seen that both the channel width and the spacing increase with dose, indicating fewer but wider channels at the higher doses. These results agree with the expectation that at higher doses deformation becomes more localized and confined. With regard to effects of strain, the channel width increases slightly as the strain increases, but no meaningful change is found in the channel spacing.

Table 4. Channel widths and spacings in irradiated 316 stainless steel.

Dose, dpa	Strain, %	Channel width, nm		Channel spacing, nm	
		Mean	Deviation	Mean	Deviation
0.17	6	10	5	284	200
0.78	2	26	6	622	433
	5	24	5	535	246
	32	19	11	588	306

Closer examination of the larger blocks between the major channels reveals that some of them are riddled with vague, fragmented channels lying parallel to the major channels, Fig. 25. There are also numerous extremely narrow, straight channels that are very difficult to resolve; they correspond to the locations of large stacking faults or microtwins. Dislocation tangling within the blocks is diminished.

The deformation mode map derived for annealed 316 austenitic stainless from these observations is shown in Fig. 26.
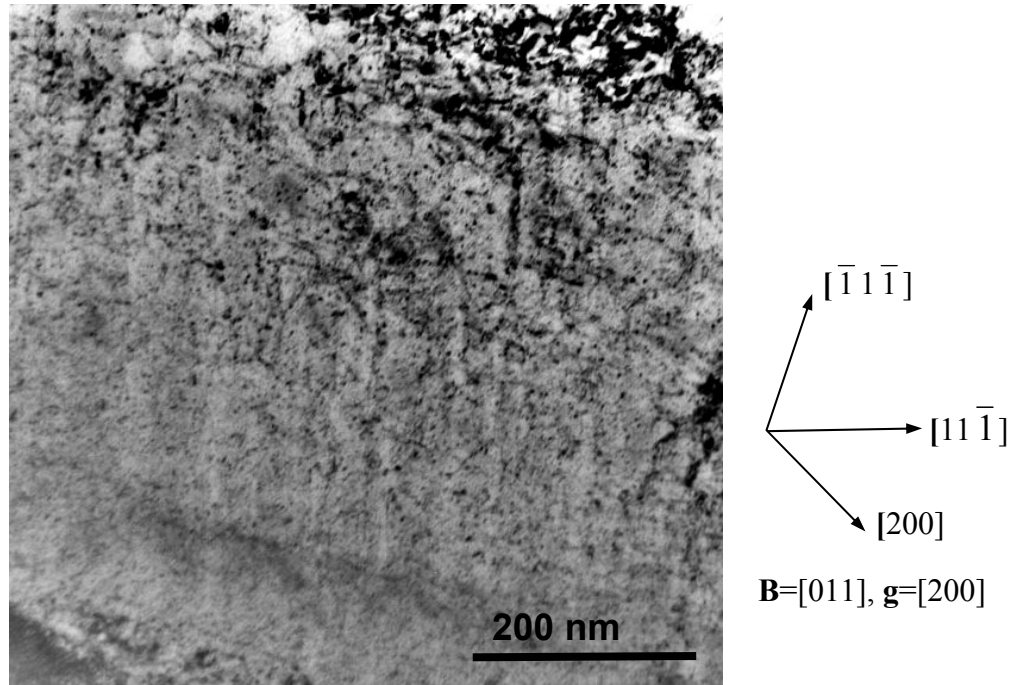
Fig. 25. Fragmented channels within the blocks in 316 stainless steel irradiated to 0.78 dpa and strained 32%.
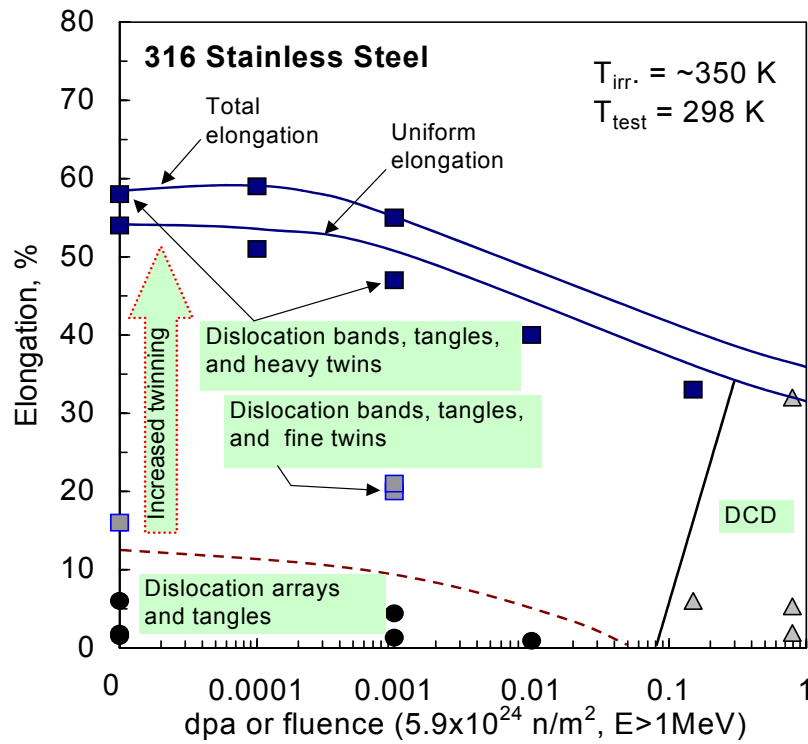
Fig. 26. Deformation mode map for 316 austenitic stainless steel neutron-irradiated at 65-100°C and tested at room temperature.

4.5 Discussion of Phase 1 and 2 Findings
This work has produced the first ever deformation mode maps for neutron irradiated reactor structural alloys, shown in Figs. 10, 17, and 26 for A533B ferritic steel, Zr-4, and 316 austenitic stainless steel, respectively. These maps identify the major modes of plastic deformation operating during tensile tests of irradiated materials at room temperature. The boundaries of the deformation regimes are outlined in terms of neutron fluence and plastic elongation. The data are sparse but they provide the map frameworks for subsequent fleshing out as more data become available.

Four deformation modes are recognized; namely, dislocation tangling and cell formation; banding or planar deformation; dislocation channel deformation (DCD); and deformation microtwinning. Deformation by dislocation tangling and cell formation is the normal mode in most unirradiated metals. It develops from a three-dimensional interaction of dislocations resulting from cross slip and impingement of dislocations on intersecting slip planes. It occurs to some extent in all three materials herein, whether irradiated or not. It is the dominant mode in the A533B steel for doses below 0.1 dpa. It competes with DCD and is depressed when DCD is strong. Dislocation banding, or planar deformation, represents confinement of dislocation activity to a limited number of slip planes. It is a normal mode of deformation where a single slip system is dominant, as in Zircaloy-4, or where dislocation cross slip is diminished, as in the 316 steel. Diminished cross slip is a consequence of the low stacking fault energy of austenitic steel, as discussed later. Planar dislocation deformation is encouraged by irradiation. The planar arrays are considered to be precursors of DCD but are not a prerequisite for DCD. DCD is not found in any of the three alloys before irradiation. It is seen in all three alloys after irradiation, but not at the lower neutron fluences. Deformation microtwinning is seen only in the austenitic steel. It occurs before and after irradiation and is a result of low stacking fault energy; it is encouraged by irradiation.

Regarding the tensile curves and tensile properties, a pattern is noted in which changes in properties induced by irradiation near room temperature fall into two regimes of fluence dependence. The first regime is at low fluences and is characterized by minor reductions in elongations and by small increases in yield strengths without introduction of yield point drops. In this regime, the deformation modes are the same as those for the unirradiated material; work hardening rates are unchanged, and there are no overt signs of DCD. The second regime is at fluences of 0.01 dpa and higher, and is distinguished by large increases in yield strengths, introduction or enhancement of yield point drops, large decreases in elongations, and significant reductions in macroscopic work hardening rates. In this higher fluence regime, DCD is involved. In the 316 steel, there is increased microtwinning activity in addition to the DCD. For all three alloys the losses in ductility due to irradiation are associated primarily with reductions in uniform elongation. Except for the A533B steel at the two highest doses, the necking strains, i.e. the differences between the total elongation and the uniform elongation, are barely affected by the irradiation. The implication is that the tensile properties are most impacted by the changes in the work hardening regions prior to reaching the UTS.

It is seen, then, that DCD is the only deformation mode induced by irradiation. Furthermore, the incidence of DCD coincides most closely with the larger irradiation-induced changes in the tensile curves. That coincidence is not accidental. It represents an intimate connection between

channeling and alteration of tensile properties, in conformation with similar relationships established elsewhere in both irradiated and unirradiated materials. Strain localization is not peculiar to irradiated materials. It is quite common in unirradiated materials, where it is referred to as work softening. It is usually preceded by a yield point drop, after which deformation initially proceeds locally at low work hardening rate. Work softening involving swept-out dislocation channels is encountered in materials that have been prehardened by cold straining [3, 19, 20], by quenching [21, 22], or by some precipitates [23, 24]. Perhaps the best-known example is the strong yield point and related Lüders bands seen in mild steels. The features of non-uniform deformation found in the first tensile tests conducted on a neutron irradiated metal, single crystal copper, reported in 1960 [6], were likened to Lüders bands. The deformation bands in irradiated copper were subsequently shown to be DCD [4, 25,26]. Similar findings were subsequently made for irradiated molybdenum [27]. In short, DCD seen in irradiated metals is a facet of the broader phenomenon of work softening.

Explanations of the yield point drop and associated strain localization in work softening are plentiful. They include sudden release of dislocations from locked sources [28], rapid multiplication and movement of dislocations [29], geometrical softening [30], and adiabatic heating [5]. The underlying premises are that the prehardening treatments have locked the dislocation sources, which then require higher stresses to activate them. When the first sources are activated they send avalanches of dislocations sweeping through the barriers ahead of them, clearing softened pathways. A general observation is that the higher the yield stress at which plastic strain begins, the greater is the propensity for channeling. It has been proposed [31] that the character of slip correlates more systematically with stress than with any other parameter, and that focused or localized slip is favored by high stresses. It is also well known that the velocity of glide dislocations increases exponentially with stress [29], which invokes high strain rates in channels. Indeed, high speed photography of the surface slip lines resulting from DCD has shown that they develop very rapidly, in less than a millisecond [32, 33]. Details of the barrier clearing process(es) are specific to particular types of barriers and are still very much debatable. It is generally agreed that once the initial channels are formed, less force is required to maintain the machine crosshead speed, hence the stress drops. Under the reduced stress, activation of additional sources is denied and dislocation activity in the surrounding stronger matrix is suppressed; therefore, deformation is restricted to the cleared channel regions until work hardening at channel/channel and channel/grain boundary intersections raises the stress. The removal of dislocation barriers in the channels reduces the work hardening rate in the channels, which is signaled in the tensile curve as an apparent decrease in bulk work hardening. The degree of reduction in work hardening will depend on the extent to which DCD is involved.

Whatever the basic mechanism(s) of strain localization processes, the symptoms of work softening in the tensile curve and the simultaneous occurrence of local bands of deformation in TEM are similar to those seen in the present work. It is very clear, too, that the propensity for DCD is greater the higher the yield strength, which in turn is a function of neutron dose. These observations leave little doubt that the DCD found herein is associated with, and probably responsible for, the yield point drops and reductions in work hardening rates. The "little doubt" centers on the data for doses of 0.01 and 0.1 dpa in the A533B steel. Strong yield point drops and severely reduced work hardening were seen for these cases but no DCD was found. It is our opinion that DCD did occur in these two instances but its detection in TEM was thwarted by an

invisibility curtain. The problem is that at these doses and the low irradiation temperature the size of the RDS in iron and steels is submicroscopic in TEM, i. e. the average defect cluster size is less than 1 nm. These small clusters have been detected by other techniques of atom probe microscopy, small angle neutron scattering, and positron annihilation. Also, coarsened clusters can be seen in TEM if the material is post-irradiation annealed to a temperature of 300-400°C [34-36] or if the material is irradiated at 290°C [37, 38]. At such higher temperatures thermal diffusion processes are enhanced and are sufficient to enable the clusters to grow to visible sizes. For the present study the size of the RDS in A533B steel at a dose of 0.1 dpa and less is below the TEM resolution limit of about 1 nm. Consequently, since the RDS can not be seen in TEM neither can dislocation channels, even if they are there en masse. The reason for this is that the visibility of a channel is determined by the difference in degree of scattering of the electron beam by the RDS in the channel and by the RDS in the adjacent matrix. In a channel, the RDS is erased or broken up by the passage of glide dislocations, and the resulting reduced electron scattering reveals the channel as a lighter-colored band in a TEM photographic print. However, if the matrix RDS is too small to be seen there will not be a detectable difference in scatter contrast between the matrix and a channel. Then the only hope of detecting such channels in TEM is to search for other evidence of channels such as straight surface slip steps and trails of dislocation debris left at the channel paths, particularly piled-up dislocations at the intersections of crossing channels. Unfortunately, the A533B specimens contained too many residual dislocations to permit reliable use of that technique. The technique has proved useful for exposing channel paths in annealed pure iron irradiated to neutron fluences as low as 1.5 x 10^{22}n.m^2, E>0.1 MeV, which is about 0.001 dpa, where no RDS was visible [39]. So the seeming absence of channel contrast in the low dose A533B specimens is not sufficient evidence that no channels are present. Another difficulty with the A533B steel, particularly at the higher doses, is the previously mentioned severity of the strain localization. The deformation occurred only in a very narrow necked region, not uniformly along the gauge length, and it was not possible to get satisfactory TEM pieces from the neck.

By and large, then, the major changes in tensile properties can be connected with the incidence of DCD, which is not unexpected in view of the aforementioned correlations for work softening. It seems, too, that changes in the tensile curve, principally the introduction of yield point drops and reductions in work hardening rate, may be more sensitive indicators of strain localization than TEM examinations, at least for the A533B steel. It might follow that the occurrence of a yield point drop coupled with reduced work hardening is a sure sign of strain localization. However, the opposite is not true. That is, the absence of a yield point drop and no significant reduction in work hardening rate does not necessarily signify an absence of strain localization. This was demonstrated clearly in the investigations [9] that produced the deformation maps for nickel and gold in Fig. 2. The corresponding tensile curves are shown in Fig. 27. Study of these curves shows that in the nickel none of the specimens that exhibited DCD displayed a yield point drop or significant reduction in work hardening rate. In the gold, all the irradiated specimens showed large reductions in work hardening whether they deformed by channeling or not, and only the highest fluence specimen had a yield point drop. The deformation mode in the nickel is notable in that it underwent a transition from dislocation cell type to a lamellar or planar band structure before cleared channels emerged. Such banding is, of course, a form of strain localization and can thus be expected to contribute to channel-like changes in the tensile curve.

Judging from the lack of symptoms in the tensile curves for the nickel, that contribution must be very subtle.

From the above discussion, the minimum dose at which DCD begins in the three alloys for irradiation at 65-100°C is about 0.01 dpa for Zr-4 and A533B steel, and between 0.01 and 0.1 dpa for the stainless steel. These are significantly higher doses than for the onset of DCD in pure nickel and gold. In Fig. 2 the occurrence of DCD in the nickel and gold begins at a fluence of about 1 x 10^{21}n.m^{-2}. The irradiations were conducted in the Rotating Target Neutron Source II at Lawrence Livermore National Laboratory where the D-T neutron energy is 14 MeV. For such high-energy neutrons, the atomic displacement cross sections are about ten times larger than for fission neutrons with energies >1MeV. A D-T neutron fluence of 1 x 10^{21}n.m^{-2} corresponds to about 0.004 dpa for medium atomic mass number metals like nickel [40]. Hence, the threshold displacement doses for DCD in the present alloys are 2.5 to 25 times higher than the thresholds for pure nickel and gold. Some of this difference may be due to differences in irradiation parameters such as neutron spectrum and damage rate. But most of the difference is probably attributable to differences in chemical compositions. The alloying additions and impurity elements in the alloys will reduce survival of point defects from displacement cascades and may promote greater recombination of freely migrating point defects, thereby reducing the development of RDS. Attainment of a critical yield stress for initiation of DCD would then be delayed to higher doses. Actually, it is not known what triggers DCD, whether it is achievement of a critical stress greater than the unirradiated yield strength, or a critical dislocation velocity, or a critical softening stress due to defect clearing. It is not even clear whether there is a true threshold of *any* kind for DCD.

Although no symptoms of DCD were seen at the lower fluences, it is quite conceivable that DCD is always awaiting its chances and is spurred by the mildest hardening treatment but needs to achieve a critical *presence* to become *noticed*. After all, the basic dislocation slip process itself is a heterogeneous deformation mode. It is not obvious whether there is a real threshold for DCD or whether the seeming absence of DCD at low fluences is because of inadequate sensitivity in our detection techniques.

In the present work, the stainless steel displays some of the dislocation banding, or cursory channeling behavior seen in the microstructural development of the channels in nickel. After a dose of 0.01 dpa a yield point drop is produced in the stainless steel but there is no associated decrease in work hardening rate. No channels are discerned but dislocation banding is more pronounced. At higher doses, dislocation channels are observed and they are narrower than those in the other two alloys at a given dose. Moreover, of the three alloys investigated here, the stainless steel is the only alloy that retains much of the channeling dislocations within the channels. The channels in stainless steel also contain fine microtwins, not seen in the other two alloys.
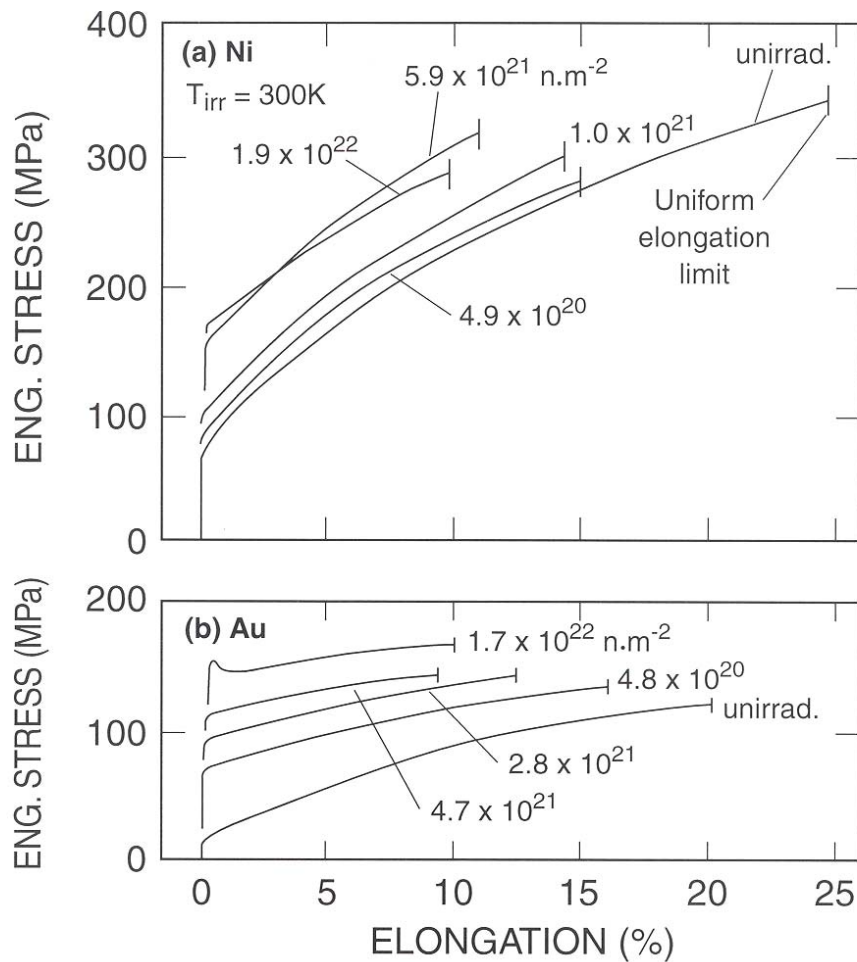
Fig. 27. Engineering tensile curves for the deformation mode maps in Fig. 2 [9].

Because of the low stacking fault energy of austenitic stainless steel, the partial dislocations that constitute a glide dislocation are more widely separated, or extended, than in higher stacking fault materials such as the A533B steel and Zr-4. The separation of the partials is just visible as a short ribbon of stacking fault fringes. For plastic deformation to occur the two partial dislocations must either glide as a pair or the leading partial must increase its separation from the trailing partial, creating a larger stacking fault. Before a dislocation can move off its primary slip plane onto a cross slip plane the stacking fault between the partials must first be compressed, which requires extra energy. Therefore, cross slip is suppressed and the deformation tends to be much more planar in stainless steel than in higher stacking fault materials.

The location of deformation twins within the slip bands in the stainless steel demonstrates that slip and deformation twinning in this material are not two separate processes; the twinning is a direct and coupled consequence of the planar slip. The twins are not the rapid, blocky type, accompanied by sharp drops in stress that are common in some metals during straining at low temperature. The twins in stainless steel occur gradually by dislocation slip and, as shown

elsewhere [38-40], they are formed by successive glides on adjacent slip planes. It is speculated here that retention of glide dislocations and twins in the channel/deformation bands moderates the activity of glide dislocations in the channels and dampens the build-up of excessive stresses and strains in the channel bands. This restricts the width of the channels and provides some work hardening capacity in them. This is probably one reason why the stainless steel has much more resistance to radiation-induced ductility loss than the other two alloys. Another reason could be that it is a legacy effect from the unirradiated conditions. The total elongation of the unirradiated stainless steel (63%) is much larger than those of the other two alloys, 20% for A533B and 33% for Zr-4. This superior elongation in the stainless steel stems largely from protracted uniform elongation, which comprises almost all of its total elongation, whereas in the other alloys the uniform elongations represent less than half of their total elongations. The feature that prolongs the uniform elongation of the stainless steel might be the microtwins, which develop within the deformation bands. Both the stainless steel and the Zr-4 deform by dislocation banding, which being a strain localization process should limit their elongations. But only the stainless steel develops microtwins in the bands. And the stainless steel is much more ductile than the Zircaloy. Because of its lower stacking fault energy the separation of partial dislocations in the 316 stainless steel is much higher than in the other two alloys, and they contain significant stacking fault ribbons even though they may not always be easily noticeable in the unirradiated material at low strains. Their presence makes cross-slip more difficult, and is the reason that dislocation glide motions are confined to narrower bands in the stainless steel. In these narrow bands dislocation pileups occur more readily, which generates more back stress hardening and encourages activation of new slip sources. Additionally, the higher stresses cause greater separation of the partials, producing wider stacking faults [41]. These faults are precursors of the deformation twins found in the bands. Since the faults and twins are formed progressively with strain, they can continue to prolong work hardening. On these grounds it is proposed here that the stacking faults and twins are responsible for the superior elongation of the stainless steel in both its irradiated and unirradiated conditions.

Zirconium alloys undergo slip primarily on {0001} basal, {10$\bar{1}$0} prism, and {10$\bar{1}$1} pyramidal planes, in a common <11$\bar{2}$0> direction. Mechanical twinning can occur together with slip. No twins were seen in the Zircaloy-4 in the present work, presumably because of a lack of suitable texture. Zirconium alloys develop strong textures during forming operations. In tension tests the dominant deformation mode is dependent on the processing texture. In rolled sheet, the basal planes become aligned in the plane of the sheet and are tilted slightly in the rolling direction. If the tensile specimen is machined in the thickness (T) direction, such that its basal planes lie nearly perpendicular to the tensile axis, it will deform by a mixture of non-basal slips and gross mechanical twinning. Some of the twins will be suitably reoriented for slip to occur in them. If the tensile specimen is taken in the longitudinal forming direction (L), it will deform primarily by slip. In the present work, the tensile specimens were machined in the rolling direction, L type, and no twins were seen in the tensile tests. In literature reports of DCD in zirconium alloys, some of the specimens were of T type and they displayed mechanical twinning during tensile testing [42]. The twins were of the massive, lenticular type. Formation of these broad deformation twins did not remove RDS and cause DCD, but slip bands occurring within the twins did. Interestingly, during those tests, which were made after a fluence of 4 x 10^{23}n.m^{-2},

E>1MeV, the occurrence of DCD did not seem to be sensitive to material composition; it was found in iodide zirconium, Zircaloy-2, and Zr-2.3Nb.

A final point of discussion of these Phase 1 and 2 data is the increases in yield strengths caused by the irradiations. Historically, the earliest radiation strengthening data were obtained on copper [6] and were found empirically to fit an equation of the form $\Delta YS = \alpha(\varphi t)^{1/3}$ over a wide range of doses, where ΔYS is the increase in critical shear stress or macro yield strength, and φt is the neutron fluence or flux-time product. It was quickly pointed out [43] that the data could equally well fit the equation with an exponent of ½, which was the expectation for a hardening model involving hindrance of glide dislocations on slip planes by a random distribution of point defect clusters. The model assumes the volume fraction of clusters varies linearly with fluence. This assumption was later challenged when analysis of cluster densities in pure copper [44] indicated they were linear with fluence only at very low fluences below about 5×10^{20} n m^{-2}, corresponding to about 0.0001 dpa, above which they varied with $(\varphi t)^{1/2}$. Subsequent analysis [45] of a broader range of copper data from many sources showed that for doses above about 0.0001 dpa the cluster density exponent might be 1 or ½, depending on interstitial impurity content. A cluster exponent of ½ would make $\Delta YS = \alpha(\varphi t)^{1/4}$ It is recognized that all of these relationships will fail at higher doses due to saturation in formation of clusters caused by overlapping of displacement cascades and by absorption of freely migrating point defects at existing clusters. For copper [44], such saturation is estimated to occur at a dose of about 0.1 dpa [44] and it is seen at about 0.1 dpa [45,46]. For iron, cluster saturation is deduced to occur at 0.01-0.04 dpa [47,48] but is not seen until at least 0.5 dpa [46].

The tensile data obtained in the present work afforded an opportunity to test these predictions. In Fig. 28 the increases in yield strengths are plotted against fast neutron fluence in log-log coordinates. There are obvious signs of saturation of hardening at the highest fluence, so the data were arbitrarily analyzed as low and high dose groups. The results of a least squares line-fitting analyses are shown in Table 5. To make the α values compatible with literature data, the analysis was done with φt in units of n.cm^{-2}, E>1MeV. At the lower doses the slope is essentially ½ for all three materials irrespective of their large differences in crystal structures, chemical compositions, and microstructures. At fluences above 6×10^{18} - 6×10^{19} n. cm^{-2}, corresponding to displacement doses of 0.01-0.1 dpa for all three materials, the hardening exponent is reduced to the order of 0.1. Historically, such a decrease in hardening exponent would be taken as an indication that saturation of point defect clusters was occurring at doses above 0.01-0.1 dpa. To check the role of point defect clusters, the black spot defect densities, N_c, measured on the tensile specimens were plotted as $N_c = \alpha'(\varphi t)^n$ in log-log coordinates, Fig. 29.
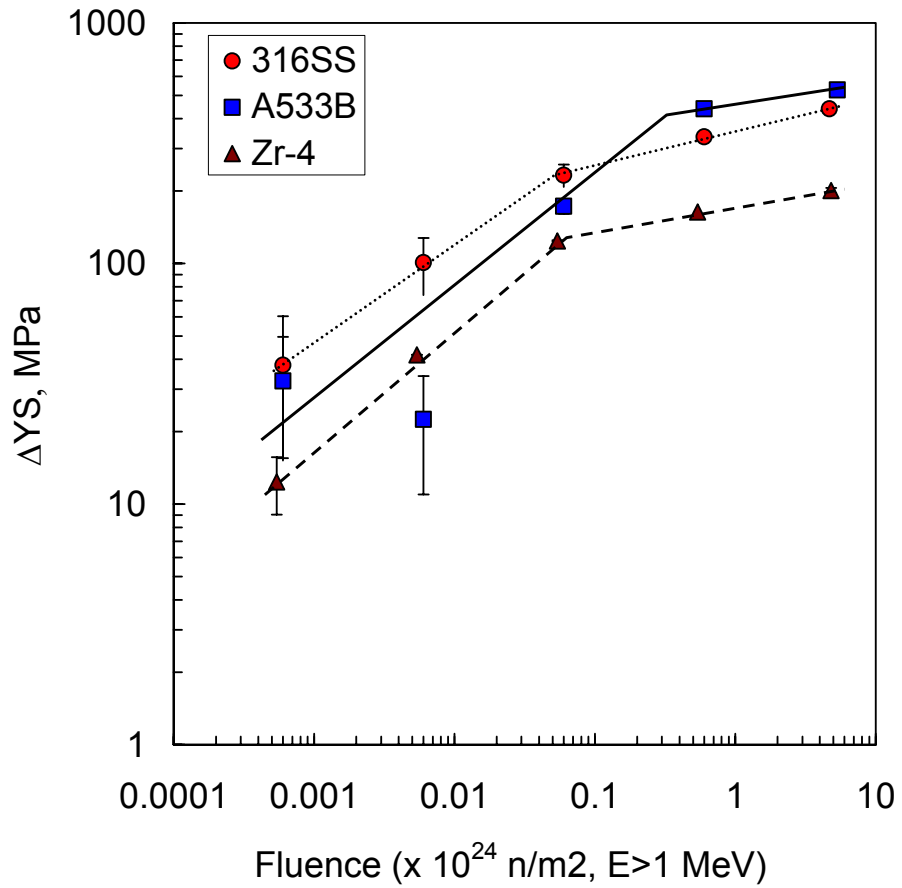
Fig. 28. Determination of radiation hardening exponents for the three alloys.

Table 5. Fitting parameters for radiation hardening equation $\Delta YS = \alpha(\varphi t)^n$.

Alloy	Low dose regime		Higher dose regime	
	α_1	n_1	α_2	n_2
A533b	5.45×10^{-8}	0.43	5.53	0.08
Zr-4	1.26×10^{-9}	0.5	0.54	0.11
316ss	2.43×10^{-7}	0.4	0.11	0.15
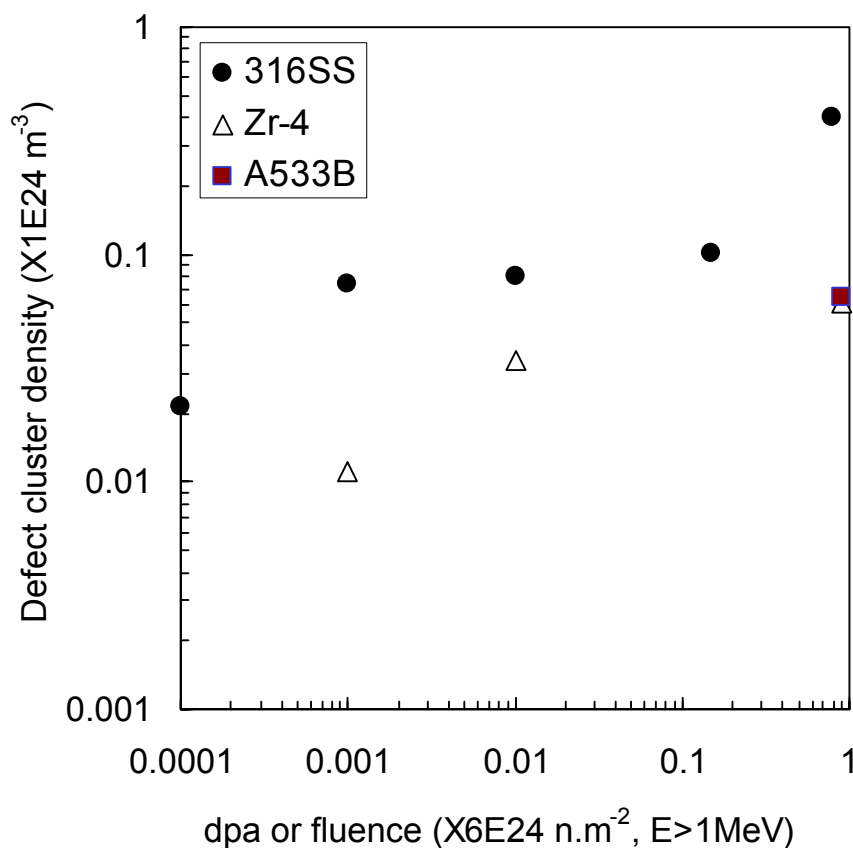
Fig. 29. Variation of black spot defect densities with irradiation dose.

There is only one datum for the A533B steel, which precludes determination of a slope or a saturation dose. The data for the stainless steel show no evidence of saturation, and a straight line drawn through the data would have a slope or exponent of order 0.25. Such a slope would be the lowest exponent ever measured for damage accumulation. It is decidedly at odds with established slopes of 0.5 and 1.0 for other fcc materials [44,45]. The cluster densities for the stainless steel are appreciably lower than those reported elsewhere for 316 stainless steel irradiated to similar doses at similar temperature [49]. In view of these discrepancies, it is considered that the cluster density data for the stainless steel are inconclusive for providing a firm relationship between cluster density and dose and for indicating an unambiguous saturation dose. The defect cluster measurements for the Zr-4 alloy are sparse but could be represented by a line of slope about 0.5 through the two lower fluence data, declining to a lesser slope above 0.01 dpa. This break in slope would be loosely compatible with the change in slope of the change in yield strength, Fig. 28.

As mentioned earlier, the marked reductions in slope of the change in yield strength with radiation dose at about 0.05 dpa in Fig. 28 could be due to achievement of saturation in damage microstructure. They might also be associated with a change in deformation mode. The

reductions in slope coincide with the occurrence of pronounced yield point drops and reductions in work hardening at and above 0.05 dpa. Those features and the dislocation channels found with them can not be attributed to dispersed barrier hardening. They are symptomatic of DCD. Since there is nothing to indicate that barrier hardening and DCD should share the same hardening exponent, it is postulated that intervention by DCD may be a significant factor in the reduced rate of radiation hardening in the higher dose regime. A similar conclusion was recently made for reduced radiation hardening found at doses above 0.05 dpa in ferritic/martensitic steels [50].

5.0 Phase 3

Phase 3 of the program covered irradiations and tensile tests made at higher temperature than for Phases 1 and 2. The goal temperature was 288°C, which is the operating temperature of the ferritic steel pressure vessels of light water power reactors. In austenitic stainless steels there is a region of high radiation hardening and low ductility for irradiations and tests conducted at around 300°C [51-58]. Most of such irradiations have been made to doses >>1 dpa, and DCD has been observed in the low ductility specimens [54, 58-60]. DCD also occurs in specimens of stainless steel strained after high dose rate ion bombardments at irradiation temperature up to 500°C and doses of 1-10 dpa where the radiation damage microstructures are similar to those for neutron irradiations at temperatures around 300°C [61-64]. There are no systematic studies of the dose dependence of radiation hardening and deformation behavior of stainless steels neutron irradiated to doses below 1 dpa at about 300°C and tested at about 300°C.The present tests were intended to address that shortcoming. In Zircaloy, radiation-induced strengthening can be greater for irradiations and tests made at 280-300°C [65,66] than for those made at room temperature; at doses of about 0.1-1.0 dpa low ductility occurs via plastic instability associated with DCD [42,67,68]. It was hoped that these Phase 3 tests would throw more light on this issue. Since little is known about the influence of strain rate on DCD in any metal, strain rate was one of the parameters investigated in these Phase 3 tests.

5.1 Results

The Phase 3 specimens were irradiated in March 2002 during the first fuel cycle following a prolonged shutdown of HFIR for scheduled major maintenance and upgrade. The goal exposures were 6 x 10^{23}n.m^{-2} (0.1 dpa) and 5 x 10^{24}n.m^{-2} (0.8 dpa). The timing of the irradiations was later than originally intended because the reactor was out of service for longer than planned. This meant that the specimens had to be tested immediately after irradiation in order to meet the program schedule. Consequently, there was not enough time to allow the 0.8 dpa specimens to undergo radioactive decay to reduce their radioactivities below the radiation limit posted for entry into the out-of-cell test laboratory. In anticipation of this dilemma, and to compensate for possible shelving of the 0.8 dpa specimens after irradiation, a third rabbit with a full complement of specimens was irradiated to a dose of 0.01 dpa where the radioactivity level would pose no problem but which would still give specimens satisfactory for our purposes. Published data [54] for the tensile properties of neutron irradiated austenitic stainless steel indicated that a dose of 0.01 dpa at 300°C would give increases in YS of about 170 MPa in 300°C tests, and deformation would occur by dislocation channeling. In fact, even at doses as low as 0.001dpa at 290°C in 316 stainless steel, radiation damage microstructure [51] and increases in YS [51,69] are observed.

As expected, the 0.8 dpa specimens were too radioactive for immediate testing. The 0.1 dpa and 0.01 dpa specimens were tested at 288°C and a strain rate of $10^{-3}s^{-1}$. Radiation effects on strength and ductility were found to be minor or not detectable. No consistent irradiation strengthening or reductions in elongations were discerned for the A533B steel and the stainless steel, Figs. 30 and 31. Small increases in YS and UTS, and small decreases in elongations, were detected in Zr-4, Fig. 32. (Note that in these figures, and in subsequent Phase 3 figures, the irradiation temperature is indicated as ~350°C. The reason for this, as shall be explained shortly, is that the actual temperature is believed to have inadvertently exceeded the goal temperature of 288°C.)
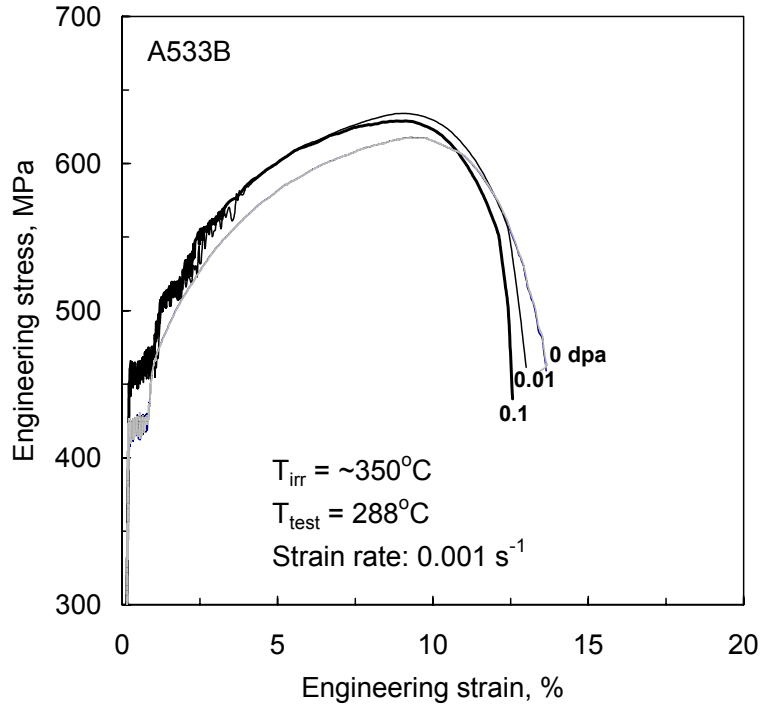
Fig. 30. Examples of engineering tensile curves for A533B steel irradiated to 0, 0.01, and 0.1 dpa at ~350°C and tested at 288°C.
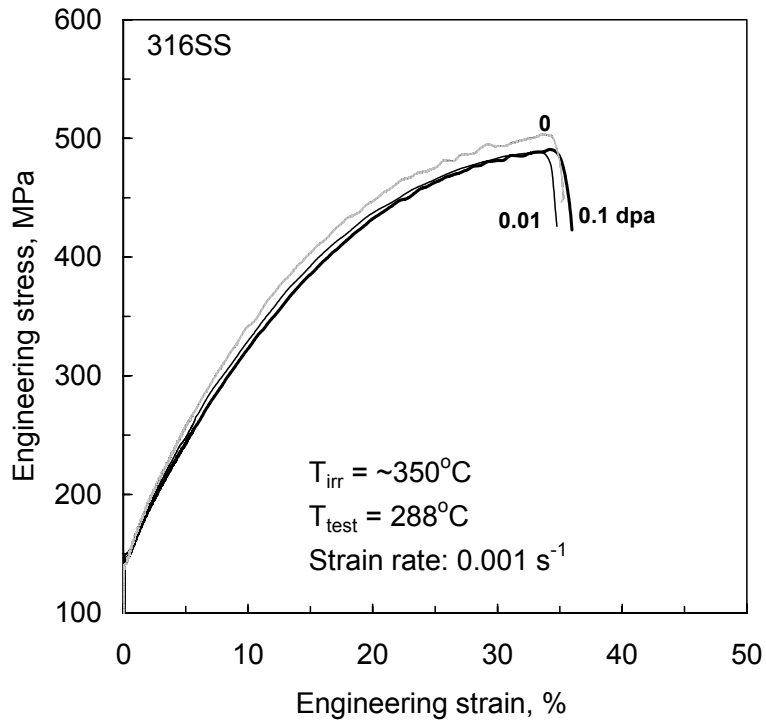
Fig. 31. Examples of engineering tensile curves for 316 stainless steel irradiated to 0, 0.01, and 0.1 dpa at ~350°C and tested at 288°C.
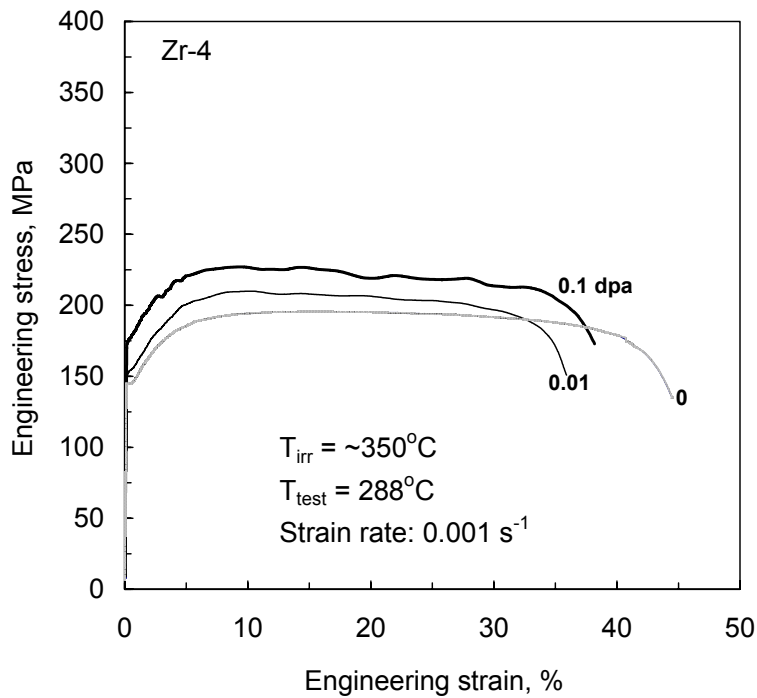
Fig. 32. Examples of engineering tensile curves for Zircaloy-4 irradiated to 0, 0.01, and 0.1 dpa at~ 350°C and tested at 288°C.

None of the tensile curves displayed features that could flag the occurrence of DCD, such as yield point drops, reduced work hardening, or prompt plastic instabilities. The tensile curves for the A533B steel, both irradiated and unirradiated, displayed Lüders strain regions containing high-frequency stress serrations. The irradiated specimens had slightly higher yield strengths and also contained high-frequency stress serrations in the first few percent of elongation beyond the Lüders region. The unirradiated specimen, which was not aged to simulate the irradiation temperature, did not contain the post-Lüders serrations. The high frequency serrations are characteristic of dynamic strain aging, which is common in ferritic steels during testing at temperatures around 300°C, and is due to interaction of mobile carbon atoms with glide dislocations. The presence of more serrations in the irradiated specimens indicates that they were encouraged by the irradiation treatment. Presumably the irradiation temperature and/or atomic displacements during irradiation caused more carbon to be taken into solution. To confirm the lack of radiation hardening, tests were made at room temperature on 0.1 dpa specimens of each alloy. Such low temperature tests should avoid dynamic strain aging and should increase the sensitivity of detection of irradiation-induced changes in yield strength. No serrations were seen, and no significant evidence of irradiation hardening was detected.

Increasing the strain rate by factors up to a thousand fold did not reveal any further effects of irradiation hardening in any of the alloys, Figs. 33-35. The A533B steel, irradiated and unirraditated, displayed a small increase in YS with increasing strain rate, and a decrease in UTS, Fig. 33. That is a common response to strain rate for bcc metals when dynamic strain aging is present. The 316 stainless steel had small increases in yield strength and UTS, Fig. 34. The YS and UTS of Zr-4 alloy, irradiated and unirradiated, were raised considerably by increased strain rate, Fig. 35. Concurrently, elongation values were reduced; the uniform elongation in Zr-4 fell to almost zero at the highest strain rate for a dose of 0.1 dpa. The full program of tensile tests was completed for the Phase 3 specimens with detection of only minor irradiation hardening effects. The tensile data for these elevated temperature irradiations are compiled in Table A4-2.
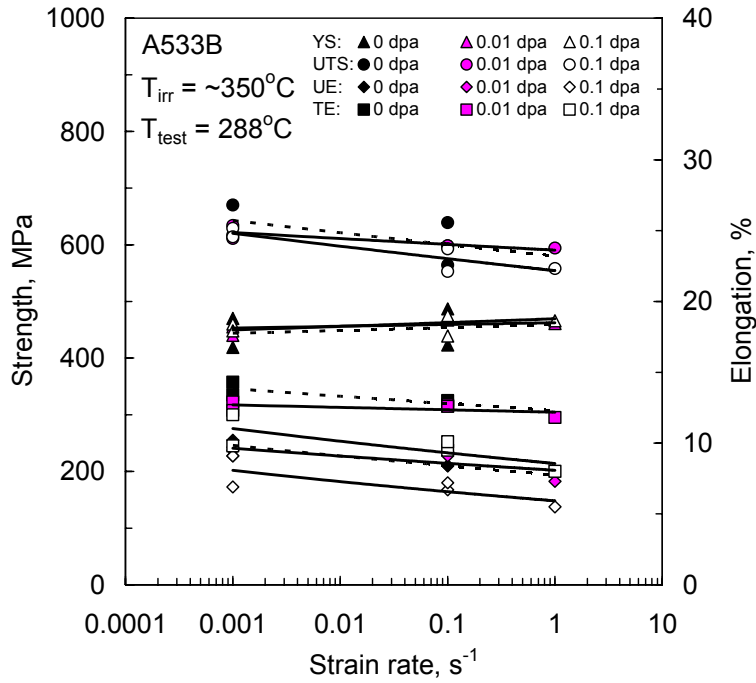
Fig. 33. Strain rate dependence of tensile properties of A533B steel irradiated at~ 350ºC and tested at 288ºC.
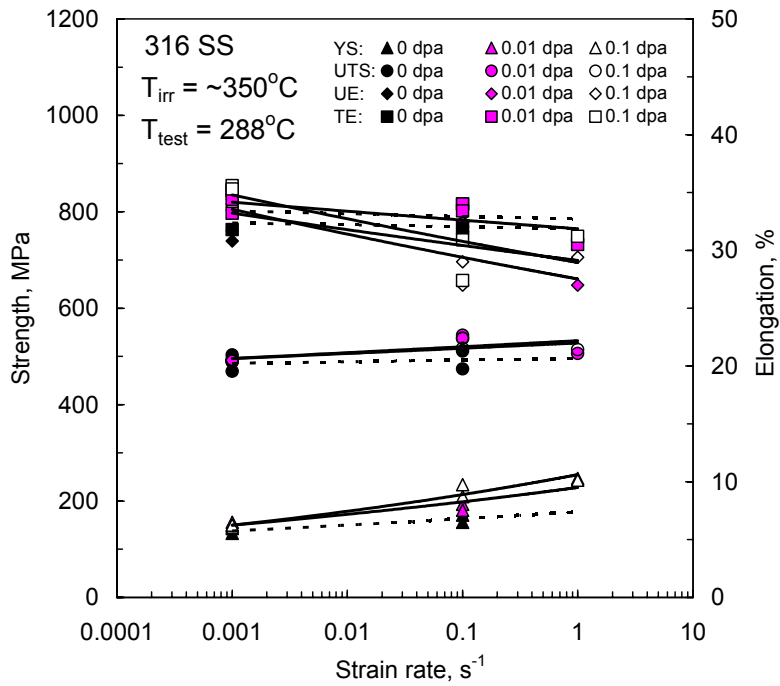
Fig. 34. Strain rate dependence of tensile properties of 316 stainless steel irradiated at ~350ºC and tested at 288ºC.
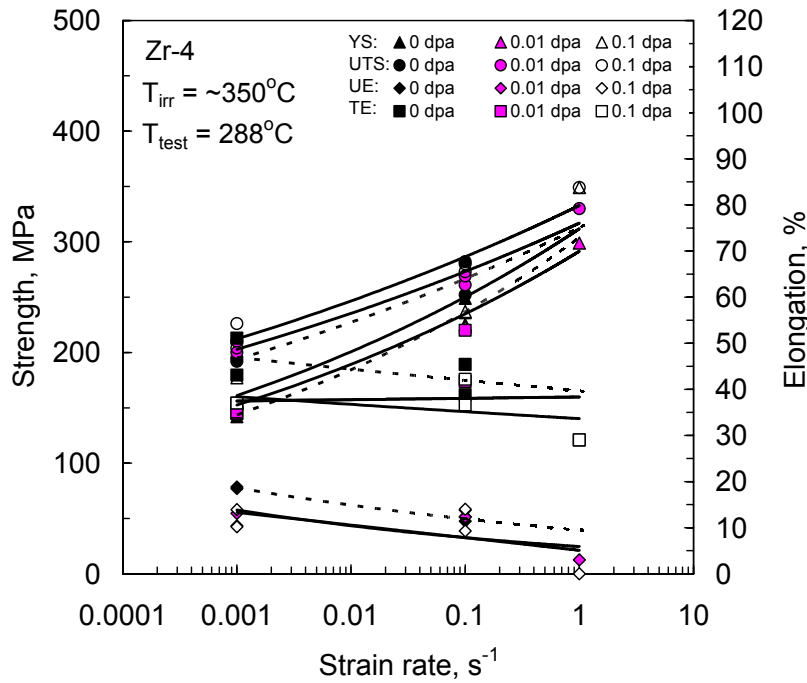
Fig. 35. Strain rate dependence of tensile properties of Zircaloy-4 irradiated at ~350ºC and tested at 288ºC.

There were no other overt signs of radiation damage. TEM examinations of the gauge sections of the tested tensile specimens of A533B and 316 stainless steel showed no signs of radiation damage microstructure and no dislocation channeling. In a TEM disk of 316 steel, taken from one of the TEM blanks irradiated to 0.1 dpa, there was a low density of dislocation loops, 3.6 x 10^{21} m^{-3}, with mean size of 2.1nm, Fig. 36. One Zr-4 tensile specimen irradiated to 0.1 dpa and strained 5%, contained patches of black spot radiation damage at a concentration of 2.5 x 10^{21} m^{-3} and mean size 6.5nm, and tangles of glide dislocations, Fig. 37, but there were no dislocation channels.

During disassembly of the rabbits it was found that many of the passive SiC temperature detectors were broken. Nevertheless, there were sufficient whole detectors available to permit analyses to extract their irradiation temperature. The technique utilizes the principle that irradiation displacement damage and transmutation products decrease the electrical resistivity of the SiC. Post-irradiation annealing of a detector above the irradiation temperature removes the displacement damage and restores much of the original resistivity. The temperature at which recovery commences is taken to correspond with the irradiation temperature. This technique has been verified quantitatively in radiation experiments containing thermocouples [70] and is considered to be accurate within 20ºC. The resistivity of each detector was first measured in the as-irradiated condition using a four-point probe. It was then heated for 30 min. at a temperature well below the goal irradiation temperature and remeasured. This cycle was repeated at progressively higher temperatures until considerable and steady increase in resistivity was

established. Examples of recovery curves for three detectors from the 0.1dpa rabbit are shown in Fig. 38. The onset of recovery is well defined in each detector and indicates an irradiation temperature of 280°C for all three detectors. The initial differences in resistivity for the three detectors, as-irradiated, are believed to be a legacy from the unirradiated condition where microcracks from the machining operations cause detector-to-detector variations. The resistivities of unirradiated detectors were scattered around 400 Ω-m, and were independent of annealing temperature. This measured temperature of 280°C is higher than planned. As discussed later, the SiC temperature detectors were in contact with a heat sink and were intended to operate at about 220°C. The 60°C excess temperature measured on them implies that the irradiation temperatures of the tensile specimens would also have been about 60°C higher than intended.
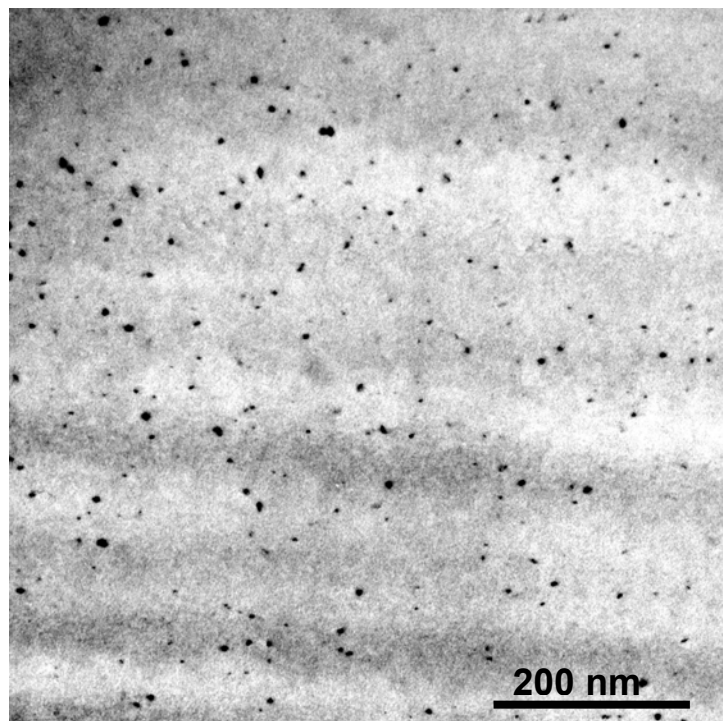
Fig. 36. Black spot radiation damage in 316 austenitic stainless steel TEM disk specimen as-irradiated to 0.1 dpa at~ 350°C.
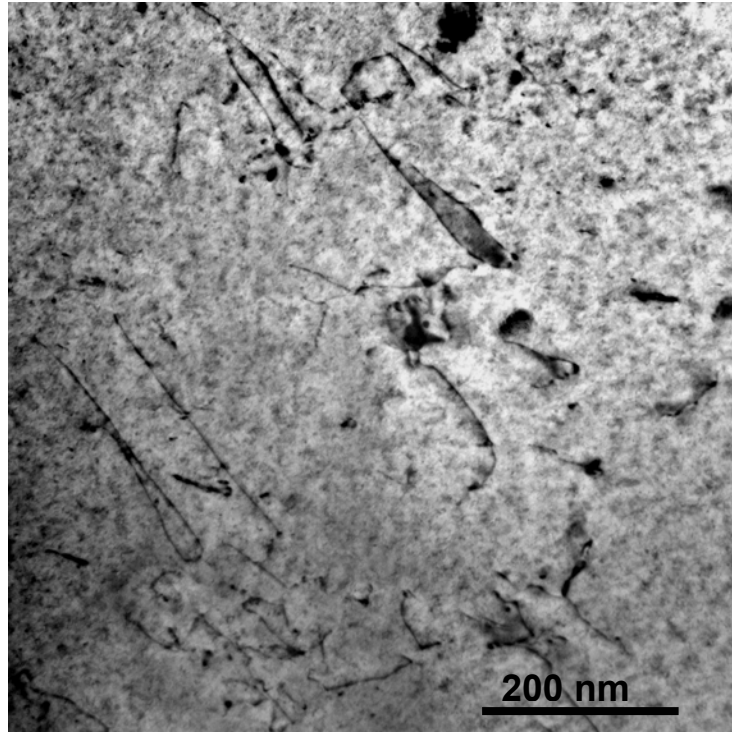
Fig. 37. Black spot radiation damage in a Zircaloy-4 tensile specimen irradiated to 0.1 dpa at ~350^oC and strained 5% at 288^oC.
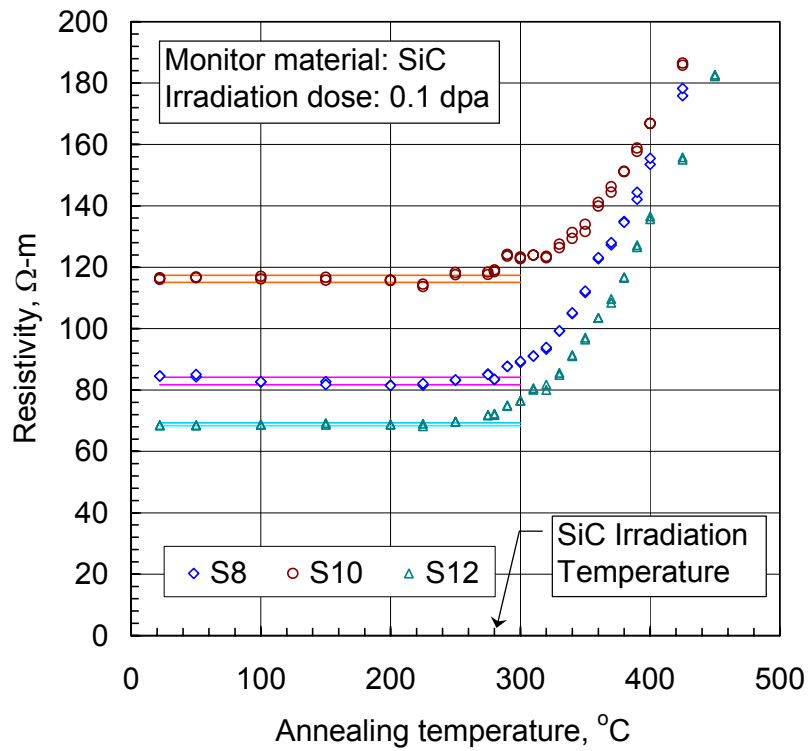
Fig. 38. Resistivity measurements on SiC detectors to determine irradiation temperature.

5.2 Discussion of Phase 3 Findings

Serious enquiries were made into the cause(s) of the low measured radiation hardening. It was established early in the test schedule that the fault was not in the testing system. The drive mechanism, load cell, recording equipment, and furnace temperature on the tensile machine were all shown to be functioning properly. Furthermore, tests made at room temperature to increase the sensitivity of detection of irradiation-induced changes in yield strength, showed no effects of irradiation. Data from the latter tests were consistent with the test data obtained for unirradiated specimens in Phases 1 and 2, reaffirming the reliability of the test system, which was the same system used for testing the Phases 1 and 2 specimens. Despite the lack of extensive radiation damage microstructure, it was clear from other indicators that the specimens did receive the intended irradiation doses. The operational records for the hydraulic facility testified that the rabbits were given the correct exposures in the correct positions. During the exposures the neutron fluxes were normal, as indicated by the facts that isotope production rabbits irradiated in the same rabbit train at the same time as the NERI rabbits yielded the expected quantities of isotopes, and the radioactivity readings on the NERI specimens agreed with the estimated radioactivities. The SiC temperature detectors suffered considerable reductions in resistivity consistent with receipt of a significant radiation dose. So, inadequate radiation dose was not the cause of the low hardening. Therefore, suspicion was diverted to the irradiation temperature, which was deduced to have risen too high for much radiation damage to survive at these low doses.

Investigation of the cause of overheating of the specimens was focused on two suspects; uncertainties in the thermal/hydraulics calculations used to design the internal configuration of the capsule, and unusually low readings of coolant water flow in the hydraulic tube system. The possibility that overheating might have been due to a random temperature spike during irradiation is considered very unlikely because the 0.01 dpa and 0.1 dpa rabbits were irradiated for periods of 4.2h and 42h in sequence in the same Level 7 irradiation position. In order to erase the radiation damage from both rabbits, there would have to be two spikes, both occurring at the ends of the irradiation periods. Another possibility, that there was mispositioning of the specimens and holders in the rabbits, was rejected on the grounds that all the specimens and fixtures were carefully inspected before assembly and were found to be within the specified tolerances, and after assembly the positions of the components in the rabbits was verified by X-ray radiography. During dismantling of the irradiated capsules there were no signs that any of the internal components had shifted their positions. The central, bent specimen, whose function was to act as a spring to keep the tensile specimens pressed against one another, seemed to perform well, and there was no looseness in the stacks.

The computer code HEATING 7 was used for the thermal/hydraulic heat generation and transfer calculations. Independent checks of the methodology and input parameters have revealed no gross sources of errors. It was realized that there were uncertainties in the input values of thermal conductivities for materials undergoing irradiation. Values of gamma heating rates in the HFIR flux trap were also a little uncertain; values of 46 W/g were used for the steels and Zr-4, and 37 W/g for aluminum. It was recognized from the onset that the temperatures at the centers of the specimen stacks would be 60° or so higher than the temperatures at the SiC temperature detectors located on the outsides of the stacks. Although these detectors were not positioned in

the path of the designed heat flow direction, it was expected that their low thermal conductivity would reduce sideways heat flow. Newer models of the capsules now place additional detectors at the centers of the specimen stacks. It was known, too, from literature data described below, that dynamic annealing of the damage microstructure might occur at a temperature, T_{da}, only about 50°C higher than the goal irradiation temperature of T_{irr}= 290°C. To allow for those uncertainties, and to try to ensure that T_{irr} at the centers of the stacks would be below T_{da}, the value of T_{irr} in the calculations was set at 270°C. For such condition, the temperature of the SiC detectors, which were in contact with the aluminum specimen holder and lost heat to it, was estimated to be about 220°C. After irradiation, the temperature measured on the detectors exceeded the estimated temperature by 60°, implying that T_{irr} at the centers of the stacks would also have been 60° higher, at about 330°C. The three dimensional heat transfer calculations have been repeated with closer simulation of the experimental configuration and with added conservatisms. These revised calculations predict that the temperatures of the SiC detectors should be 240-260°C. The predicted temperatures at the centers of the stacks of the tensile are nominally 300°C for the stainless steel and 325°C for Zr-4.

An important factor in the heat transfer calculations is the temperature drop from the rabbit housing to the coolant water flowing over the rabbit. It is estimated to be 15°C at the regular flow rate of 4gpm, which should maintain the housing at about 65°C on average. However, after reactor restart, the two flow meters that monitor the coolant in the Hydraulic Tube facility have intermittently shown abnormally low flow rates of <1gpm. If the flow is reduced from 4gpm to 1gpm, the heat transfer coefficient from the rabbit housing to the coolant would decrease by a factor of 3, raising the housing temperature to 98°C. This would put the operating temperatures of the SiC monitors at about 280°C, and the central tensile specimens at about 340°C. The flow monitoring system uses pressure differential transmitters. HFIR engineers have tentatively attributed the low flow readings to problems in the transmission lines that conduct the signal from the detectors in the hydraulic tube system to the readout panel in the reactor control room, not to actual reduced flow rates. To resolve this issue, new transmitters and electronics were installed during a fuel change in late January 2003. Issuance of the present report was held back to include the results of flow measurements made with the updated system. The new measurements were conducted in late May 2003, and they show that the earlier low flow readings were not real, they were instrument related [71]. These results exonerate the coolant flow from implication in the specimen overheating problem. Therefore, overheating is probably due to leeway in the design and heat transfer calculations for the experiment.

Another way to deduce the irradiation temperature is to compare the experimental observations with relevant published literature data where irradiation temperatures are cited. The fact that some small signs of radiation damage microstructure and radiation hardening were found indicated that the irradiation temperature was at, or just above, the threshold temperature for dynamic annealing of the damage. Prevention or retardation of radiation damage microstructure by dynamic annealing occurs because the damage is thermally unstable. Annealing involves atomic migration, which occurs to some degree at all irradiation temperatures and increases exponentially with temperature. Hence the irradiation temperature is a powerful variable in the retention of stable damage microstructure. The black spot type damage structure observed following low-temperature irradiation consists of clusters of self-interstitial atoms (SIAs) and clusters of vacancies. The thermal equilibrium concentration of vacancies is much greater than

for SIAs, and the binding energy for a vacancy to a vacancy is less than that between SIAs. Hence vacancy clusters are thermally less stable than SIA clusters. With increasing irradiation temperature greater rates of evaporation of vacancies from the vacancy clusters cause their elimination. Since some of the mobile vacancies become absorbed by the SIA clusters, where reaction between a vacancy and an SIA eliminates both defects, a gradual removal of the SIA clusters also occurs. Thus, the behavior of the vacancies governs the annealing response of the damage microstructure at intermediate temperatures. For a given point defect production rate, or neutron flux, a critical irradiation temperature, T_{da}, can be defined above which dynamic annealing ensures that few radiation-induced point defects survive and little or no damage structure will develop, although some radiation-assisted thermal aging products may occur. Transmutation products are retained but they will have little or no effects on radiation hardening in the present experiments.

Values of T_{da} will depend on material composition and structure, displacement rate, and other factors, and are neither well investigated nor well defined for commercial alloys. Boundary values can be obtained from postirradiation annealing (PIA) studies. Two key factors in the annealing of damage structure are the mobility of vacancies and the binding energy of vacancies to clusters. The temperature where vacancy mobility becomes appreciable, also known as the Stage III annealing temperature in PIA studies, usually occurs at homologous temperatures greater than about $0.25T_m$ All three alloys herein have melting temperatures around $1500^{o}C$, for which $0.25T_m$ is about $170^{o}C$. So the targeted irradiation temperature of $288^{o}C$ for the Phase 3 experiments was above the lower temperature boundary for T_{da}. A rough guide to the upper boundary of T_{da} is the temperature at which the point defect clusters disappear or mechanical properties are recovered during PIA, corresponding to Stage V recovery, which is believed to be dominated by thermal debonding of vacancies from clusters. The Stage V temperature is higher than T_{da} because the vacancy binding energy varies with cluster size and the damage structures in PIA studies are usually more mature than the more embryonic clusters involved in dynamic annealing. Literature data indicate that the effective Stage V temperature for bcc ferritic steels is $300-400^{o}C$ [72], and is $350-400^{o}C$ for Zircaloy [73,74]. For austenitic stainless steels the picture is not so clear. Measurements of recovery of electrical resistivity of pure Fe-Cr-Ni austenitic alloys during PIA after irradiation to about 0.0001 dpa at cryogenic temperature indicate an effective Stage V at $190-427^{o}C$ [75,76]. In tensile tests conducted on austenitic steels after irradiation to doses of about 0.007 dpa at $45^{o}C$ [77] and 0.01 dpa at $300^{o}C$ [54], radiation-induced increases in yield strength disappeared at $500^{o}C$ and $600^{o}C$, respectively.

Closer values of T_{da} can be derived from the highest irradiation temperatures for which residual point defect cluster-type damage has been observed, or the lowest irradiation temperature at which radiation hardening is reportedly absent in alloys similar to those employed here, and at similar irradiation doses. The reason for choosing similar doses is that, contrary to intuition, T_{da} will increase with dose. This dose dependence arises because a small fraction of point defect clusters ripen, or grow, during dynamic annealing and require higher temperatures to remove them. Another contributor to this dose dependence is the accumulation of transmutation products that stabilize point defect clusters. In particular, helium is known to promote formation of black spot damage [78] and delay the annealing of damage structure [79]. In ferritic steels, damage microstructure is not easily visible so T_{da} must be determined from disappearance of radiation-induced increases in yield strengths and Charpy impact transition temperatures. These increases

are less at T_{irr}=290°C than for room temperature irradiations, and are minor at T_{irr}>350°C for doses up to about 0.03 dpa [80-85]. Reviews [86,87] of radiation damage microstructures in zirconium and its alloys agree that neutron damage microstructure is coarse or absent at T_{irr}>500°C. Reductions in the radiation-induced increases in yield strengths of Zircaloy-2 irradiated to doses of 0.04-1.0 dpa are sensed at about T_{irr} =300°C and decline to zero at T_{irr} =350°-475°C [88]. In austenitic stainless steel, the dose dependence of T_{da} is evident from changes in tensile properties [55,89-91]. At doses of 3-10 dpa [55], T_{da} is >400°C; at a dose of about 1 dpa [90,91], T_{da} =325-420°C; at about 0.5 dpa, T_{da} = 300-400°C [55], and at a dose of about 0.002 dpa it is between 300° and 380°C [89]. Summaries of defect cluster densities in austenitic stainless steel as a function of neutron irradiation temperature after doses of 0.04 – 0.16 dpa [92] and 0.1-5 dpa [93] show a factor of two or so decline in densities between 60° and 200°C, a further decade reduction between 200 ^{o}C and 300°C, and almost another decade fall between 350° and 400°C . The defect structure changes from a black spot dominated region to a cavity dominated region at about 300°C [93]. At 400°C the dislocation loops are coarse [92] and are unlikely to substantially increase the flow stress. Thus, for austenitic stainless steel irradiated to doses of 0.01-0.1 dpa pertinent to the Phase 3 experiments, T_{da} can be expected in the range 300-380°C.

It seems, then, that T_{da}, the critical irradiation temperature above which there is insufficient retention of radiation damage microstructure to affect mechanical properties after doses of 0.01 to 0.1dpa, relevant to the present work, is about 330-350°C for bcc ferritic alloys, stainless steel, and Zircaloy. In the Phase 3 work, there was no radiation hardening in the ferritic steel and the austenitic steel, and only a small amount of radiation damage microstructure and hardening in the Zr-4. Therefore, judging from the derived literature values of T_{da}, the Phase 3 observations are consistent with an irradiation temperature of about 350°C.

Despite the low level of irradiation hardening obtained in the Phase 3 specimens, some positive conclusions regarding the temperature dependence of neutron irradiation damage and the strain rate dependence of tensile properties of A533B, Zircaloy-4, and 316 stainless steel can be drawn. The importance of dynamic annealing of displacement damage microstructure is emphasized. Analysis of the Phase 3 results and the data survey conducted herein identify a T_{da} of about 330-350°C for all three materials at doses of about 0.01-0.1 dpa. This conclusion consolidates our knowledge of the role of temperature in the viability of radiation damage, and provides valuable guidance for planning future irradiation experiments in these materials.

The strain rate data displayed in Figs. 33-35 show no effects of irradiation but they reveal some interesting features. The A533B steel, being a bcc ferritic alloy, is reputedly strongly sensitive to strain rate. It showed very little increase in yield strength with increasing strain rate in the present tests, Fig. 33, and its UTS had a negative strain rate sensitivity. The fcc 316 stainless steel, which is usually regarded as being relatively insensitive to strain rate, displayed small increases in yield strength and UTS with increasing strain rate, with corresponding small decreases in elongation values, Fig. 34. In the hcp Zr-4 alloy, Fig. 35, increased strain rate substantially raised the yield and ultimate tensile strengths and caused associated reductions in elongation values. For comparison purposes, and because there are no strain rate effects data for dislocation channeling, some spare specimens from the Phase 1 and 2 irradiations made at 60-

100°C were tested at various strain rates at room temperature. No 316 stainless steel specimens were available, but it has been reported elsewhere that increasing the strain rate in room temperature tests of 304L stainless steel did not change the yield strength of the unirradiated steel [92] whereas in one case [92] it raised the yield strength of the irradiated steel, and in another case [88] it had no effects. The present results for A533B steel and Zr-4 are given in Figs. 39 and 40.
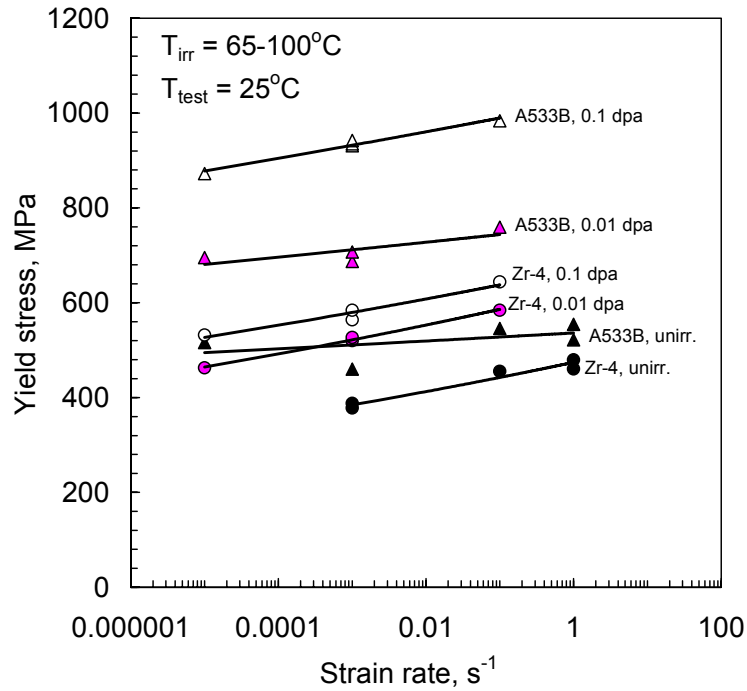
Fig. 39. Strain rate dependence of the yield strengths of A533B steel and Zircaloy-4 irradiated at 65-100°C and tested at room temperature.
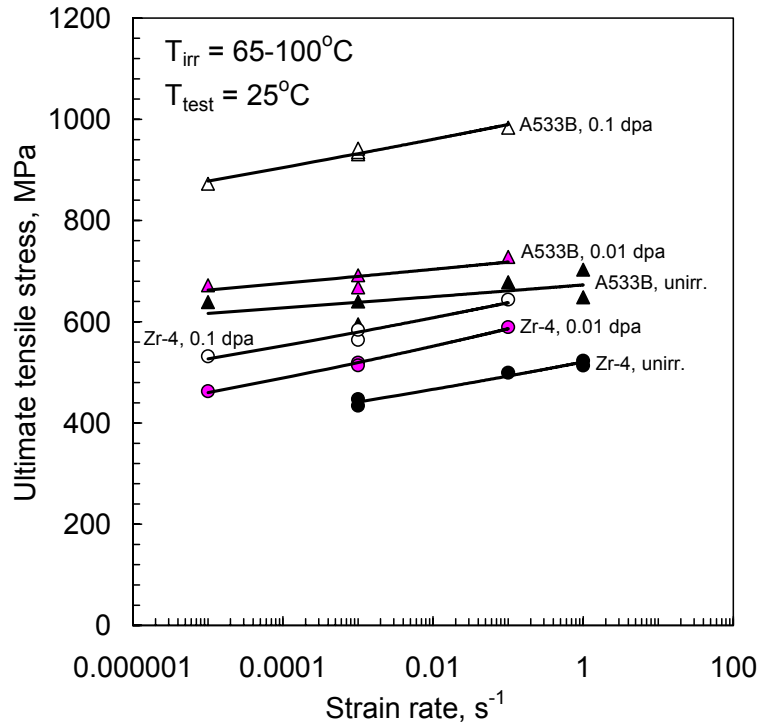
Fig. 40. Strain rate dependence of the ultimate tensile strengths of A533B steel and Zircaloy-4 irradiated at 65-100°C and tested at room temperature.

It is evident that the yield strengths for the unirradiated A533B steel display small increases with strain rate over the range investigated, which is the same response as the tests at 288°C, Fig.33. The irradiated A533B specimens show larger increases in yield strength with strain rate and with irradiation dose compared to the tests at 288°C. The UTS values for the A533B steel display a positive sensitivity to strain rate in room temperature tests, in contrast to a negative sensitivity in the 288°C tests. This difference may be influenced by dynamic strain aging at 288°C. The yield strength of unirradiated Zr-4 increases with strain rate at room temperature, but irradiation does not alter the strain rate dependence. The strain rate sensitivity of Zr-4 is much less in the room temperature tests than in the 288°C tests. At room temperature, the increase in yield strength is about 20% over the strain rate range 0.001-1.0 s^{-1}, compared to about 100% increase at 288°C. It is noted, too, that Zr-4 is about 50% weaker at 288°C than at room temperature, whereas the strengths of the two steels are relatively unaffected by the temperature change.

It is concluded that for the range of strain rates investigated here, the effects on tensile properties are small and are only slightly heightened by irradiation. Of the three alloys, Zircaloy-4 is the most sensitive to strain rate and is more sensitive at 288°C than at room temperature.

59

6.0 Suggestions for future work

- First and foremost, the attempted 288°C irradiations should be repeated under good conditions of temperature control. This temperature region remains of critical interest for strain localization studies. Additionally, studies of damage accumulation mechanisms and effects of test temperature on mechanical properties in the temperature range ~250-350°C are needed. The available 1 dpa specimens that were not used in the present work could be tested to verify the dose dependence of the dynamic annealing temperature.

- Theory and modeling of strain localization should be integrated into practical deformation studies, both at the atomic level (molecular dynamics) and the macroscopic level (deformation mechanics).

- Dislocation channeling has been observed elsewhere to occur in the preyield microstrain regions in Mo, V, and Zircaloy-2. The possibility that channeling may be the precursor to gross necking instability should be investigated.

- The role of strain localization in formation of intergranular cracks and transgranular cleavage cracks should be explored.

- TEM studies are essential for this type of research and are necessary for a clearer understanding of radiation damage in materials in general. Obtaining satisfactory TEM specimens from local regions of the miniature tensile specimens proved to be quite a challenge and was a limiting factor in the present research. To facilitate TEM, and to ensure that usable specimens can be obtained consistently from small regions of small mechanical test specimens, an improved TEM specimen preparation technique is needed. A technique that offers ideal conditions for thinning small radioactive TEM pieces is focused ion beam (FIB) technology. State-of-the-art, programmable, remotely operable FIB machines are used routinely in the semiconductor industry for quality control and problem shooting in CMOS production lines. FIB machines are expensive, $1M+, and require a trained operator. It is suggested that DOE seriously consider setting up a dedicated FIB user center at ORNL to provide TEM specimens from radioactive materials for all DOE laboratories and subcontractors. Such a facility for radiaoactive specimens currently exists only in Japan at JAERI.

7.0 Acknowledgements

8.0 References

1)   F. A. Smidt, Jr., NRL Report 7078, Naval Research Laboratory, Washington D.C. (1970).

2)   M. S. Wechsler, Chapter 2 in *The Inhomogeneity of Plastic Deformation*, pub. Amer. Soc. for Metals (1971) 19-54.

3)   A. Luft, *Progr. in Mater. Sci.* 35 (1991) 97-204.

4)   J. V. Sharp, *Phil. Mag.* 16 (1967) 77-96.

5)   R. P. Tucker, M. S. Wechsler, and S. M. Ohr, J. Appl. Phys. 40-No. 1 (1969) 400-408.

6)   T. H. Blewitt, R. R. Coltman, R. E. Jamison and J. K. Redman, *J. Nucl. Mater.* 2 (1960) 277-298.

7)   H. J. Frost and M. F. Ashby, *Deformation-Mechanism Maps*, Pergamon Press, 1982.

8)   M. F. Ashby, *Materials Selection in Mechanical Design*, Pergamon Press, 1992.

9)   A. Okada, K. Kanao, T. Yoshiie, and S. Kojima, Mater. Trans. JIM 30 No. 4 (1989) 265-272.

10)   K. Farrell, T. S. Byun, J. W. Jones. L. T. Gibson, R. G. Sitterson, N. Hashimoto, J. L. Bailey, and M. J. Gardner, " Small Specimen Procedures for Determination of Deformation Maps", in *Small Specimen Test Techniques: Fourth Volume*, ASTM STP 1418, Amer. Soc. for Testing and Materials (2002) 283-293.

11)   T. S. Byun, E. H. Lee, J. D. Hunn, K, Farrell, and L. K. Mansur, J. Nucl. Mater. 294 (2001) 256-266.

12)   S. T. Mahmood, S. Mirzadeh, K. Farrell, J. V. Pace III, and B. M. Oliver, "Neutron Dosimetry of the HFIR Hydraulic Facility", ORNL/TM-12831, Oak Ridge National Laboratory report, February 1995.

13)   T. A. Gabriel, B. L. Bishop, and F. W. Wiffen, "Calculated Irradiation Response of Materials Using Fission Reactor (HFIR, ORR, and EBR-II) Neutron Spectra", ORNL/TM-6361, Oak Ridge National Laboratory report, August 1979.

14)   K. Farrell, T. S. Byun, and N. Hashimoto, "Mapping Flow Localization Processes in Deformation of Irradiated Reactor Structural Alloys", ORNL/TM-2002/66, Oak Ridge National Laboratory report, July 2002.

15)   H. R. Higgy and F. H. Hammad, J. Nucl. Mater. 55 (1975) 177-186.

16)   E. H. Lee, T. S. Byun, J. D. Hunn, K. Farrell, and L. K. Mansur, J. Nucl. Mater. 296 (2001) 183-191.

17)   E. H. Lee, T. S. Byun, J. D. Hunn, M. H. Yoo, K. Farrell, and L. K. Mansur, Acta Mater. 49 (2001) 3269-3276.

18) E. H. Lee, T. S. Byun, J. D. Hunn, M. H. Yoo, K. Farrell, and L. K. Mansur, Acta Mater. 49 (2001) 3277-3287.

19) A. H. Cottrell and R. J. Stokes, Proc. Roy. Soc. A233 (1955) 17-33.

20) Ch. Ritschel, A. Luft, and D. Schulze, Kristall und Technik 13 (1978) 791-797.

21) S. Yoshida, M. Kiritani, Y. Deguchi, and N. Kamigaki, Suppl. to Trans. JIM 9 (1968) 83-89.

22) T. Mori and M. Meshii Acta Met. 17 (1969) 167-175.

23) A. Gysler, G. Lütjering, and V. Gerold, Acta Met. 22 (1974) 901-909.

24) T. H. Sanders Jr. and E. A. Starke Jr., Acta Met. 30 (1982) 927-939.

25) I. G. Greenfield and H. G. F. Wilsdorf, J. Appl. Phys. 32 No.5 (1961) 827-839.

26) U. Essmann and A. Seeger, phys. stat. sol. 4 (1964) 177-197.

27) J. L. Brimhall, Trans. Met. Soc. AIME 233 (1965) 1737-1742.

28) A. H. Cottrell, in *Bristol Conference on Strength of Solids*, Phys. Soc. 30, London (1948).

29) G. T. Hahn, Acta Met. 10 (1962) 727-738.

30) R. J. Price and A. Kelly, Acta Met. 12 (1964) 159-169.

31) P. J. Jackson and P. D. K. Nathanson, South African J. of Phys. 1 (1978) 7-21.

32) M. J. Makin and J. V. Sharp, Phys. Stat. Sol. 9 (1965) 109-118.

33) H. Neuhäuser and R. Rodloff, Acta Met. 22 (1974) 375-384.

34) B. L. Eyre and A. F. Bartlett, Phil. Mag. 12 (1965) 261-272.

35) J. S. Bryner, Acta Met. 14 (1966) 323-336.

36) I. M. Robertson, M. L. Jenkins, and C. A. English, J. Nucl. Mater. 108 & 109 (1982) 209-221.

37) F. Frisius, R. Kampmann, P. A. Beaven, and R. Wagner, in *Proc. BNES Conf. on Dimensional stability and mechanical behaviour of irradiated metals and alloys*, Brighton (1983) 171-174.

38) O. Okada, T. Yasujima, T. Yoshiie, I. Ishida, and M. Kiritani, J. Nucl. Mater. 179-181 (1991) 1083-1087.

39)   H. Mughrabi, D. Strohle, and M. Wilkens, Zeit. fur Metallkunde 72-5 (1981) 300-309.

40)   H. L. Heinisch, J. Nucl. Mater. 155-157 (1988) 121-129.

41)   T. S. Byun, Acta Materialia 51 (2003) 3063-3071.

42)   B. A. Cheadle, C. E. Ells, and J. van der Kuur, in *Zirconium in Nuclear Applications,* ASTM STP 551, Amer. Soc. for Testing and Mater. (1974) 370-384.

43)   A. K. Seeger, *Proceedings of the Second International Conference on the Peaceful Uses of Atomic Energy*, P/989, 6 (1958) 250-273.

44)   S. J. Zinkle, J. Nucl. Mater. 150 (1987) 140-158.

45)   B. N. Singh and S. J Zinkle, J. Nucl. Mater. 206 (1993) 212-229.

46)   M. Eldrup, B. N. Singh, S. J. Zinkle, T. S. Byun, and K. Farrell, J. Nucl. Mater. 307-311 (2002) 912-917.

47)   J. R. Beeler, p. 84-104 in *Flow and Fracture Behavior of Metals and Alloys in Nuclear Environments*, ASTM STP 380, Amer. Soc. for Testing and Mater., 1964.

48)   F. Gao, D. J. Bacon, A. F. Calder, P. E. J. Flewitt, and T. A. Lewis, J. Nucl. Mater. 230 (1996) 47-56.

49)   Naoaki Yoshida, J. Nucl. Mater. 174 (1990) 220-228.

50)   K. Farrell and T. S. Byun, J. Nucl. Mater. 318 (2003) 274-282.

51)   N. Yoshida, H. L. Heinisch, T. Muroga, K. Araki, and M. Kiritani, J. Nucl. Mater. 179-181 (1991) 1078-1082.

52)   G. R. Odette and G.E. Lucas, J. Nucl. Mater. 191-194 (1992) 50-57.

53)   G. E. Lucas, J. Nucl. Mater. 206 (1993) 287-305.

54)   Fujio Abe, Minoru Narui, and Hideo Kayano, Mater. Trans., Japan Inst. Metals 33 (1992) 1123-1129.

55)   Marc G. Horsten and Martin I. de Vries, in *Effects of Radiation on Materials: 17th International Symposium*, ASTM STP 1270, Amer. Soc. for Testing and Mater. (1995) 919-932.

56)   J. E. Pawel, A.F. Rowcliffe, D.J. Alexander, M.L. Grossbeck, and K. Shiba, J. Nucl. Mater. 233-237 (1996) 202-206.

57)   J. E. Pawel, A. F. Rowcliffe, G. E. Lucas, and S. J. Zinkle, J. Nucl. Mater. 239 (1996) 126-131.

58)   N. Hashimoto, S. J. Zinkle, A. F. Rowcliffe, J. P. Robertson, and S. Jitsukawa, J. Nucl. Mater. 283-287 (2001) 528-534.

59)   M. Victoria, N. Baluc, C. Bailat, Y. Dai, M. I. Luppo, R. Schaublin, and B. N. Singh, J. Nucl. Mater. 276 (2000) 114-122.

60)   C. Baillat, A. Almazouzi, N. Baluc, R. Schaublin, F. Groschel, and M. Victoria, J. Nucl. Mater. 283-287 (2000) 446-450.

61)   Masayoshi Suzuki, A. Sato, T. Mori, J. Nagakawa, N. Yamamoto, and H. Shiraishi, Phil. Mag. A 65 (1992) 1309-1326.

62)   S. M. Bruemmer, J. I. Cole, J. L. Brimhall, R. D. Carter, and G. Was, in *Sixth Internat. Symp. on Environmental Degradation of Materials in Nuclear Power Systems-Water Reactors*, The Metals and Minerals Society (1993) 537-546.

63)   James I. Cole and Stephen M. Bruemmer, J. Nucl. Mater. 225 (1995) 53-58.

64)   J. L. Brimhall, J. I. Cole, J. S. Vetrano, and S. M. Bruemmer, Mat. Res. Soc. Symp. Proc. 373, Materials Research Society (1995) 177-182.

65)   A. L. Bement, J. C. Tobin, and R. G. Hoagland, in *Flow and Fracture of Metals and Alloys in Nuclear Environments,* ASTM STP 380, Am. Soc. Testing Mater. (1964) 364-385.

66)   C. E. Ells and C. D. Williams, Suppl. to Trans. Japan Inst. Metals 9 (1968) 214-219.

67)   C. E. Coleman, D. Mills, and J. van der Kuur, Canadian Metallurgical Quarterly 11-1(1972) 91-100.

68)   R. B. Adamson, S. B. Wisner, R. P. Tucker, and R. A. Rand, in *The Use of Small Scale Specimens for Testing Irradiated Material*, ASTM STP 888, Am. Soc. Testing Mater. (1986) 171-185.

69)   H. L. Heinisch, J. Nucl. Mater. 155-157 (1988) 121-129.

70)   L. L. Snead, A. M. Williams, and A. L. Qualls, "Revisiting the use of SiC as a Post Irradiation Temperature Monitor", in *Effects of Radiation on Materials*, ASTM STP 1447, Amer. Soc. for Testing and Mater. (2003), in press.

71)   Letter from G. J. Hirtz to M. B. Farrar, "Evaluation of Administration Restriction placed on the HFIR Hydraulic Rabbit Facility on September 10, 2002.", May 29, 2003, Oak Ridge National Laboratory.

72)   E. A. Little, International Metals Reviews, 204 (1976) 25-60.

73)   L. M. Howe, "The Annealing of Irradiation Damage in Zircaloy-2 and the Effect of High Temperature Irradiation on the Tensile Properties of Zircaloy-2", A.E.C.L. 1024, Atomic Energy of Canada Limited (1960).

74)   T. Onchi, H. Kayano, and Y. Higashiguchi,, J. Nucl. Mater. 88 (1980) 226-235.

75)   C. Dimitrov, M. Tenti, and O. Dimitrov, J. Phys. F:Metal Phys. 11 (1981) 753-765.

76)   C. Dimitrov and O. Dimitrov, J. Nucl. Mater. 105 (1982) 39-47.

77)   P. C. L. Pfeil and D. R. Harries, in *Flow and Fracture of Metals and Alloys in Nuclear Environments*, ASTM STP 380, Amer. Soc. for Testing and Mater. (1964) 202-221.

78)   K. Farrell, Radiation Effects, 53 (1980) 175-194.

79)   R. E. Stoller, "Microstructural Evolution in Fast-Neutron-Irradiated Austenitic Stainless Steels", ORNL-6430, Oak Ridge National Laboratory (1987).

80)   D. R. Harries, R. W. Nichols, and C. Judge, *Steels for Pressure Reactor Circuits*, Special Report No. 69, The Iron and Steel Institute, London (1961) 297-327.

81)   J. R. Hawthorne, *Steels for Pressure Reactor Circuits*, Special Report No. 69, The Iron and Steel Institute, London (1961) 343-369.

82)   R. W. Nichols and D. R. Harries, *Radiation Effects on Metals and Neutron Dosimetry,* ASTM STP 341, Amer. Soc. for Testing and Mater. (1963) 162-199.

83)   R. G. Berggren, W. J. Stelzman, and T. N. Jones, "Radiation Effects on Pressure Vessel Steels", Solid state Division Progress Report for Period Ending January 1967, ORNL-4097, Oak Ridge National Laboratory (1966).

84)   E. A. Little and D. R. Harries, *Irradiation Effects in Structural Alloys for Thermal and Fast Reactors*, ASTM STP 457, Amer. Soc. for Testing and Mater. (1969) 215-241.

85)   V. M. Stefanovic and N. Lj. Milasin, *Irradiation Effects on Structural Alloys for Nuclear Reactor Applications,* ASTM STP 484, Amer. Soc. for Testing and Mater. (1970) 521-536.

86)   D.O. Northwood, Atomic Energy Review 154 (1977) 547-609.

87)   M. Griffiths, J. Nucl. Mater.159 (1988) 190-218.

88) C. E. Ells, C. E. Coleman, and C. D. Williams, "The Temperature Dependence of Irradiation Damage in Zirconium Alloys", A.E.C.L. 5470, Atomic Energy of Canada Limited (1974); and in *Strength of Materials Symposium*, Kyoto, August 1974.

89) N. F. Pravdyuk, S. T. Konobeevsky, A. D. Ameyev, and Y. I. Pokrovsky, P/2052 in Proc. 2nd United Nations International Conference on the Peaceful Uses of Atomic Energy-Vol. 5 (1958) 457-465.

90) W. R. Martin and J. R. Weir, in *Flow and Fracture of Metals and Alloys in Nuclear Environments*, ASTM STP 380, Amer. Soc. for Testing and Mater. (1964) 251-268.

91) E. E. Bloom, W. R. Martin, J. O. Stiegler, and J. R. Weir, J. Nucl. Mater. 22 (1967) 68-76.

92) N. Yoshida, Q. Xu, H. Watanabi, T. Muroga, and M. Kiritani, J. Nucl. Mater. 191-194 (1992) 1115-118.

93) A. F. Rowcliffe, S. J. Zinkle, J. F. Stubbins, D. J. Edwards, and D. J. Alexander, J. Nucl. Mater.258-263 (1998) 183-192.

94) J. C. Wilson and R. G. Berggren, ASTM Proceedings 55 (1955) 689-707.

Appendix A: Details of Experiment conditions.

A1. Sources and chemical compositions of the three alloys, and heat treatments for the tensile specimens.

All tensile test specimens were electrodischarge-machined from cold rolled, 0.25 mm thick sheets of the alloys. The edges of the gauge sections were sanded by hand to eliminate machining irregularities. Identity marks were engraved on the heads. After a light surface sanding to remove engraving burrs, the specimens were ultrasonically cleaned in alcohol and acetone, and were then subjected to the appropriate heat treatments.

A533B Ferritic Steel
Source: R. K. Nanstad, Metals and Ceramics Division, ORNL. This material is from the 02 plate in the HSST program described by C. E. Childress on p. 49 in "Fabrication History of the First Two 12-in.-Thick ASTM A-533 Grade B, Class 1 Steel Plates of the Heavy Section Steel Technology Program, Documentary Report 1", ORNL-4313, UC-80- Reactor Technology, February, 1969. This particular steel is an acknowledged reference material for studies of radiation effects in pressure vessel steels.

Table A1.1. The chemical composition of A533B steel (wt.%)

C	Si	Mn	S	P	Ni	Mo	Fe
.22	.25	1.48	.018	.012	.68	.52	Bal.

Treatment: Vacuum-seal in a quartz capsule. Anneal 4h @ 880°C, air-cool to room temperature; reheat for 4h @ 660°C, air-cool to room temperature; reheat 20h @ 610°C, furnace-cool to 315°C, then air-cool to room temperature. This treatment produces a microstructure of lath-like tempered bainite in which the mean packet size of granular bainite structure was measured at 9μm, Fig. A1.1.
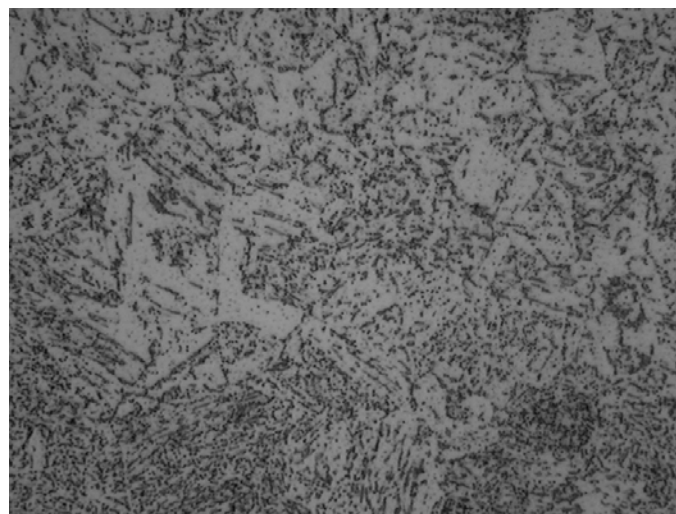
Fig. A1.1. Microstructure of A533B steel.

Zircaloy-4 (Zr-4)
Source: D. Hobson, Metals and Ceramics Division, ORNL. Chemical analysis provided by ABB
C-E Services Inc, letter of March 7, 2000 to K. Farrell.

Table A1.2. The chemical composition of Zircaloy- 4 (wt.%)

C	Sn	Fe	Ni	S	N	O	Zr
.015	1.4	0.1	<0.1	0.001	<0.001	0.06	Bal.

Treatment: Anneal 30 min. @ 670°C in vacuum. The microstructure was recrystallized equiaxed
grains of mean size 13 μm, Fig. A1.2.
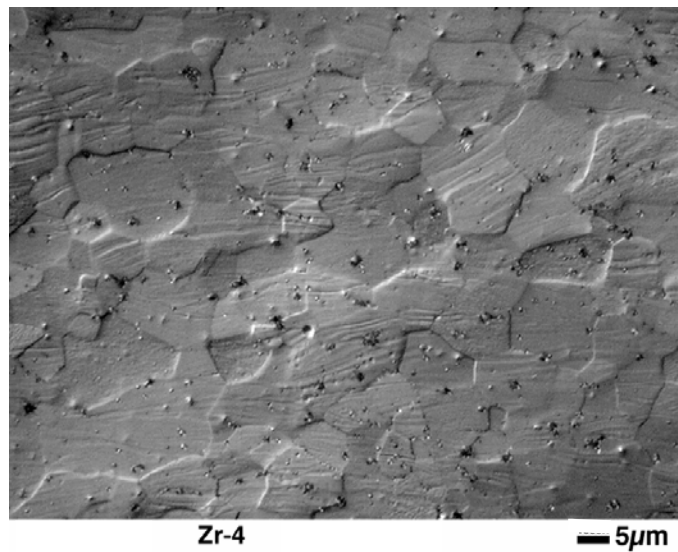
Fig. A1.2. Microstructure of annealed Zircaloy-4.

Ref 316 Austenitic Steel.
Source: L. T. Gibson, Metals and Ceramics Division, ORNL. This material is the reference heat # 8092297C described in Table 4.3 in "Mechanical Properties Design Data Program Semiannual Progress Report for Period Ending January 31, 1984", ORNL/MSP/1.3-84/1, May, 1984.

Table A1.3. The chemical composition of 316 stainless steel (wt.%)

C	Mn	Si	S	P	Cr	Ni	Mo	Ti	Nb+Ta	Cu	Co	N	B	Fe
.059	1.86	.57	.018	.024	17.15	13.45	2.34	<.01	<.01	.10	.02	.031	0.0005	Bal.

Treatment: Anneal 30 min. @ 1050°C in vacuum. The microstructure, Fig. A1.3, was recrystallized equiaxed grains of mean size 67 μm.
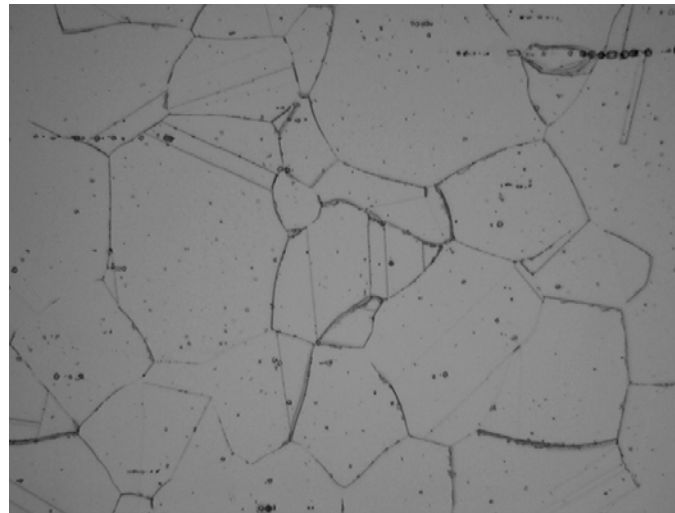
01-2844-02   Ref. 316(T120)   0.011"Thick   500X 10μm
Anstenitic   Aqua Regia

Fig. A1.3. Microstructure of annealed 316 stainless steel.

A2. Specimen size and handling

Experiments of the type and scope needed to obtain deformation mode maps for irradiated materials entail testing and handling of many radioactive specimens, sometimes outside the hot cell where radiation exposure to research personnel can be high. To minimize radioactivity levels and to make the maximum use of available space in the irradiation facility, a custom-designed miniature tensile specimen was used. The specimen was made thin enough, 0.25 mm, for excision of TEM pieces that required no further reduction in thickness by grinding, thereby eliminating the grinding operation and the associated radioactive dust. The 0.25 mm thickness did not compromise the strength properties of the materials. Comparison of the tensile properties of our miniature specimens with those of larger specimens showed very good reproduction of strength properties but reduced elongation values due to the size effect. Duplication of property values in multiple tests was excellent. Yield point drops and Lüders strains were reproduced. However, because it is small and thin, the specimen is sensitive to possible introduction of extraneous plastic strains from inappropriate loading techniques. In particular, loading through pins or by friction gripping was considered likely to be unsuitable. Trials with pin-loaded specimens showed much plastic extension at the holes, despite the pin diameter (1.8 mm) being larger than the gauge width (1.5 mm). Therefore, an under-the-shoulder loading system was devised. The heads of the specimens were made broad so that the load-bearing area of the shoulders was at least three times larger than the gauge cross section. A bonus of the large heads is that they allow 3 mm disks to be punched or otherwise cut from them. Such disks are suitable for deformation studies in a disk bend apparatus [11].

The load is applied to the tensile specimen in the custom-built cradle pictured in Fig. A2.1. The cradle protects the small specimen against accidental bending or torsion moments that might occur during manual positioning of the specimen in the tensile machine. It aligns the specimen, applies the load under its shoulders during the test, and requires only easy movements to release the tested specimen. No clamping is required. The tensile specimen is placed in the cradle simply by lowering the specimen into the open recesses in the cradle head pieces while the cradle is lying on a workbench. The cradle is constructed from cold worked stainless steel. Its two headpieces move on a track made from two rod rails. The rails pass through clearance holes drilled in the headpieces of the cradle. Extension arms screwed into the head pieces have end knobs with convex shoulders that are radiused to mate with concave seats in thimble pieces attached to the pull rods of the tensile machine. This ball-and-socket type arrangement ensures good axial alignment during loading. The load is transmitted to the specimen via the inner faces of the slotted portions of the recessed cavities in the cradle headpieces. Those faces are shaped to match the shoulder contours of the tensile specimen. Sliding gates are installed in the cradle headpieces at right angles to the tensile axis and they straddle the specimen heads. The gates assure that the specimen remains properly seated during lifting of the cradle and insertion in the tensile machine, and they retain the pieces of a specimen broken in test. They were also intended to deter any tendency for plastic buckling of the heads during the test. However, tests to failure with trial specimens, and subsequently with many irradiated specimens, have shown that the gates may not be needed for that purpose; no distortion of specimen heads has been found, not even in tests made with the gates open.
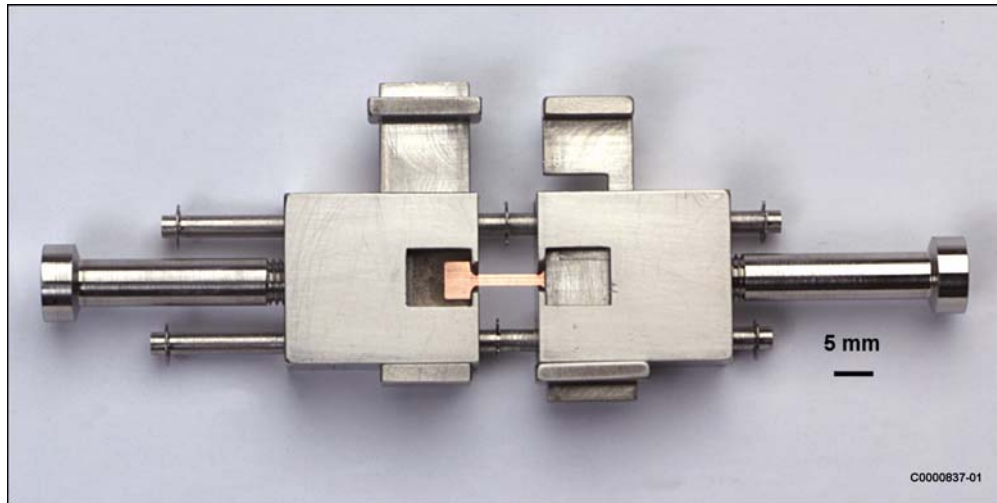
Fig. A2.1. The tensile cradle.

To prepare a specimen for testing, the cradle is laid on its back on a bench with the gates open and the headpieces touching one another. The specimen is picked up with tweezers or vacuum tweezers and is positioned into the channel and the head cavities. Seating of the specimen is checked though a mirror and the heads are separated with tongs until resistance is felt. Using tongs, the gates are closed and the cradle is lifted by one of its extension arms and is placed in the machine pull rod thimbles

All tensile tests were conducted at room temperature in a screw-driven machine at a crosshead speed of 0.008 mm.s^{-1}, corresponding to a specimen strain rate of 10^{-3}s^{-1}. Engineering strain was calculated from the recorded crosshead separation, using a nominal gauge length of 8 mm. Engineering stress was calculated as the load divided by the initial cross section area before irradiation. The load cell was calibrated to NIST-approved standards.

A3. Neutron Irradiation Conditions

A3.1 Radiation Site and Specimen holders

Irradiations of the specimens were not described in Ref. 10, so details are given here. The irradiations were carried out in flowing coolant water in the Hydraulic Tube facility of the High Flux Isotope Reactor. The Hydraulic Tube passes into the flux trap region at the center of the cylindrical fuel element. The high-pressure water passing through the tube conducts a train of nine, cylindrical, aluminum capsules, called rabbits, in and out of the flux trap without disrupting the operation of the reactor. Neutron fluxes at the rabbits are of order 4 x 10^{18} n.m^{-2}.s^{-1}, E >1 MeV, and 2 x 10^{19} n.m^{-2}.s^{-1}, thermal neutrons. The nuclear heating rate in the facility is high, and cooling of the specimens is necessary to maintain a constant, low temperature. There is no instrumentation in the facility to measure the temperature of specimens inside a rabbit so the best way to obtain a low temperature is to ensure that the specimens are in contact with the flowing coolant. In which case, the temperature of the specimens is estimated to be in the range 65-100°C. For the Phase 1 and 2 irradiations, the rabbit was custom-designed with numerous perforations through the walls and end plugs to permit the water to flow directly over the

specimens. The A533B steel and Zr-4 materials are prone to oxidation and absorption of hydrogen when exposed to a water environment, and if such events occurred during irradiation they could affect mechanical properties and confound a simple discrimination of the effects of irradiation. Therefore, to screen the specimens from oxidation and at the same time keep them in good thermal contact with the water to allow removal of nuclear heat, the A533B steel and Zr-4 specimens were sealed in soft aluminum envelopes. The envelopes were made from annealed, high purity aluminum foil, 0.125 mm thick. Each envelope contained two tensile specimens, one laid directly on top of the other. Closure of the envelopes was made by electron beam welding in vacuum. On removal from the vacuum chamber, the atmospheric pressure, aided by a little finger pressure, forced the soft foil against the specimens. During irradiation, the high water pressure of 3.2 MPa in the hydraulic tube ensured that good thermal contact was maintained between the envelope and the specimens.

For the Phase 3 irradiations at $290^{o}C$, the specimens were irradiated in the HFIR Hydraulic Tube facility, this time in a non-perforated, regular, finned rabbit in the arrangement shown in Fig. A3.1. Three stacks of specimens, one for each alloy, were secured in aluminum holders. The holders were rectangular in cross section, with their short sides curved to match the inside curvature of the rabbit wall. The specimen stacks were placed in a centrally-spaced rectangular cutout in the holder. Each stack, reading from outside to center, consisted of a silicon carbide temperature monitor, the same length and width as a tensile specimen blank, and 0.375 mm thick; a TEM blank, same length and width as the monitor and 0.25 mm thick, with four 3 mm diameter TEM disks wire-machined into it and left attached with small uncut sections; and six tensile specimens, 0.25 mm thick. At the center of the stack was a reject tensile specimen bent into an S-shape to act as a spring that compressed the stack and held it against the walls of the holder. The other half of the stack was a mirror image of the first half. The stack was oriented in the holder such that the planes of the specimens were parallel to the long, flat sides of the holder. Aluminum filler pieces shaped to fill the gauge section cut-outs in the tensile specimens were placed on both sides of the specimen stacks to provide good thermal conduction in the plane of the specimens towards the curved sides of the holders. This aluminum conduction path was the designed direction of major heat transfer from the specimens to the holder thence to the rabbit wall. The three loaded holders were keyed together in a train and were slid into the rabbit whose solid end plug was already welded in. The train was carefully positioned so as to leave a small, annular gap of 0.0035-in. between the curved sided of the holders and the inside of the rabbit, using small standoff points on the holders. When the train position was satisfactory, the end plug containing the gas fill hole was welded in place. The rabbit was then place in a vacuum chamber and evacuated and backfilled with helium. The filler hole was sealed by laser welding it through a glass port in the chamber. Finally, the rabbit was subjected to X-ray radiography to establish that no movement of the stacks had occurred, and to helium mass spectrographic testing for leak detection.

RABBIT ASSEMBLY
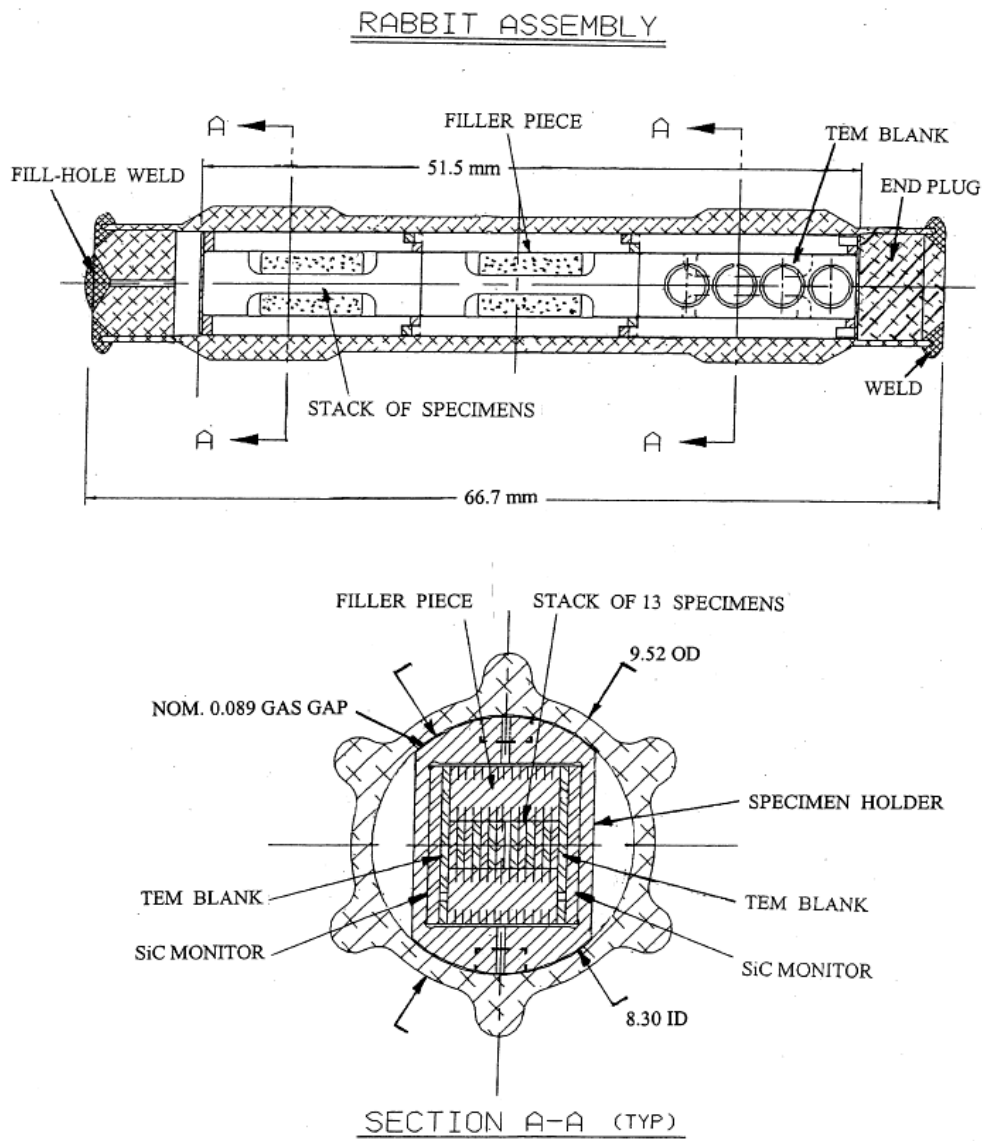
Fig. A3.1. Arrangement of specimens for the 290°C irradiations.

A3.2 Radiation Exposures

The turnaround time for the rabbit train in the Hydraulic Tube can be very short, less than a minute, if so desired. The neutron fluxes in the flux trap are well characterized [12] and are reproduced from one fuel cycle to another. Consequently, a desired neutron exposure can be obtained simply by controlling the time the rabbit spends in the flux trap. The specimens for the Phase 1 and 2 experiments were housed in ten rabbits that were irradiated in positions HT-3 and HT-7 of the Hydraulic Tube for times between 2.4 min. and about 350 h to five goal exposures spaced at decade increments. These exposures are listed in Table A3. The corresponding, nominal atomic displacements in the table range from 0.0001 dpa to 0.89 dpa. Rabbits F4 and F9 at the highest exposures were intended to reach 1 dpa but were curtailed due to unprecedented

73

demand for use of the Hydraulic Tube facility in view of an impending, maintenance outage of the HFIR. Dpa values were calculated on the basis of a displacement cross section for iron and stainless steel of 1.9×10^{-26} dpa per unit total neutron fluence derived for the neutron spectrum in the HFIR flux trap [13]. The corresponding cross section for zirconium is 1.7×10^{-26}, which makes the dpa values for Zircaloy-4 about 10% smaller than the listed nominal values.

Table A3. Irradiation exposure conditions. Neutron fluences are in units of $n.m^{-2}$.

Rabbit No.	HFIR No.	Irrad. Site	Exposure Period	Temp., ^{o}C	Total Fluence	Thermal Fluence	Fluence > 1 MeV	Nominal dpa
Phases 1 and 2; A533B steel and Zircaloy-4.								
F1	8-00-5	HT-3	2.4 min	65-100	5.0E21	3.2E21	5.9E20	0.0001
F2	8-00-3	HT-3	24 min	65-100	5.0E22	3.2E22	5.9E21	0.001
F3	8-00-1	HT-3	4.12 h	65-100	5.2E23	3.3E23	6.1E22	0.01
F5	7-00-3	HT-3	41.13 h	65-100	5.2E24	3.3E24	6.1E23	0.1
F4	8-00-13	HT-3	369.6 h	65-100	4.7E25	2.9E25	5.5E24	0.89
Phases 1 and 2; 316 stainless steel.								
F6	8-00-6	HT-7	2.4 min	65-100	4.9E21	3.0E21	5.8E20	0.0001
F7	8-00-4	HT-7	24 min	65-100	4.9E22	3.0E22	5.8E21	0.001
F8	8-00-12	HT-7	4.12 h	65-100	5.0E23	3.1E23	5.9E22	0.01
F10	7-00-7	HT-7	41.13 h	65-100	5.0E24	3.1E24	5.9E23	0.1
KF5[a]	4-98-2	HT-3	72 h	65-100	9.1E24	5.7E24	1.1E24	0.17
F9	8-00-10	HT-7	333.5 h	65-100	4.1E25	2.5E25	4.8E24	0.78
Phase 3; All alloys.								
F31	3-02-4	HT-7	4.2 h	288[b]	5.1E23	3.2E23	6.0E22	0.01
F29	3-02-5	HT-7	41.7h	288[b]	5.1E24	3.2E24	6.0E23	0.1
F28	3-02-3	HT-3	342h	288[b]	4.3E25	2.7E25	5.0E24	0.80

[a] From an earlier experiment in HT-3 position.

[b] Goal temperature; see Section 5.0 for discussion of actual temperature.

A4. Tensile Data Tables
The tensile test results for Phases 1 and 2 are listed in Table A4(1). The data for Phase 3 are in Table A4(2).

Table A4.1. Engineering tensile data at room temperature after irradiation at temperatures in range 60-100°C.

I.D	Mater.	dpa	YS (0.2% offset), MPa	UTS, Mpa	UE, %	TE, %
a77	A533B	0	459	595	12.5	17.8
a78		0	501	640	12.9	19.6
a85		0	512	652	11.5	20.6
a76		0	514	656	13	19.5
a34		0.0001	517	659	12.1	17.5
a35		0.0001	541	698	10.2	15.3
a22		0.001	506	636	12.3	18
a15		0.001	523	666	10.7	16.8
a14		0.001	528	684	10.9	16.4
a32		0.01	661	668	8.4	12.5
a33		0.01	678	692	7.8	13.1
a47		0.1	931	931	0	0.2
a48		0.1	935	935	0	0.3
a49		0.1	942	942	0	1.3
a40		0.89	1003	1003	0	1
a39		0.89	1043	1043	0	1.2
r74	Zr-4	0	378	434	12.3	29
r75		0	388	447	12	33.2
r83		0	415	471	12.3	28.2
r76		0	404	473	15	36.4
r13		0.00009	396	460	12.7	30.2
r12		0.00009	411	481	14.4	29.8
r14		0.0009	438	477	8.4	26.7
r18		0.0009	438	478	9.8	24.3
r30		0.009	521	514	3.2	16.3
r24		0.009	520	519	2.7	17
r50		0.09	560	584	0	11.7
r35		0.8	594	594	0	8.8
r34		0.8	601	601	0	9.8
t91	316SS	0	217	562	55.2	62.8
t80		0	237	572	54.2	56.3
t78		0	240	588	54.3	58.3
t76		0	243	593	58.7	61.6
t05		0.0001	256	609	57	59.6
t06		0.0001	288	695	63.1	67
t15		0.001	316	631	51.8	55
t17		0.001	354	677	52.7	59
t55		0.01	448	667	37.3	39.5
t21		0.01	449	682	38.1	40
t56		0.01	501	706	44.3	47.6
t22		0.01	470	714	38	42.8
t75		0.1	567	735	37	41.3
t81		0.1	574	740	35.1	39.1
t37		0.78	676	779	28.8	30
t32		0.78	672	788	32.6	36.1

Table A4.2. Engineering tensile data at 288°C and various strain rates after irradiation at elevated temperature.

ID	Mater.	dpa	Test Temp, °C (±2 °C)	Strain Rate, s^{-1}	YS (0.2% offset), MPa	UTS, MPa	UE, %	TE, %
A50	A533B	0	288	10^{-3}	470	670	10.2	14.3
A55		0	288	10^{-3}	419	617	9.5	13.4
A47		0.01	288	10^{-3}	440	611	9.7	12.9
A46		0.01	288	10^{-3}	455	634	9.1	12.3
A18		0.1	288	10^{-3}	460	629	9.1	12
A21		0.1	288	10^{-3}	448	614	6.9	9.8
A23		0.1	RT	10^{-3}	528	670	10.6	14.9
Ave*		0	RT	10^{-3}	496	636	12.5	19.4
A51		0	288	10^{-1}	487	639	8.4	12.6
A60		0	288	10^{-1}	423	564	8.4	13
A48		0.01	288	10^{-1}	467	598	9.4	12.7
A43		0.01	288	10^{-1}	471	598	9.1	12.6
A16		0.1	288	10^{-1}	439	553	6.7	9.5
A14		0.1	288	10^{-1}	475	593	7.2	10.1
A40		0.01	288	10^{0}	461	594	7.3	11.8
A25		0.1	288	10^{0}	466	558	5.5	8
R51	Zr-4	0	288	10^{-3}	142	192	18.8	51.1
R53		0	288	10^{-3}	145	195	18.5	43.1
R46		0.01	288	10^{-3}	154	210	10.4	34.8
R47		0.01	288	10^{-3}	153	200	13.1	35.1
R20		0.1	288	10^{-3}	177	226	10.2	37
R14		0.1	288	10^{-3}	155	204	13.9	37
R23		0.1	RT	10^{-3}	400	475	11.66	26.8
Ave*		0	RT	10^{-3}	396	456	12.9	31.7
R50		0	288	10^{-1}	249	282	12.4	45.4
R52		0	288	10^{-1}	225	252	11.4	38.8
R40		0.01	288	10^{-1}	225	261	13.8	52.8
R44		0.01	288	10^{-1}	236	269	12.3	41.7
R16		0.1	288	10^{-1}	223	280	14	42.2
R15		0.1	288	10^{-1}	237	273	9.3	36.6
R43		0.01	288	10^{0}	299	330	3	29
R21		0.1	288	10^{0}	349	349	0	29
T57	316SS	0	288	10^{-3}	143	503	34	35.1
T53		0	288	10^{-3}	133	469	30.8	31.8
T47		0.01	288	10^{-3}	150	488	33.5	34.4
T49		0.01	288	10^{-3}	156	491	31.7	33.2
T18		0.1	288	10^{-3}	146	490	34.4	35.6
T14		0.1	288	10^{-3}	150	494	33.8	35.3
T23		0.1	RT	10^{-3}	229	619	54.7	58.3
Ave*		0	RT	10^{-3}	234	579	55.6	59.7
T54		0	288	10^{-1}	156	474	32.5	34
T55		0	288	10^{-1}	171	511	31.6	31.9
T50		0.01	288	10^{-1}	193	544	32.4	34
T44		0.01	288	10^{-1}	181	537	32	33.4
T13		0.1	288	10^{-1}	209	538	27	27.4
T16		0.1	288	10^{-1}	234	517	29	30.9
T40		0.01	288	10^{0}	247	506	27	30.5
T24		0.1	288	10^{0}	243	514	29.4	31.2

* Average room temperature (RT) properties of unirradiated specimens from Table A4-1.

A5. TEM Preparations and Observation Conditions

The tensile specimen was not the only area of miniaturization in this project. The use of miniature tensile specimens meant that TEM pieces taken from the specimen gauge sections would be significantly smaller and of different shape than the standard 3 mm diameter TEM disk. Indeed, the TEM pieces from the gauge sections had dimensions of 1.5 x 1.5 x 0.25 mm. Preparation of electrothinned foils from these pieces in a Tenupol electropolishing apparatus required substantial development work and modification of Tenupol specimen holders, as described in Ref. 10. For the electrothinning, a single polishing solution consisting of 600 ml methanol, 360 ml butylcellosolve, 60 ml perchloric acid, and 5 ml glycerin, was used for all three materials. The operating conditions were

	316SS	A533B and Zr-4
Voltage (V)	10-12	10-12
Current (mA)	35-40	30
Temperature (^{o}C)	-12	-12
Flow rate	Setting #3	Setting #3
Sensitivity	Setting #7	Setting #7

For the TEM examinations a strict routine was followed to ensure that different specimens were studied under optimum viewing and diffracting conditions to observe planar deformation. It is well established that plastic deformation by slip bands, channeling, and mechanical twinning occur primarily on certain favored slip systems, notably on the planes with the highest atomic densities, and the direction of the deformation is usually in the direction of closest atomic packing. In order for such planar deformation to be seen most clearly the plane must be examined edge-on, otherwise it is masked by material above and below it and its planar nature is difficult to verify. Therefore, the foils were tilted with respect to the beam direction so as to lay the slip planes for the expected deformation on, or close to, the beam direction, thereby allowing the channels to be viewed edge-on. This permits channel widths and spatial distributions to be measured most easily. The following viewing conditions were used for each alloy:

a. 316 stainless steel has a face-centered cubic crystal structure and the major slip system is {111}<110>. For this material, the beam direction, B, was set at [011], and the diffracting vector, g, was chosen to be 200 or $11\bar{1}$.

b. A533B steel is tempered bainite with a ferritic body-centered cubic crystal structure. It has numerous slip systems, the most common of which is {110}<111>. B was set at [001], and g=200 or 110.

c. Zircaloy-4 has a close-packed hexagonal crystal structure. Its slip systems can be on {0001} basal planes, {10$\bar{1}$0} prism planes, or on {10$\bar{1}$1} pyramidal planes, all with a <11$\bar{2}$0> slip direction. B was set at [0001], and g=[$\bar{1}$100] or [10$\bar{1}$0]. Under these conditions, very thin planar faults will exhibit streaks in the diffraction patterns, which is useful for identifying stacking faults and fine deformation twins.

Appendix B: Bibliography of localized plastic flow in irradiated iron and ferritic steels

B1.   J. C. Wilson, paper # P/1978 in *Second United Nations International Conference on Peaceful Uses of Atomic Energy*, Vol. 5 (1958) 431-445.

B2.   R. G. Berggren, in Proc. of *USAEC Conf. On Status of Radiation Effects Research on Structural Materials and the Implications to Reactor Design*, Chicago, Ill, Oct. 15-16, 1959, USAEC (1959) 91-127.

B3.   B. L. Eyre, Phil. Mag. 7 (1962) 1609-1613.

B4.   B. L. Eyre, Phil. Mag. 7 (1962) 2107-2113.

B5.   B. L. Eyre and A. F. Bartlett, Phil. Mag. 12 (1965) 261-272.

B6.   J. S. Bryner, Acta Met. 14 (1966) 323-336.

B7.   S. M. Ohr, Scripta Met. 2 (1968) 213-216.

B8.   F. A. Smidt, Jr., "Dislocation-Substructure Interactions in Irradiated Iron and Steel", BNWL-1045, Battelle Pacific Northwest Laboratory, June 1969.

B9.   F. A. Smidt and B. Mastel, Phil. Mag. 20 (1969) 651-656.

B10.   F. A. Smidt, Scripta Met. 4 (1970) 517-520.

B11.   J. S. Bryner and J. G. Y. Chow, Acta Met. 18 (1970) 191-200.

B12.   H. Mughrabi, D. Strohle, and M. Wilkens, Zeit. fur Metallkunde 72-5 (1981) 300-309.

B13.   B. N. Singh, A. J. E. Foreman, and H. Trinkaus, J. Nucl. Mater. 249 (1997) 103-115.

B14.   B. N. Singh, A. Horsewell, and P. Toft, J. Nucl. Mater. 271 & 272 (1999) 97-101.

B15.   Y. Chen, P. Spätig, and M. Victoria, J. Nucl. Mater. 271&272 (1999) 128-132.

B16.   M. Victoria, N. Baluc, C. Bailat, Y. Dai, M. I. Luppo, R. Schäublin, and B. N. Singh, J. Nucl. Mater. 276 (2000) 114-122.

B17.   M. I. Luppo, C. Bailat, R. Schäublin, and M. Victoria, J. Nucl. Mater. 283-287 (2000) 483-487.

B18.   D. S. Gelles and R. E. Schäublin, Mater. Sci. and Eng. A309-310 (2001) 82-86.

B19. D. S. Gelles, M. L. Hamilton, and R. E. Schäublin, in *Effects of Radiation on Materials: 20th International Symosium*, ASTM STP 1405, Amer. Soc. for Testing and Mater. (2001) 523-534.

B20. N. Hashimoto, S. J. Zinkle, R. L. Kleuh, A. F. Rowcliffe, and K. Shiba, Mat. Res. Soc. Symp. Proc. 650 (2001) R1.10.1-R1-10-6.

Appendix C: Bibliography of localized plastic flow in irradiated austenitic stainless steels

C1.   F. R. Shober and W. E. Murr, *Symposium on Radiation Effects on Metals and Neutron Dosimetry*, ASTM STP 341, Amer. Soc. for Testing and Mater. (1962) 325-343.

C2.   J. O. Stiegler and J. R. Weir, Jr., Chapter 11 in "Ductility", pub. Amer. Soc. for Metals, (1967) 311-342.

C3.   R. L. Fish, J. L. Straalsund, C. W. Hunter, and J. J. Holmes, in *Effects of Radiation on Substructure and Mechanical Properties of Metals and Alloys*, ASTM STP 529, Amer. Soc. for Testing and Mater. (1973) 149-164.

C4.   E. E. Bloom, in *Radiation Damage in Metals*, American Society for Metals, Metals Park, Ohio, (1975) 295-329.

C5.   H. Saka, K. Noda, K. Matsumoto, and T. Imura, Phys. Stat. Sol. 31 (1975) 139-149.

C6.   G. R. Odette and G. E. Lucas, J. Nucl. Mater. 179-181 (1991) 572-576.

C7.   M. Suzuki, F. Fujimura, A. Sato, J. Nagakawa, N. Yamamoto, and H. Shiraishi, Ultramicroscopy 39 (1991) 92-99.

C8.   Fujio Abe, Minoru Narui, and Hideo Kayano, Mater. Trans., Japan Inst. Metals 33 (1992) 1123-1129.

C9.   Masayoshi Suzuki, A. Sato, T. Mori, J. Nagakawa, N. Yamamoto, and H. Shiraishi, Phil. Mag. A 65 (1992) 1309-1326.

C10.   S. M. Bruemmer, J. I. Cole, J. L. Brimhall, R. D. Carter, and G. Was, in *Sixth Internat. Symp. on Environmental Degradation of Materials in Nuclear Power Systems-Water Reactors*, The Metals and Minerals Society (1993) 537-546.

C11.   M. G. Horsten and M. I. de Vries, J. Nucl. Mater. 212-215 (1994) 514-518.

C12.   James I. Cole and Stephen M. Bruemmer, J. Nucl. Mater. 225 (1995) 53-58.

C13.   Marc G. Horsten and Martin I. de Vries, in *Effects of Radiation on Materials: 17th International Symposium*, ASTM STP 1270, Amer. Soc. for Testing and Mater. (1995) 919-932.

C14.   J. L. Brimhall, J. I. Cole, J. S. Vetrano, and S. M. Bruemmer, Mat. Res. Soc. Symp. Proc. 373, Materials Research Society (1995) 177-182.

C15.   J. E. Pawel, A.F. Rowcliffe, D.J. Alexander, M.L. Grossbeck, and K. Shiba, J. Nucl. Mater. 233-237 (1996) 202-206.

C16.   L. Boulanger, F. Soisson, and Y. Serruys, J. Nucl. Mater. 233-237 (1996) 1004-1008.

C17.   J. E. Pawel, A. F. Rowcliffe, G. E. Lucas, and S. J. Zinkle, J. Nucl. Mater. 239 (1996) 126-131.

C18.   S. G. Song, J. I. Cole, and S. M. Bruemmer, Acta Mater. 45 (1997) 501-511.

C19.   Peter Mullner, Mater. Sci. Eng. A234-236 (1997) 94-97.

C20.   G. E. Lucas, Mat. Res. Soc. Symp. Proc. 439, Materials Research Society (1997) 425-436.

C21.   Shiro Jitsukawa, Ikuo Ioka, and Akimichi Hishinuma, J. Nucl. Mater. 271 & 272 (1999) 167-172.

C22.   S. M. Bruemmer, J. I. Cole, R. D. Carter, and G. S. Was, Mat. Res. Soc. Symp. Proc. 439 (1997) 437-444.

C23.   J. Chen, Y. Dai, F. Carsughi, W. F. Sommer, G. S. Bauer, H. Ullmaier, J. Nucl. Mater. 275 (1999) 115-118.

C24.   C. Bailat, F. Groschel, and M. Victoria, J. Nucl. Mater. 276 (2000) 283-288.

C25.   E. H. Lee, T. S. Byun, J. D. Hunn, N. Hashimoto, and K. Farrell, J. Nucl. Mater. 281 (2000) 65-70.

C26.   M. Victoria, N. Baluc, C. Bailat, Y. Dai, M. I. Luppo, R. Schäublin, and B. N. Singh, J. Nucl. Mater. 276 (2000) 114-122.

C27.   T. S. Byun and K. Farrell, in *Proc. Fourth International Topical Meeting on Nuclear Applications of Accelerator Technology,* Washington D.C., November 12-16, 2000, Amer. Nucl. Soc. (2000) 270-277.

C28.   C. Baillat, A. Almazouzi, N. Baluc, R. Schaublin, F. Groschel, and M. Victoria, J. Nucl. Mater. 283-287 (2000) 446-450.

C29.   K. Farrell and T. S. Byun, "Tensile Properties of Candidate SNS Materials after Irradiation in Two Neutron Areas in the LANSCE Accelerator", SNS report, SNS/TR-211, Oak Ridge National Laboratory, Jan. 2001.

C30.   N. Hashimoto, S. J. Zinkle, A. F. Rowcliffe, J. P. Robertson, and S. Jitsukawa, J. Nucl. Mater. 283 (2001) 528-534.

C31.   T. S. Byun, E. H. Lee, J. D. Hunn, K. Farrell, and L. K. Mansur, 294 (2001) 256-266.

C32.   K. Farrell and T. S. Byun, J. Nucl. Mater. 296 (2001) 129-138.

C33.   Y. Dai, X. Jia, J. C. Chen, W. F. Sommer, M. Victoria, and G. S. Bauer, J. Nucl. Mater. 296 (2001) 174-182.

C34.   E. H. Lee, T. S. Byun, J. D. Hunn, K. Farrell, and L. K. Mansur, J. Nucl. Mater. 296 (2001) 183-191.

C35.   E. H. Lee, T. S. Byun, J. D. Hunn, M. H. Yoo, K. Farrell, and L. K. Mansur, Acta Mater. 49 (2001) 3269-3276.

C36.   E. H. Lee, T. S. Byun, J. D. Hunn, M. H. Yoo, K. Farrell, and L. K. Mansur, Acta Mater. 49 (2001) 3277-3287.

C37.   K. Farrell, T. S. Byun, J. W. Jones, L. T. Gibson, R. G. Sitterson, N. Hashimoto, J. L. Bailey, and J. Gardner, "Small Specimen Procedures for Determination of Deformation Maps", in *Small Specimen Test Techniques: Fourth Volume,* ASTM STP 1418, Amer. Soc. for Testing and Materials (2002) 283-293.

C38.   T. S. Byun, K. Farrell, E. H. Lee, J. D. Hunn, and L. K. Mansur, J. Nucl. Mater., 298 (2001) 269-279.

Appendix D: Bibliography of localized plastic flow in irradiated Zr alloys

D1.   M. J. Makin and F. J. Minter, J. Inst. Metals 85 (1956-57) 397-402.

D2.   A. L. Bement, J. C. Tobin, and R. G. Hoagland, in *Flow and Fracture of Metals and Alloys in Nuclear Environments,* ASTM STP 380, Am. Soc. Testing Mater. (1964) 364-385.

D3.   J. W. Weber, in *Effects of Radiation on Structural Materials,* ASTM STP 426, Am. Soc. Testing Mater. (1967) 653-669.

D4.   C. E. Ells and C. D. Williams, Suppl. to Trans. Japan Inst. Metals 9 (1968) 214-219.

D5.   C. D. Williams and R. W. Gilbert, "Fast Neutron Damage in Zirconium-Based Alloys", AECL-3308, Atomic Energy of Canada Report (June 1969); and pp 235-247 in *Radiation Damage in Reactor Materials, Vol I*, IAEA-SM-120/C-3, Vienna, 2-6 June 1969, International Atomic Energy Agency.

D6.   C. E. Coleman, D. Mills, and J. van der Kuur, Canadian Metallurgical Quarterly 11-1(1972) 91-100.

D7.   B. A. Cheadle, C. E. Ells, and J. van der Kuur, in *Zirconium in Nuclear Applications,* ASTM STP 551, Am. Soc. Testing Mater. (1974) 370-384.

D8.   H. S. Rosenbaum, G. F. Rieger, and D. Lee, Met. Trans. 5 (1974) 1867-1874.

D9.   G. F. Rieger and D. Lee, in *Zirconium in Nuclear Applications,* ASTM STP 551, Am. Soc. Testing Mater. (1974) 335-369.

D10.   G. J. C. Carpenter and J. F. Watters, in *Zirconium in Nuclear Applications,* ASTM STP 551, Am. Soc. Testing Mater. (1974) 400-415.

D11.   W. L. Bell, Discussion, ASTM STP 551, Am. Soc. Testing Mater. (1974) 199-200.

D12.   R. R. Hosbons, C. E. Coleman, and R. A. Holt, "Numerical Simulation of Tensile Behaviour of Nuclear Fuel Cladding Materials", AECL-5245, Atomic Energy of Canada Limited, October 1975.

D13.   J. J. Jonas, R, A. Holt, and C. E. Coleman, Acta Met. 24 (1976) 911-918.

D14.   D.O. Northwood, R. W. Gilbert, and C. E. Coleman, in *Zirconium in the Nuclear Industry,* ASTM STP 633, Am. Soc. Testing Mater. (1977) 418-436.

D15.   D. Lee and R. B. Adamson, in *Zirconium in the Nuclear Industry,* ASTM STP 633, Am. Soc. Testing Mater. (1977) 385-401.

D16.   T. Onchi, H. Kayano, and Y. Higashiguchi,, J. Nucl. Mater. 88 (1980) 226-235.

D17.   W. L. Bell and R. B. Adamson in *Advanced Techniques for Characterising Microstructure,* The Metallurgical Society of AIME, Warrendale, Pa. (1983) 115-124.

D18.   R. B. Adamson, S. B. Wisner, R. P. Tucker, and R. A. Rand, in *The Use of Small Scale Specimens for Testing Irradiated Material*, ASTM STP 888, Am. Soc. Testing Mater. (1986) 171-185.

D19.   R. B. Adamson, in *Zirconium in the Nuclear Industry: Twelfth International Symposium,* ASTM STP 1345, Am. Soc. Testing Mater. (2000) 15-31.

D20.   M. Fregonese, C. Regnard, L. Rouillon, T. Magnin, F. Lefebvre, and C. Lemaignan, in *Zirconium in the Nuclear Industry: Twelfth International Symposium,* ASTM STP 1345, Am. Soc. Testing Mater. (2000) 377-398.

MAPPING FLOW LOCALIZATION PROCESSES IN DEFORMATION OF IRRADIATED REACTOR STRUCTURAL ALLOYS-FINAL REPORT

Distribution

Internal Distribution:
1. E. E. Bloom, ORNL

2. T. S. Byun, ORNL/UT

3. K. Farrell, ORNL

4. N. Hashimoto, ORNL/UT

5. L. L. Horton, ORNL

6. C. R. Hudson II, ORNL

7. Y. Katoh, ORNL

8. R. L. Kleuh, ORNL

9. L. K. Mansur, ORNL

10. S. R. Martin, Jr., DOE/ORNL

11. G. E. Michaels, ORNL

12. R. K. Nanstad, ORNL

13. Yu N. Osetskiy, ORNL

14. L. L. Snead, ORNL

15. R. E. Stoller, ORNL

16. F. W. Wiffen, ORNL

17. S. J. Zinkle, ORNL

External Distribution:

18. Denise Berry, U.S. Department of Energy, Oakland, CA

19. Paul Cantonwine, Westinghouse Bettis Laboratory, West Mifflin, PA

20. Madeline A. Feltus, U.S. Department of Energy, Washington, DC

21. Lynn Hall, NE-20, U.S. Department of Energy, Germantown, MD

22. Lisa Herrera, U.S. Department of Energy, Germantown, MD

23. Stuart Maloy, Los Alamos National Laboratory

24. Marty Martinez, Energetics, Inc., Maryland

25. Tom Miller, U.S. Department of Energy, Germantown, MD

26. Rebecca Richardson, U.S. Department of Energy, Oakland, CA

27. Bachu Singh, Riso National Laboratory, Denmark

28. James F. Stubbins, University of Illinois at Urbana-Champaign, IL

29. Charles Thompson, U.S. Department of Energy, Germantown, MD

30. Gary Was, University of Michigan

31. Phil Wong, NSPD, U.S. Department of Energy, Oakland, CA

32. Edward P. Simonen, PNNL, MS P8-15, P.O. Box 999, Richland, WA 99352